Distribution Agreement

Signature:

Yixiao Dong Date

Functionally-Responsive Hydrogels: from Dynamic Coloration to Biosensing

By

Yixiao Dong

Doctor of Philosophy

Chemistry

[Advisor's signature] Khalid Salaita

Advisor

[Member's signature] Craig L. Hill

Committee Member

[Member's signature] Brian Dyer

Committee Member

Accepted:

Kimberly Jacob Arriola, Ph.D, MPH

Dean of the James T. Laney School of Graduate Studies

Date

Functionally-Responsive Hydrogels: from Dynamic Coloration to Biosensing

By

Yixiao Dong

M. S. Wuhan University of
Technology, 2015

Advisor: Khalid Salaita, Ph.D.

An abstract of

A dissertation submitted to the Faculty of the James T.
Laney School of Graduate Studies of Emory University

in partial fulfillment of the requirements for the degree of

Doctor of Philosophy

in the Department of Chemistry

2022

Abstract

Functionally-Responsive Hydrogels: from Dynamic Coloration to Biosensing

By Yixiao Dong

There are numerous examples of living creatures taking advantage of various responsive mechanisms to adapt to their environment. For example, chameleons change their skin color for mating or intimidating predators. *Mimosa pudica* folds its leaves inward upon mechanical perturbation as a defense mechanism, and the Venus flytrap closes its trapping leaves in response to the minute force of an insect landing on it. These examples have inspired numerous works developing responsive and "smart" materials. To date, scientists have built a library of responsive hydrogels according to their various response types, such as pH, heat, biomolecules, magnetic field, salt gradient, etc. In this dissertation, we have further expanded this library of responsive hydrogel materials to address specific challenges in the field, including strain-accommodation, on-demand assembly, and cellular force sensing.

In chapter one, a comprehensive overview is given regarding previously developed responsive hydrogels with different functionalities. The overview is focused on three major aspects, including the components, responsibilities, and latent applications. The diversity of the materials demonstrates the great potential of functionally-responsive hydrogels in addressing different challenges in materials science and engineering.

In chapter two, the design of strain-accommodating smart skin (SASS) is proposed based on the inspiration of a chameleon. Both finite element analysis and experimental results confirm the strain accommodating behavior of SASS material which is different from previously developed responsive photonic hydrogels with accordion-type structure. In the end, the SASS design demonstrates latent applications such as camouflage and anti-counterfeiting.

In chapter three, a more challenging topic about on-demand assembly is proposed. In this case, the chromatic response of photonic hydrogel is no longer rely on the swelling/deswelling of hydrogel matrix, but rather the *in situ* assembly of magnetic nanoparticles. The on-demand assembly mechanism can not only avoid the volumetric change of common responsive hydrogels, but also sheds light on novel rewritable technology, information storage, and encryption technology.

In chapter four, a responsive hydrogel was developed to measure cellular forces at the pico-newton level. We chemically modify single molecular tension probes on a PEG hydrogel surface. This responsive hydrogel provides a physiologically identical environment while measuring the cellular tension surface. Attempts of cellular tension imaging beyond 2D surface has also been introduced.

The final chapter provides comprehensive summary and outlook about functionally-responsive hydrogels, beyond the scope of what is described in this dissertation. The prospective discussions include alternative material design, characterization, and other potential applications.

ACKNOWLEDGMENT

I want to express my sincere gratitude to my PhD advisor Dr. Khalid Salaita who contributed, both intellectually and financially, throughout all my research works as I was conducting for this dissertation. His patience and dedication have led me towards achieving remarkable milestones in my PhD career. I fondly remember the time when he took time out of his busy schedule to discuss research projects with me and help me troubleshoot challenging issues in my experiments throughout my 6 years of doctoral studies. He strikes a perfect balance between ensuring we dedicate and develop ourselves into critical thinkers and researchers, but also ensure we have the time and space to seek a creative side so we can discover our professional identity. I also want to express my gratitude towards my research committee members: Dr. Craig L. Hill and Dr. Brain Dyer, for their invaluable advice, encouragement, and even criticism on my research projects during these years. I would not have become the critical thinker and researcher I am today without the help of my advisor and committee members.

I also want to thank all my fantastic friends and collaborators during these years. Especially thank SK Aysha Rashid, who collaborated with me for the hydrogel-based cellular tension sensing matrix project. She is also an amazing friend that helped me with many outreach events and activities in the past. I really enjoyed the time we spent together as friends, and really enjoyed all the hot pots we consumed over the years. I also want to thank my dear friend and amazing colleague Radhika Sharma. I enjoyed serving as an essential collaborator for her thesis project with lipid nanodiscs. She has also been my biggest cheerleader and support throughout my ups and downs in grad school, and she dedicated her time to ensure I land big in terms of my career and helped me with procuring my next job along with continuous assistance for other career opportunities during my search. Additionally, I want to thank my lab members such as Dr. Alisina

Bazrafshan, J. Dale Comb, Dr. Hiroaki Ogasawara, Dr. Allison Ramey-Ward, Dr. Rong Ma, Dr. Hanquan Su, Dr. Jing Zhao, Dr. Kimberly Clarke, Dr. Victor Ma, Selma Piranej, Tharindu Rajasooriya, etc. for being amazing colleagues. While I received generous support from my in-lab colleagues, my friends and collaborators outside my lab cemented my group of support and I appreciate the efforts of Dr. Eric R. Weeks, Dr. Cong Cao, Dr. Misael Adair Romero, and Dr. Wei Sun. I also especially thank Dr. David Lynn for helping me with my PhD application process of Emory University. My thanks extend to the faculty, staff and the students of the Chemistry department at Emory who have all contributed to the amazing atmosphere for pursuing graduate studies.

At last, I would like to give my big thanks to my lifetime partner Eduardo Sanchez who accompanied and supported me every step of the way in these past 4 years. He bolstered me when I was down and celebrated every one of my accomplishments. I look forward to taking the next steps with him as my husband. I am also grateful to the long-distance support provided by my parents and all my relatives in China. As the proverbial adage states: “it takes a village to raise a child” and without their support, I would not be in the place that I am today.

TABLE OF CONTENTS

LIST OF FIGURES

LIST OF ABBREVIATIONS

DLS	Dynamic light scattering
RICM	Reflection interference contrast microscopy
SASS	Strain-accommodating smart skin
PEG	Polyethylene glycol
MNPs	Magnetic nanoparticles
NIPAM	N-isopropylacrylamide
LCST	Lower critical solution temperature
UCST	Upper critical solution temperature
OMA	Optomechanical actuator
MTFM	Molecular Tension Fluorescence Microscopy
LatB	Latrunculin B
SEM	Scanning electron microscopy
TEM	Transmission electron microscopy
RGD	Arginine-Glycine-Aspartic Acid
PC	Photonic crystal

CHAPTER 1. INTRODUCTION

1.1 An overview of responsive hydrogels

Hydrogel materials are highly swelled molecular networks where nearly 90% of its weight is water. Responsive hydrogels are the most diverse and intensely studied functional materials due to their potential to be programmed with various responding behaviors and have broad applications in areas such as actuators[1], electronics[2], sensors, drug delivery systems, and others. To create a dynamically responsive hydrogel material, one needs to be able to program an input–output function either from molecular (bottom-up) or geometry (top-down) programmability. Bottom-up molecular programmability is often used for patterning hydrogel materials comprised of DNA[3], peptides[4], synthetic copolymers[5], and polysaccharides[6]. Controlling the molecular sequence of these macromolecules building blocks allows for generating diverse responsivities of functional hydrogel materials.[3-6] In contrast to bottom-up self-assembly, “top-down” approaches tend to be more labor-intensive creating structures in a more serial process, but provide highly tailored geometries and configurations for responsive hydrogels.[7] These top-down approaches confer responsivity beyond the molecular structure and properties of the material, leading to an architecturally-directed responsivity. Although the “top-down” and “bottom-up” approaches are distinct and separate concepts in responsive hydrogel programming, they are not exclusive to each other. In fact, it is quite common for functionally responsive hydrogel materials to include both methods to better achieve the desired response, composition, and form.[8, 9]

1.2 Material types

Synthetic hydrogels, and synthetic polymers in general, are often selected for their ease of availability, as well as their ability to be chemically modified for unique applications[10]. This is especially true of functionally responsive hydrogels, where the ability to manipulate chemical and mechanical properties allows for diverse applications and tuned responsiveness. Synthetic polymers can be intrinsically responsive to external stimuli, such as the responsivity of N-isopropylacrylamide (NIPAm) and N-isopropylmethacrylamide (NIPMAm) to heating[11-13], or the sensitivity of polyethylene glycol (PEG) hydrogels to humidity[14].

Responsive hydrogels can also be made entirely or partially of naturally derived materials. While these types of polymers can be subject to sourcing concerns, naturally derived materials offer distinct advantages. Polymers such as alginate, chitosan, and hyaluronic acid are highly sensitive to the ionic strength and the electrochemical environment of their medium[15-17]. Thus, naturally derived materials will generally actuate based on cation content and pH[18, 19]. Nucleic acids, long studied for their role in information carrying functions in biology and genetics, can be synthesized and controlled precisely have recently emerged as a biopolymer building block for the construction of responsive hydrogels[20, 21]. These gels are sensitive to their thermal and chemical environment, which can alter force production by disrupting hybridization[22].

While some hydrogels are responsive in their pure form, mechanical activity is often induced in gels with the addition of dopants, such as metal nanoparticles or chemical impurities.[1] Additionally, multiple synthetic and/or naturally derived polymers can be combined to form composites that leverage the advantages of both materials, enhancing factors such as programmability, responsivity, and material properties[23, 24].

1.3 Responsivity

A hallmark of responsive hydrogel is their ability to respond to a variety of external stimuli (**Figure 1.1**). These responses are intrinsically tied to the design of the material, and each has unique advantages and disadvantages, dependent on the intended use of the hydrogel. Notably, even though responsive hydrogels can respond to a variety of external stimuli, the primary responsive form pertains to be the swelling and deswelling of the hydrogel networks in most of the cases.

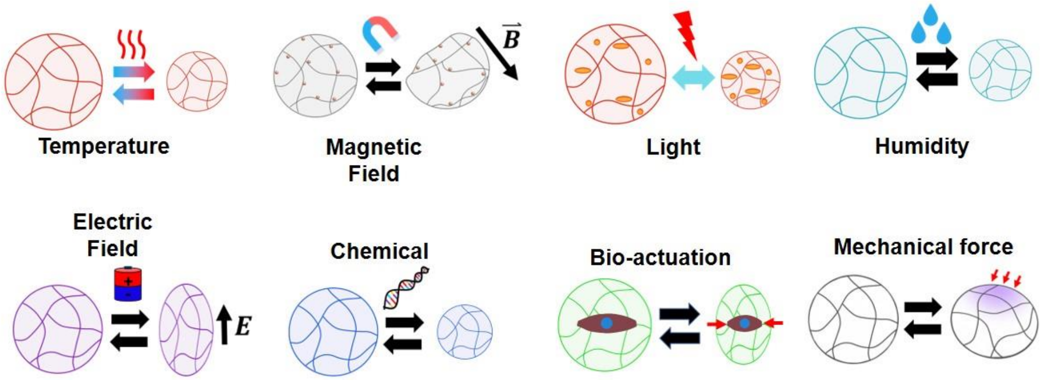

Figure 1.1. Schematics of typical responsivities for hydrogel materials. Responsive hydrogels can be triggered by a variety of stimuli, dependent on the material design. Different hydrogels can respond to heating, magnetic or electric fields, light, hydration state, oxidation state, specific molecules in solution, pH, ionic strength, and even extrinsic mechanical forces.

1.3.1 Thermoresponsive Materials

Among the most studied responsive hydrogels are the thermoresponsive polymers, which undergo conformational changes at the molecular level when heated to specific temperatures. This temperature is defined as either a lower critical solution temperature (LCST) or upper critical solution temperature (UCST), as described below.

Responsive hydrogel with a lower critical solution temperature (LCST) are hydrogels that become less soluble upon increasing the environmental temperature[25]. This reduced solubility of polymer chains causes the overall hydrogel to shrink or collapse upon heating. Poly(N-isopropylacrylamide) (pNIPAM) and its derivatives have been studied intensively many decades because of their facile synthesis and well-characterized LCST that is conveniently above room temperature (~32 ^{o}C). By making pNIPAM hydrogels using different monomers or co-polymers and employing a variety of crosslinking approaches, the transition temperature of pNIPAM hydrogels can be tuned which leads to the ability to tune the shape as an output.

Hydrogel backbones that have an upper critical solution temperature (UCST) are mostly created through binary polymer networks, in which polymer-polymer hydrogen bond interactions are stronger than polymer-water bonds interactions at room temperature[1, 26, 27]. Generally, this kind of polymer-polymer interaction network can be built through two methods: copolymerization, or interpenetration of different polymer networks.

The UCST window and UCST temperature are mainly controlled or finetuned by three different aspects: components of polymer-polymer pairs, ratio between the different polymers, ionic strength and pH of aqueous medium. At least three types of polymer-polymer pairs have been reported recently for the fabrication of responsive hydrogels. Hua et al.[28] reported UCST responsive hydrogel based on interpenetrating networks of poly(acrylic acid) (pAAc) and poly(acrylamide) (pAAm). Homogeneous pAAm gel networks were first synthesized by radical polymerization. Then, to create programmability in the design, an anisotropic responsive hydrogel was fabricated by photopolymerizing the pAAc network on one side of pAAm network. Upon cooling to room temperature, the UCST responsive hydrogel bend to the side that is rich in pAAc. The temperature responsivity has a wide window of 30-60 ^{o}C, and programmable actuation was realized through partial heating/cooling of specifically designed hydrogel shapes. Similarly, Auge et al.[26] studied the UCST volume transition of poly(acrylamide-co-acrylonitrile) copolymer hydrogel, and Ding et al.[27] studied the UCST transition of methyl cellulose-graft-polyacrylamide (MC-g-PAM) hydrogels.

1.3.2 Light Responsive Materials

One of the most common methods of triggering the response of hydrogel materials is via illumination with specific wavelengths of light. The light-driven mechanism offers several advantages: remote actuation, tunable responsiveness, and the potential to use natural sunlight in some applications. The majority of these responsive materials are hydrogel nanocomposites, with the inclusion of nanoparticles or specific chemical compounds reacting with the light and driving the response (**Figure 1.2**). In this section, we will detail the current mechanisms used to attain actuation in this manner.

One mechanism for light-driven hydrogel actuation is responsivity to far red, near-infrared (NIR) and infrared (IR) light. To accomplish this, nanomaterials, such as gold nanostructures, are incorporated into a hydrogel matrix made of thermoresponsive polymers: for example, N-isopropylacrylamide (NIPAM)[29]. Noble metal nanostructures found in these composite hydrogel exhibit distinct absorption spectra at visible and IR zone of wavelengths that is highly dependent on particle morphology: larger aspect ratios (length/width) show a demonstrated red-shift in absorbed IR wavelengths[30]. This causes a surface plasmonic resonance in the nanoparticle, leading to photothermal heating that drives the local volume phase transition of the thermoresponsive polymer matrix[31, 32] (**Figure 1.2a**). One example of this technology is the optomechanical actuator (OMA) developed by our group[32] where a poly-N-isopropyl methacrylamide (NIPMAm) nanoparticle is polymerized around a gold nanorod core to absorb NIR light. The diameter of these

OMAs collapses from ~500 nm to ~250 nm upon illumination and can be used to apply forces to external systems, such as living cells and biomolecules (**Figure 1.2b**)[32, 33].

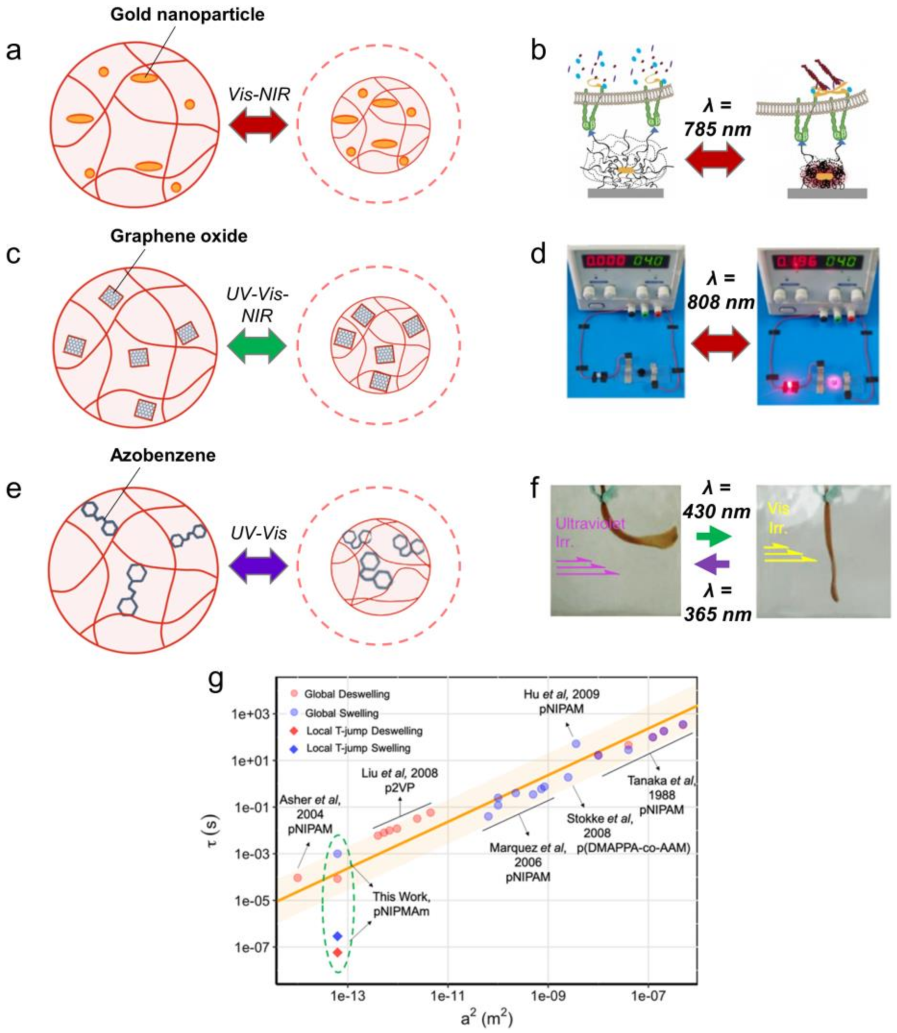

Figure 1.2. Mechanisms of photo responsive hydrogels. Light-responsive hydrogels can be designed to be mechanically active under illumination from various wavelengths. a) Hydrogel made of thermoresponsive polymers with the inclusion of gold nanoparticles is common for inducing IR and visible light responsivity. b) An example of this is the NIPMAm-coated gold nanorod structure designed by Liu et al, which was demonstrated to apply forces to cells. Reprinted with permission.[32] Copyright 2015, Springer Nature. c) Graphene oxide nanostructures can induce photoresponsivity at a variety of light wavelengths, d) such as one example in which graphene oxide-containing responsive hydrogel were used as an electrical switch controlled by NIR light. Reprinted with permission[36]. Copyright 2015, American Chemical Society. e) Responsivity to UV light wavelengths can be programmed by leveraging the photoisomerization of molecules such as azobenzene. f) This can create mechanical actuation in the presence of specific wavelengths, but not others, as demonstrated by Takashima and colleagues. Reprinted with permission[43]. Copyright 2012, Springer Nature. g) Comparison of nanoparticle radius (a^2) to actuation time constant (τ) among published thermally and photothermally responsive materials. Reprinted with permission[45]. Copyright 2018 American Chemical Society.

However, metallic nanoparticles are not the only way to achieve IR responsivity in hydrogel. Graphene nanostructures have also been employed, and these provide light-to-heat conversion similar to metals. Graphene, and graphene oxides, undergo photothermal heating under numerous wavelengths, including strong absorption peaks in the IR, due to a strong photoelectric effect[34, 35] (**Figure 1.2c**). Another interesting property that arises from this effect in graphene-containing hydrogel composite is electrical conductivity (this can also induce mechanical responsivity, as described later in this section). This was leveraged by Shi and colleagues to create a light-responsive electrical switch using a NIPAM and graphene oxide composite (**Figure 1.2d**)[36]. Other responsive hydrogels utilizing this mechanism have incorporated graphene oxide nanosheets[37-39], or carbon nanotubes[40, 41].

Another class of light-responsive hydrogels that are well-studied are the ultraviolet (UV) responsive hydrogels. This mechanism of action here still requires a chromophore with extinction at UV-wavelengths as well as nanomaterials that absorb in this range. Graphene oxide nanoparticles in particular have a strong absorption in the UV range, and can be incorporated into hydrogels to provide thermally triggered actuation as described above.

A commonly used moiety to drive light-to-force conversion is the azobenzene group. When irradiated at 300-400 nm, azobenzenes undergo a photo-isomerization that drives the conversion from the ground *trans* state to the excited *cis* state. This physically deforms the molecule (**Figure 1.2e**), and may also change its affinity for other molecules to create reversible host-guest interactions[42, 43]. One interesting example of a visible light driven responsive material using azobenzene photo-isomerization was reported by Takashima et al., where they showed that the interaction between azobenzene and cyclodextrin can be controlled with light, leading to reversible hydrogel actuation [43] (**Figure 1.2f)**. Another molecule used for photo-mechanical conversion is stilbene, which also undergoes photo-isomerization under UV irradiation and has been demonstrated in responsive hydrogel systems[44]. Interestingly, some of these azobenzene-based UV responsive materials also respond to longer-wavelengths (> 350 nm), such as blue lasers[43].

Of note, thermally and photothermally responsive materials exemplify the relationship between material size and the time of actuation response (**Figure 1.2g**). Zhao and colleagues conducted an analysis of representative publications in this field and found that larger-sized hydrogels require longer times to deswell. Specifically, the time constant of deswelling increases linearly with the square of the particle radius. They also note that optically heating hydrogel particles from the inside, as is the case for the optomechanical actuator particles, leads to a significant enhancement in the rate of deswelling that deviates from bulk heating of hydrogels. Fundamentally, a this relationship arises due to the rate of water movement in and out of the hydrogel system[45]. These results emphasize that the geometry of a responsive hydrogel and its mechanism of responsivity can both be used to program their response.

1.3.3 Chemical responsivity

Chemo-responsive hydrogel are a class of smart material that may respond to one or more of a broad array of chemical inputs. The response of these hydrogels may be triggered by ion concentrations or the presence of a specific molecule, or through more complex means such as enzymatic activity or oxidation-reduction reactions. In this section, we describe the mechanisms involved in each type of chemical responsivity including pH, redox chemicals, biomolecules, humidity and ionic strength.

1.3.3.1 pH responsive hydrogels

There are two major types of pH responsive hydrogels: proton-donors and proton-acceptors. A majority of proton-donor type hydrogels contain carboxyl acid[46-50] as the proton donor. When the environmental pH is less than the pKa of the material, proton-donating groups lose their charge, resulting in deswelling of the hydrogel. Proton-acceptor type hydrogels typically have nitrogen or metal complexes in their functional groups as proton acceptors, such as amines[50, 51], pyridines[52, 53], Fe^{3+}-catechols[54], and related molecules[55-57]. When the environment is more basic (pH>pKa), proton-*accepting* groups lose the positive charge and cause hydrogel deswelling.

The programmability of pH responsive hydrogels can arise from bottom-up assembly or top-down design. For example, Zarzar et al.[47] reported on the role of the architectural design of submerged hydrogel-actuated polymer microstructures (**Figure 1.3a**). These substrates with microposts or microfins, were first made by creating a mold in epoxy resin, then copolymerizing acrylic acid and acrylamide to create the pH-responsive structure. Due to the fact that acrylic acid has a pKa of 4.25, the hydrogel contracts at lower pH such that the microstructures are actuated and bend in one direction. All the micropillars bend to one side because the experiment employed unidirectional flow of the buffer within the microfluidic channel.

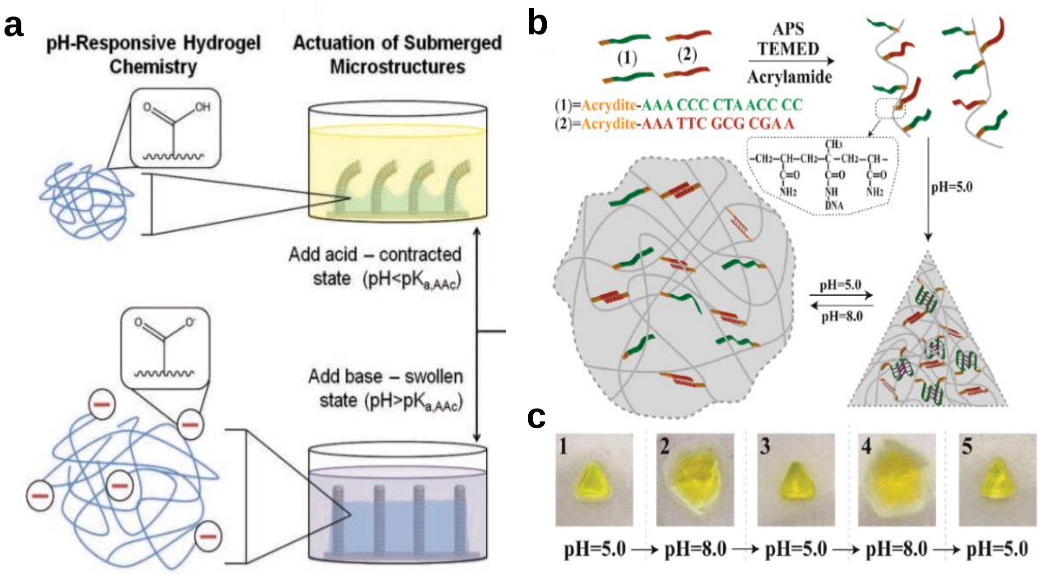

Figure 1.3. pH responsive hydrogels. a) A chip designed with polymer microstructures that is surrounded by a responsive hydrogel matrix. Micropillars on the chip deform in response to pH changes sensed by the responsive hydrogel, driving the actuation mechanism. Reproduced with permission[47]. Copyright 2011, Wiley-VCH. b) DNA crosslinked responsive hydrogel that have shape memory function in respond to different pH conditions. Decreased pH causes restructuring of the DNA base paring, resulting in deformation of the bulk gel. c) This effect is demonstrated to be highly reversible and repeatable. Reproduced with permission[61]. Copyright 2015, Wiley-VCH.

Another important class of pH responsive hydrogels are based on DNA hydrogels. These hydrogels show tunable pH responsivity that is controlled by the nucleic acid sequence. One example is reported by Gibson et al[58], in which the pH responsive DNA motif is formed by Hoogsteen interactions that form a triplex structure due to the protonation of the cytosine base[59]. The formation of the triplex motif mechanically brings two nanoparticles in physical proximity within the hydrogel which results in a shift of the spectra absorbance peak. In another example, it was reported that cytosine-rich domains form interlocking domains (i-motif) when the environmental pH drops to around 5.0[60, 61]. Such pH-responsive nucleic acids often incorporate C-rich motifs because the C bases have a pKa ranging from ~4 to ~6 and the protonation can disrupt the conventional Watson-Crick base pairings, and thus the protonated C nucleobases form C^+-C pairings instead of C-G pairings. This mechanism has inspired work where pH responsive hydrogels were created using DNA-crosslinked hydrogels. Guo et al.[61] reported the synthesis of shape memory hydrogel that are made of DNA-crosslinked polyacrylamide. Two different DNA crosslinkers cooperatively determine the swelling and deswelling states of the hydrogel. The first DNA strand forms crosslinkers at acidic (pH=5.0) conditions due to its cytosine rich sequence that forms an i-motif, while the other oligonucleotide is palindromic and forms crosslinks that non-pH responsive. At higher pH (8.0), the cytosine-rich DNA crosslinker denatures and the gel adopts a quasi-liquid form because of the reduced overall crosslinking density, and thus causing swelling of the hydrogel. However, when the pH is 5.0, the cytosine-rich DNA crosslinker strands are protonated reverting back into interlocking domains (i-motif), and therefore collapsing and recovering its original shape (**Figure 1.3b and c**). The interactions between protonated cytosine and other DNA bases provide a distinct toolbox to fabricate pH responsive hydrogels.

1.3.3.2 Oxidation-reduction responsive hydrogels

Redox (oxidation-reduction reaction) responsive hydrogels can be triggered by either by reducing/oxidizing reagents[62-67] or alternatively, such hydrogels can be triggered using an external electric field[68].

In general, redox reactions cause swelling/deswelling changes in hydrogels in two ways: altering the intrinsic hydrophilicity (hydration) of redox groups in the hydrogel, and/or by modulating molecular interactions between redox groups and other molecules in the hydrogel. The former aspect can directly change the swelling state through hydrophilicity, while the latter works to change crosslinking density or molecular assembly.

One of the pioneering examples of redox responsive hydrogel was developed by Yoshida et al., utilizing the Belousov–Zhabotinsky (BZ) reaction to drive the actuation of hydrogels[69]. BZ reactions are well known for their self-oscillating behavior, in which the catalyst ruthenium tris(2,2'-bipyridine) ($Ru(bpy)_3^{2+}$) is periodically oxidized into ($Ru(bpy)_3^{3+}$). In such responsive hydrogels, the ruthenium complex can be modified, such as with the addition of an alkene group, and then copolymerized with other monomers to make redox responsive hydrogels. Due to the fact that ($Ru(bpy)_3^{3+}$) is more charged than ($Ru(bpy)_3^{2+}$), the hydrogel follows ion fluxes produced by the BZ reaction to shrink and expand cyclically. This self-oscillating hydrogel was further programmed with a variety of shapes and asymmetric structures for different applications, such as autonomous mass transportation[63, 70], artificial cilia[71], and self-walking robots[72].

In addition to hydrophilicity manipulation as a result of redox reactions, the host-guest interaction is another mechanism of actuation in redox responsive hydrogels[67]. For example, the host-guest interaction between ferrocene and β-cyclo-dextrin (βCD) is one of the most well studied redox responsive host-guest pairs, where the two molecules associate and dissociate in different redox states, which can be harnessed to create actuation [66]. Nakahata et al.[64] reported a responsive hydrogel crosslinked through ferrocene/βCD pairs. In this system, oxidization of ferrocene caused the dissociation of the ferrocene/βCD pairs, lowering the crosslinking density of the hydrogel and therefore causing the gel to swell.

Recently, the library of redox responsive hydrogel has been further expanded. Novel molecular interactions such as donor-acceptor pairs[73] and π-stacking[62, 65] have been developed for redox responsive hydrogel. These mechanisms are working to address the slow kinetics and small volume changes exhibited in traditional redox responsive hydrogel [65], to create more significant and on-demand responsivity for future studies and applications.

1.3.3.3 Biomolecule responsive hydrogels

Biomolecule sensing is of great interest, particularly in the areas of diagnostics, biological sensing, and drug delivery[74, 75]. Biomolecule responsive hydrogels have been intensively reported over the past few decades, and a variety of responding mechanisms have been developed to detect the target biomolecules for different purposes. These materials generate a mechanical response to a variety of target molecules, such as glucose[76-79], enzymes[80-82], and DNA[83, 84], among others[85]. In general, the responsivity of these responsive hydrogels relies on engineering the hydrogel such

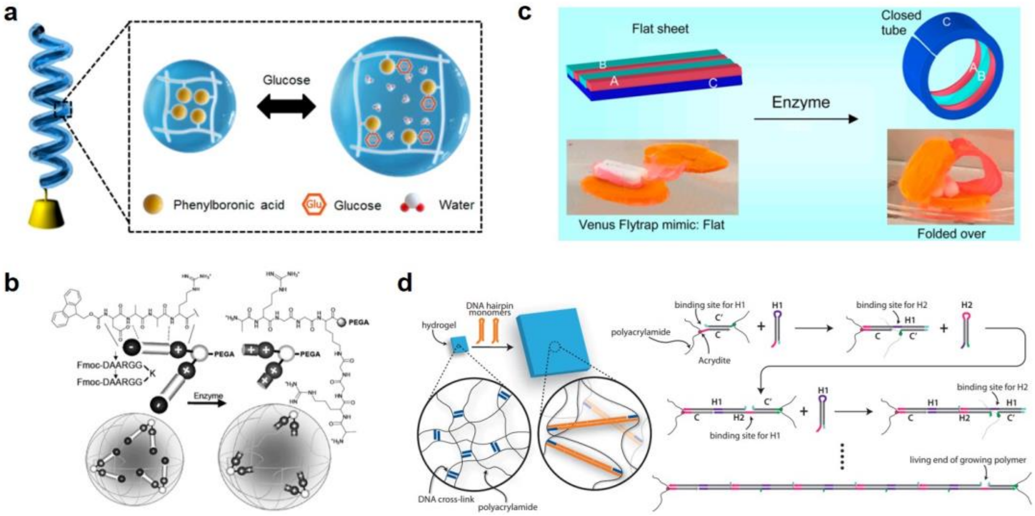

Figure 1.4. Biomolecule-responsive hydrogels. a) A glucose responsive hydrogel, comprised of a self-helical hydrogel fiber modified with phenylboronic acid groups that are repelled from each other in the presence of glucose. Readapted with permission[76]. Copyright 2020, American Chemical Society. b) An enzymatically actuated hydrogels, in which enzyme cleavage removes charge shielding groups and causes electrostatic repulsion within the polymer network, causing gel swelling. Readapted with permission[80]. Copyright 2009, Royal Society of Chemistry. c) A structurally programed responsive hydrogel with large amplitude of enzymatic response that induces curvature to the material in the presence of an enzyme, due to the multilayered structure of the hydrogel. Readapted with permission[82]. Copyright 2016, American Chemical Society. d) A sequence-specific DNA-responsive hydrogel, in which the presence of a specific target strand triggers a hybridization chain reaction resulting in large volume changes in the gel. Readapted with permission[83]. Copyright 2017, American Association for the Advancement of Science.

that it incorporates a specific molecular moiety that generates the response in the hydrogel. This biomolecule interaction typically results in changes of either the crosslinking density or the overall hydration of the hydrogel. In the following paragraphs we describe specific examples that harness this general concept.

Glucose is one of the most well studied target molecules for biomolecule responsive hydrogels[76-79, 86, 87], as the ability to sense and respond to glucose levels has expansive implications, from diabetes research to microbiology. Sim et al.[76] designed a self-helical hydrogel fiber made of a nylon core and hydrogel sheath modified with phenylboronic acid (**Figure 1.4a**), which can reversibly form bonds with glucose. Upon increasing the concentration of glucose to 1 M, the molecular complex formed by phenylboronic acid and glucose increases the overall hydrophilicity and water content which leads to swelling of the hydrogel sheath, and producing a maximum tensile strain of 2.3%. Once the glucose concentration drops, the responsive hydrogel can reverse the swelling response and recover its original mechanical properties. This particular hydrogel fiber design also has greater mechanical strength (~1 MPa) than other existing glucose responsive hydrogels due to the nylon core. This is just one example of a glucose responsive hydrogel that provides a new strategy for designing materials with greater durability.

Compared with other types of responsive hydrogel, enzyme-responsive hydrogels rely on the cleavage of specific moieties to modulate crosslinking density and hydration in hydrogel networks. This mechanism of responsivity has remarkably high specificity, but is irreversible. A slightly different example of an enzyme responsive hydrogel was developed by McDonald et al[80]. The cleavage of target peptide branches by thermolysin creates a more cationic polymer network, causing swelling (**Figure 1.4b**). Importantly, this mechanism is highly enzyme-specific, as the reported gel structures only responded to thermolysin, but not other enzymes such as chymotrypsin.

Though the density of branched peptide molecules in this gel system is relatively low, the volumetric change of enzymatic response could reach up to 30%. Athas et al.[82] reported enzyme responsive hydrogels with an even greater response amplitude (**Figure 1.4c**). In this work, the bulk gel was hybridized by three different "sub-gels" patterned in an asymmetric fashion. The enzyme collagenase specifically degrades the gelatin-based sub-gel at room temperature, creating a mechanical mismatch that caused bending towards the cleavage side.

Responsive hydrogels that can sense specific DNA oligonucleotide sequences are another class of functional hydrogels, which have advantages in terms of programmability compared to peptide and protein-based materials. Moreover, building materials with mechanical response to nucleic acid inputs has potential utility in diagnostics. For example, Cangialosi et al.[83] designed DNA responsive hydrogels with a photopatterned bilayer structure (**Figure 1.4d**). The hydrogel was crosslinked by DNA duplexes which triggered a hybridization chain reaction (HCR) in the presence of two specifically designed DNA hairpin targets. The HCR greatly increases the length of the double stranded DNA crosslinkers in the gel, inducing the swelling and actuating of the as-designed hydrogels. Although the responsive kinetics in this system were relative slow and the response was irreversible, the hydrogel was capable of nearly 100-fold volumetric expansion. To the best of our knowledge, this response represents the greatest volume change reported in a hydrogel material, and speaks to the large persistence length of double stranded DNA (~50 nm) and its high charge density.

1.3.3.4 Humidity responsive hydrogels

All hydrogels are, to some degree, mechanically responsive to changes in hydration state due to their defining high water content. However, some hydrogels are specifically designed to harness or amplify this water responsiveness. The responsive moieties of humidity-responsive hydrogels are mostly made of poly(ethylene glycol) (PEG)[14, 88-90] or polyethoxysiloxane[91]. Some of these humidity responsive hydrogels are quasi-hydrogels, where sensitivity to water is enhanced by reducing the original amount of water contained in the unactuated gel. In comparison to other chemical responsive hydrogels, humidity responsive hydrogels usually have a more rapid response (responding within seconds) and facile synthesis. The latter provides more possibilities for higher-level architectural programming, such as 3D printing[88, 92] and electrospinning[89]. Furthermore, since humidity responsive hydrogels tend to have less water content than common hydrogel materials, humidity responsive hydrogels demonstrate better mechanical performance in their strength, fatigue properties, and locomotive speed[14, 88, 93].

1.3.3.5 Ionic strength (IS) responsive hydrogels

Response behavior can be achieved in functional hydrogels by changing the ionic strength (IS) of their environment[94]. Theoretically, most polyelectrolyte-based hydrogels are IS responsive, such as poly(acrylic acid)[95], polypeptides[94], and alginate[19]. Generally speaking, the charge shielding effect of high-salt environments leads ionized groups in the hydrogel to have reduced charge repulsion, so that deswelling occurs in the bulk gel. However, only a few existing studies of responsive hydrogel focus solely on IS responsive behavior. Instead, many studies tend to introduce multi-responsive behavior that includes IS response[19, 95]. For example, a programmed interpenetrating network hydrogel with poly(acrylic acid) and poly(N-isopropylacrylamide) was reported by Shang and coworkers[95]. Poly(acrylic acid) can respond both to pH and ionic strength due to the presence of the carboxylic acid group. Note that the actuating kinetics of IS responsive hydrogels are in general slower than other response mechanisms like pH, temperature, or electric-triggered redox, taking 20-30 min to reach equilibrium[19, 94]. This is likely due to the hindered transport rate of different ions within the hydrogel network. Theoretically, the response kinetics are also affected by the specific size, shape, and chemical components of the hydrogel. IS responsive hydrogels with faster kinetics and better sensitivity are a promising direction for future studies in this area.

1.3.4 Magnetic field-responsive hydrogels

Magnetic field response is a simple and well understood method of remotely driving actuation[96, 97]. Magnetic field responsive hydrogels are mostly composites of hydrogels mixed with magnetic nanoparticles (MNPs). Typically, MNPs are entrapped, either covalently or non-covalently, within the hydrogel network of the material. When a magnetic field is applied, MNPs are drawn along the direction of the field, pulling parts of the gel structure with them. MNPs encompass a wide variety of magnetic nanostructures, including single particles, linear arrays, or 2D structures. The application of magnetic fields during the synthesis of magnetic responsive hydrogels can also direct the alignment of MNPs, programming the gel response by organizing the MNPs into isotropically or anisotropically aligned structures within the hydrogel matrix.

Responsive hydrogels with randomly distributed MNPs are among the most common magnetic responsive hydrogels, as they do not require extra steps during synthesis to align the particles [98-104]. Without any specific arrangement of the MNPs, the actuation of these hydrogels is simple, and the material moves toward the magnetic field. In contrast, spatially organizing the MNP can generate more specific responses that have an inherent directionality. Such patterned MNP-doped materials are discussed later in this section. A good example of randomly organized MNP nanocomposite was developed by Haider and coworkers[98] where they dispersed alginate coated Fe_3O_4 nanoparticles in a polyacrylamide hydrogel. The strength of the gel could be modulated through metal-cation crosslinking of the alginate components, here using Fe^{3+} to obtain an ultimate tensile strength of up to ~1MPa. Though increasing the nanoparticle content gradually decreased the mechanical strength, the magnetically responsive hydrogels had a larger response amplitude with the inclusion of more concentrated Fe_3O_4 MNPs. The magnetically responsive hydrogels would bend to the direction of magnetic field at any orientation, highlighting an advantage of remote controlling strategy. Similar work was conducted by Caykara et al[99], where MNPs were randomly distributed in a poly(N-tertbutylacrylamide-co-acrylamide) hydrogel matrix, creating a magnetically actuatable composite.

Though magnetically responsive hydrogels can be directly actuated by magnetic force, a slightly more complex mechanism to create magnetically responsive hydrogels is to incorporate MNPs with thermal responsive polymers, such as pNIPAM. By applying an alternating magnetic field (AMF), heat is produced by MNPs that triggers the thermal response of the hydrogel matrix[97, 105, 106]. Satarkar et al.[105] fabricated such a Fe_3O_4/pNIPAM hydrogel composite. Upon application of AMF, the hydrogel collapsed and the microfluidic channel was toggled to the open state. They further demonstrated the responsivity of this material could be tuned by MNP content and programmed geometry. In comparison with direct magnetic field actuation, the AMF-triggered, indirect thermal response of magnetically responsive hydrogels tends to have larger actuation magnitudes.

Offering more precise movement control, magnetically responsive hydrogels with organized MNPs represent an emerging area in magnetically responsive materials. MNPs can be pre-aligned prior to hydrogel formation by applying an external magnetic field, then polymerizing the hydrogel to freeze the MNP spatial arrangement into the gel network. Huang et al. [107] reported the fabrication of hydrogel-based soft robot with programmable moieties, in which a “head” and “tail” region were separately programmed with different alignments of MNPs during the photopatterning of the bulk gel. The authors found that the orientation of MNPs dictated the self-folding behavior of the different moieties, which determined the final morphology of the material. The hydrogel architecture (helical tail vs. flat tail) and magnetic field rotation were found to affect the movement velocity of the designed soft robot, creating a highly programmable responsive hydrogel design.

Magnetically responsive hydrogels programmed by the alignment of MNPs demonstrate a practical way of fabricating functional soft robots with different geometries and propulsion styles. Compared to those with randomly aligned MNPs, responsive hydrogels with organized MNPs show great promise in developing more sophisticated responsive hydrogels with programmable function.

1.3.5 Electrical field

Electrical field responsive hydrogel are usually responsive to one of two types of electrical stimuli either static or redox-based. For static electrical stimulation the physical deformation of the hydrogel directly results from the application of an electrical voltage[108-110]. In contrast, the redox-based hydrogels include a redox active group within the hydrogel that undergoes an electrochemical reaction by an applied electric field[68, 111]. Examples of such materials are given in **Figure 1.5**, and the unique mechanisms and advantages of each type of electrical field responsive hydrogels are described below.

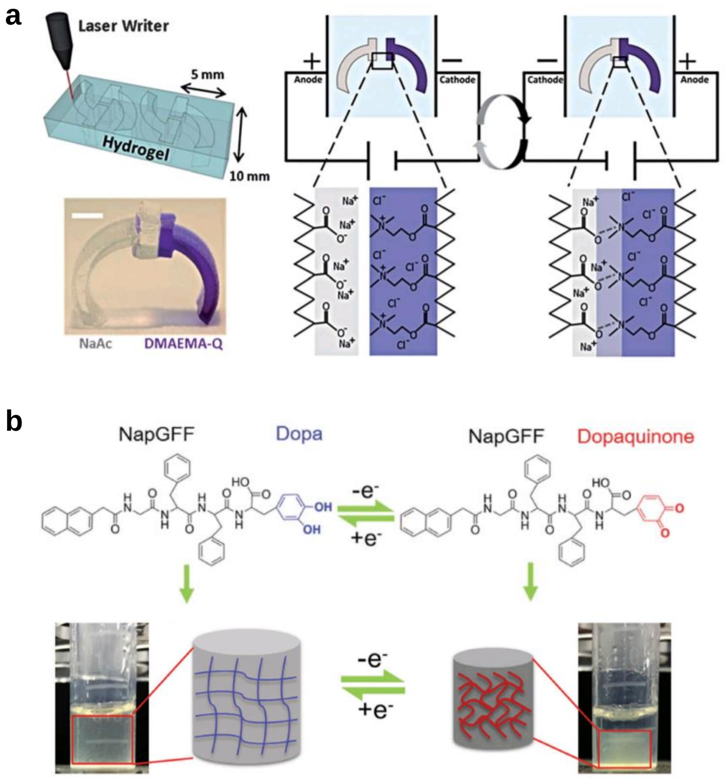

Figure 1.5. Electrical field responsive hydrogels. a) A two "leg" self-walking hydrogels, fabricated using top-down design, with different "legs" that respond to electrical field direction, resulting in locomotion. Readapted with permission[112]. Copyright 2014, Royal Society of Chemistry. b) Structure and function of dopa-based hydrogels, in electrical power induces a redox reaction that deswells the hydrogel. Readapted with permission[68]. Copyright 2016, Wiley VCH.

1.3.5.1 Static type

Static type responsive hydrogels are triggered by the formation of osmotic gradients when the material is exposed to static electric field. In these cases, polyelectrolytes in a material, such as salts, are electrostatically attracted to oppositely charged electrodes. This disrupts the chemical equilibrium within the material, and causes a difference in osmotic pressure throughout the material. Water is then drawn along the osmotic pressure gradient, resulting in anisotropic swelling of the hydrogel that causes material bending.

The bending behavior of static type responsive hydrogel can be programmed through the types of polyelectrolytes in the system (i.e. polyanions or polycations). For example, an electrically actuated hydrogel walker was developed by Morales et al[112]. The two "legs" of this hydrogel were made of poly(acrylamide-co-sodium acrylate) and poly(acrylamide-co-quaternized dimethylaminoethyl methacrylate), respectively. Upon switching the electric field direction, the different legs switched between bending in a "pushing motion" and "pulling motion", working like "legs" to propel the walker forward (**Figure 1.5a**). This chemical and geometric programming of the two legs allows the hydrogel walker to keep moving without relying on ratcheted surfaces or specific external conditions that other soft robotic walkers typically employ. The response of hydrogel can also be programed by the presence of counterions to drive differential responses under certain conditions. Jiang et al.[113] studied the bidirectional bending behavior of electric responsive hydrogels that were made of a copolymerized hydrogel of acrylic acid and N,N-dimethyl acrylamide. This copolymerization combines both polycation and polyanion together, and this resulted in a bidirectional bending behavior. This was found to be due to differential movement speeds of counterions such as H^+ in the system, and the kinetic difference in this counterion migration induced the bidirectional bending.

Recently, studies have begun focusing on making nanocomposite hydrogel with electrically conductive materials such as graphene[114-116] and carbon nanotubes[117, 118]. Two main benefits of making nanocomposites with conductive materials have been identified in the literature. First, the inclusion of conductive materials increases the charge transport rate inside the hydrogels, leading to more rapid response kinetics. Additionally, nanocomposite hydrogels show better mechanical strength than responsive hydrogels without these modifications, though this may hinder the actuation of hydrogel at higher concentrations[118]. Thus, optimizing the content of conductive nanomaterials is important for electric responsive hydrogel to obtain better electrical responding performance.

The static mechanism of responsive hydrogel response also has the advantage of giving remotely controlled actuation, similar to light responsive or electric responsive. However, the remote control of responsive hydrogel is less convenient than other remotely actuated hydrogel, due to the specific requirement of salts in the solution.

1.3.5.2 Redox type

In contrast to the static type, redox-type electric responsive hydrogel use an electrical current to drive a redox reaction within the hydrogel. This modulates the charge and the hydration state of the material, resulting in actuation. Importantly, this mechanism is distinct from the chemically-triggered redox responsive hydrogels introduced in Section 1.3, as the electrons necessary for reduction are provided by electrical current, not chemical reactions. However, the response of redox-type responsive hydrogel is most similar to that of the chemically responsive hydrogel.

For example, Xue et al.[68] reported a supramolecular peptide hydrogel that can be actuated by electrically-induced redox reactions. The hydrogel was modified with dihydroxyphenylalanine (dopa) as the redox active moiety that can be oxidized into dopaquinone through electrochemical reaction **(Figure 1.5b).** The oxidation of dopa greatly decrease hydrophilicity of the material, causing hydrogel deswelling that was easily reversed by reducing the dopaquinone back to dopa electrochemically. The actuation of these types of hydrogels does not necessarily rely on the polyelectrolyte composition of the medium, which can be an advantage in certain systems over static-type hydrogels.

In both mechanisms of electric response, the electrochemical stability of the material under the applied voltage must be considered, which can limit some of the possible material components and applications. However, these considerations are necessary to avoid the production of undesired byproducts or permanent damage to the hydrogel, both of which could potentially compromise the reversibility of hydrogel materials.

1.3.6 Bioactuation

A novel example of programming hydrogel responsivity is the incorporation of biological components, such as cells or bacteria, to drive mechanical actuation. This is most often accomplished using muscle cells, with cardiac and skeletal tissues each having unique responsivity[119, 120] . Both cell types work by creating an electrochemical potential, called an action potential, across the surface of the cell. This triggers an intracellular calcium release, which promotes binding of myosin motor proteins to actin fibers. Myosin then consumes ATP to pull on the resultant complex, resulting in mechanical force on the material that can be up to mN[121].

The stimulus to which these hydrogels respond is programmed by the cell type that is included. Actuators that require spontaneous contraction often employ cardiomyocytes, which generate their own action potentials and will continue to actuate in the presence of glucose as an energy source[122-124]. Cardiac-derived muscle cells are also responsive to electrostimulation, and many of these “bio-hybrid” hydrogels utilize microelectrodes to achieve a more controlled force producing response. While spontaneous contraction of skeletal muscle can occur[119], it is not as regular and reliable as that of cardiac tissue. Therefore, skeletal muscle-based bioactuator materials tend to rely on electrostimulation to produce forces[125, 126]. However, this provides more control and programmability of the response, allowing for the actuator to be stopped and started as necessary, and to tune the frequency and magnitude of actuation.

Bioactuators offer unique advantages and challenges as compared to other responsive hydrogels. One notable limitation is the necessity to maintain the cellular component of these structures in a medium that provides glucose, salts, and other supplements, and preventing metabolic wastes from accumulating to toxic levels. These factors do, however, make bioactuated hydrogels particularly well-suited for biomedical applications, such as those discussed in following sections.

1.3.7 Mechanical force-responsive hydrogels

In order to be responsive to external mechanical forces, different hydrogels have been programmed with different signal outputs, including structural color[127, 128], voltage production[129], changes in electrical resistance[130], and fluorescent signaling[131].

Photonic crystal (PC) embedded hydrogels are naturally responsive to mechanical force. The programmability of the hydrogel is determined by its crystal constant, a parameter related to the size and distance of periodic structures within the material. Tuning this crystal constant can allow for the production of structural color within the visible spectrum, making even small applied forces easy to identify. Any stretching, pressing, poking, or bending changes the distance between repeating units of the photonic crystal, therefore inducing this chromatic switching[128], making PC responsive hydrogel a facile tool to identify externally applied forces.

Förster resonance energy transfer (FRET) is a fluorescence technique that has been broadly used to measure forces and distances in scientific studies[132-136]. Since the application of external force results in hydrogel deformation, this deformation may change the distance between two fluorophores embedded in the gel network[137]. This hypothesis was tested by Merindol et al.[131] by synthesizing a DNA-based hydrogel with FRET pairs that are non-covalently bound together. Stretching of the hydrogel separates the quencher and fluorophore and leads to a FRET-based fluorescence change that is used for imaging force density within the gel.

In addition to producing a light or color signal that can be easily observed by eye, mechanical responsive hydrogels that can output electrical signal have also been developed for integration into electronic devices. This electrical signaling includes producing voltage or changing resistance. These materials, known as triboelectric materials, are of great interest for mechanical force sensing and energy conversion. In one example, He and colleagues generated a polyacrylamide/silk fibroin composite hydrogel that detected a wide range of strains and compressions and responded by changing its electrical resistance as well as output voltage signal[138]. Despite their sensitivity, these triboelectric hydrogel materials can only indicate the magnitude of an applied force, and cannot provide spatial information regarding the force location. Nevertheless, triboelectric hydrogel materials could represent an important mechanism in future applications, such as soft wearable devices.

1.3.8 Multi-responsive actuating systems

Recently, the concept of multi-responsive hydrogels, those with responsivity to several stimuli rather than just one, has been studied with increasing depth[139-149]. Generally, the broad responsivity of such hydrogels is programmed by combining different responsive moieties together in one material system, which brings increased material complexity but also new applications for hydrogels.

There are three major approaches in the existing body of literature toward designing hydrogel materials. The first approach is copolymerization of different functional monomers or oligomers. For example, Sun et al[139] synthesized poly(N-isopropyl acrylamide-co-acrylamide) and poly(2-(dimethylamino)ethyl methacrylate-co-2-acrylamido-2-methyl propane sulfonic acid) to create a multi-responsive hydrogels sensitive to temperature, pH, and salt concentration. The second approach is to combine hydrogels with different responsivity together physically, rather than chemically, in order to "add up" their responsivities in the resultant multi-responsive hydrogels. This method includes making hydrogels with multiple parts or layers of different hydrogels[140, 141], or by building interpenetrating polymer networks of responsive polymers[142]. The final approach is to synthesize hydrogels doped with various nanomaterials, such as graphene[143, 145, 146], Fe_3O_4[144], carbon nanotubes[148], and others[149]. These nanostructures can confer responsivities to the hydrogel matrix surrounding them, such as the carbon nanotube-containing responsive hydrogel designed by Li et al. that responds to light, electricity, humidity, and volatile organic compounds [148]. Importantly, these three approaches are not exclusive to each other, and these approaches are often combined to create multi-responsive hydrogels.[139, 140, 143]

The multi-responsive hydrogels open a new gateway for high-level design of multi-responsive hydrogels for more complex applications. While most of the "primary responsivities" have been well-studied, studying the integration of the multiple responses and enhancing precision in controlling them is a broad horizon in the future of programmable multi-responsive hydrogels.

1.4 Applications

Functionally responsive hydrogels encompass a wide variety of materials, sensitivities, and synthesis techniques that all work to program certain responses. Each unique combination of these factors creates a hydrogel with specific advantages and disadvantages that dictate how that material can be used. Here, we discuss the applications in which certain responsive hydrogel have been demonstrated in the scientific literature, and their implications for future work in the field.

1.4.1 Towards Soft Robotics

A traditional robot is defined as a machine that is capable of carrying out a complex series of actions automatically[150]. Soft robotics represents a nascent sub-field of traditional robotics where the robot is primarily comprised of a compliant or soft material that aims to emulate biological systems.[151-158] There is some controversy in the field as how to distinguish a soft matter actuator from a soft robot. For some researchers, a soft robot is indistinguishable from a soft actuator[159-161], while for others soft actuators are a functional component of a soft robot[162-164]. In this thesis, we will adopt a more strict definition of a soft robot as a sophisticated system that includes one or more soft actuators to generate a series of actions. Based on this definition, the vast majority of work self-described as “soft robotics” is more formally soft actuators. Regardless, we see these more complex hydrogel actuators as a step toward constructing soft robotic systems in the near future. In this section, we introduce responsive hydrogels that may become components of soft robotic systems through three of the most common actuation approaches: magnetic, biological, and pressure-based actuation.

1.4.1.1 Toward Magnetically Actuated Robotic Systems

Magnetic actuation of robotic systems is well-suited for this application because it affords a convenient method for remote and untethered actuation of hydrogels that has been favored in past studies.[144, 154, 158] The magnetic actuation can be further classified as paramagnetic actuation and ferromagnetic actuation. For paramagnetic actuation, the hydrogel robots are exclusively attracted to the direction where magnetic field is greatest. This process does not distinguish the polarity of the magnetic field. For example, Tang et al.[152] reported a “DNA robot” with magnetic field driven navigational locomotion (**Figure 1.6a**). The paramagnetic particles incorporated

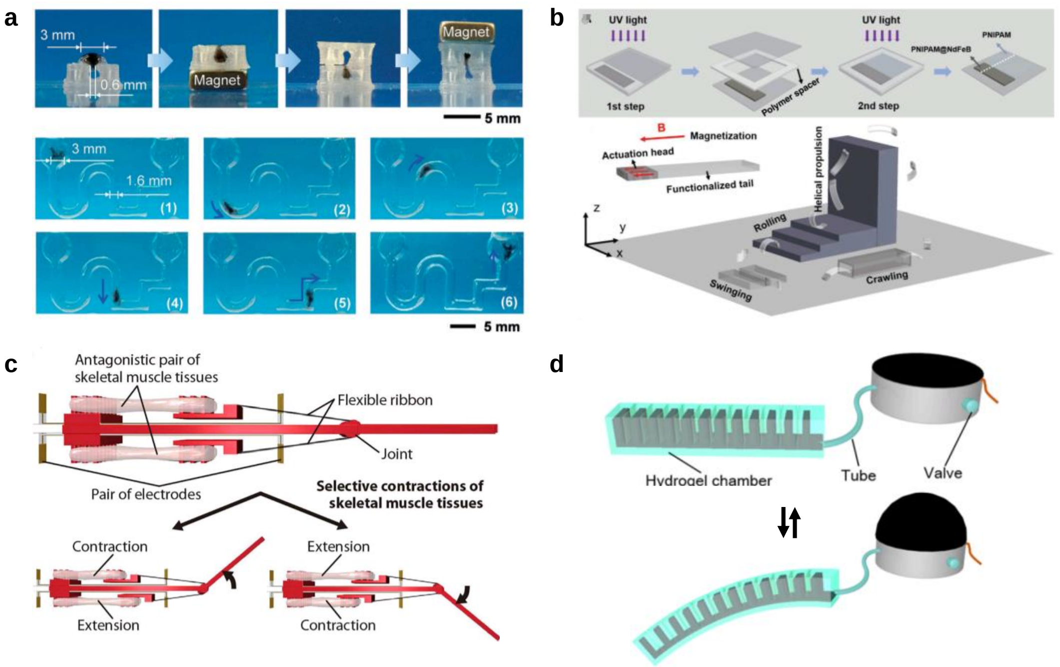

Figure 1.6 Soft "robot" with different actuating mechanisms. a) An example of a paramagnetic DNA hydrogel soft robot with magnetic field-driven navigation of its locomotion. Readapted with permission[152]. Copyright 2020, Wiley-VCH. b) A ferromagnetic hydrogel embedded with NdFeB particles. The hydrogel material is pre-magnetized during fabrication to develop the ferromagnetic response, resulting in a more sophisticated moving behavior of the soft robot under a magnetic field. Readapted with permission[153]. Copyright 2020, Wiley-VCH. c) A bio-actuated hydrogel comprised of a muscle cell-laden Matrigel scaffold. Actuation of this hydrogel is activated by applying electrical stimulation with embedded gold electrodes, triggering contraction of the cells. Readapted with permission[156]. Copyright 2018, American Association for the Advancement of Science. d) A hydrogel robot designed with asymmetrical cavities that change shape under varying hydraulic pressure, resulting in material bending. Readapted with permission[157]. Copyright 2018, IOP publishing.

within this DNA hydrogel provide efficient actuation, while the DNA network provides elasticity and biocompatibility. The soft and deformable hydrogel robots were also demonstrated to move through confined spaces, showing potential applications for drug delivery.

For ferromagnetic actuation, the hydrogel robots are sensitive to the polarity of the magnetic field. This sensitivity increases the complexity of the robot's actuation and enables diverse multimodal locomotion. For example, a “milli-robot” with a ferromagnetic head and thermo-responsive tail was reported by Du et al[153]. The head is made of a pNIPAM hydrogel with NdFeB microparticles which were magnetized by a strong external magnetic field. The resultant magnetization and magnetic coercivity of NdFeB particles ensure the ferromagnetic properties of the millimeter sized “robots”. Diverse multimodal locomotions, such as crawling, rolling, swinging, and helical propulsion, were observed and studied (**Figure 1.6b**).

1.4.1.2 Toward Biologically Actuated Robotic Systems

Bio-actuation is a fascinating yet challenging approach to fabricate hydrogel robotics. By incorporating mammalian cells or bacteria, hydrogel robots can be actuated by harnessing the power produced by these biological systems. This does, however, require that the hydrogel be biocompatible and have sufficient structural stability for the cells and bacteria to attach to. A self-swimming microbial “robot” has been created and reported by Higashi et al.[155]. Flagellated bacteria were attached onto the tail of a hydrogel made of bacterial cellulose, and the flagellar beating provided the desired motility of the responsive hydrogel. The self-swimming microbial robot demonstrated a moving speed of 4.8 μm/s. However, one disadvantage of microbial robot is that the direction of locomotion is arbitrary, because it is difficult to direct the movement of bacteria. A more delicate bio-actuated hydrogel robot was developed by Morimoto et al.[156] In their work, skeletal muscle cells were loaded onto Matrigel (a biologically derived hydrogel polymer), and the contraction of the cultured muscle tissue was controlled by applying electrical stimulation with gold electrodes (**Figure 1.6c**). In this way, the bio-actuated hydrogel “robots” was directly guided by the electrical signal input. The “robot” also showed large actuation amplitudes (~90°) and the biological components remained viable for over a week.

1.4.1.3 Toward Pressure Actuated of Robotic Systems

Pressure actuation refers to the locomotion of soft robotic materials caused by altering fluid pressure inside the responsive hydrogel. This kind of soft robot usually has an asymmetrical cavity inside that produces anisotropic force, which determines the direction of the actuation and locomotion. This strategy has already been widely adopted in non-hydrogel robotic systems[165]. However, its implementation in hydrogel actuators is challenging, due to the mechanical softness of hydrogels that may deform or rupture under pressure changes. At least one group has addressed this concern though, as Zhang et al. strengthened alginate hydrogels by physically crosslinking polyacrylamide into the composite network[157]. The hydrogel was programmed with this characteristic asymmetric cavity, which caused bending under hydraulic pressure (**Figure 1.6d**). This hydraulic pressure-driven hydrogel “robot” was demonstrated to grip a 7 grams cylindrical simulated cargo underwater.

1.4.2 Biomedical Applications of responsive hydrogel

Responsive hydrogel materials can be widely applicable in the biomedical sciences. From precise mechanical stimulation of cells to moving drugs toward their targets, responsive hydrogels have important applications in medicine as well as research and provides a unique example. Many of the response mechanisms of these materials, such as thermal, IR, or magnetic stimulation, are compatible with *in vivo* and clinical work. The programmability of the material responses also makes them favorable for research applications, where specificity and spatiotemporal accuracy can enhance our understanding of biology at a molecular level. Here, we discuss some of the promising new work employing responsive hydrogel in the biomedical sciences.

1.4.2.1. Responsive hydrogel toward the study of cell biology

Hydrogel have been used for decades in biological research, with one of the earliest applications being the use of NIPAM-coated cell culture plates for temperature controlled, non-enzymatic cell release[166]. More recently developed applications leverage the benefits of specific polymeric actuators, such as biocompatibility, ease of modification, and spatiotemporal control of response, to study the roles of mechanical stimuli in cell biology. These technologies can be applied to multiple cell types and cellular processes. Advances in microfabrication have allowed for integration of actuators into “on-chip” devices, including a recent example of a thermos-responsive actuator capable of single-cell mechanical manipulation, placing programmable hydrogel actuators on the forefront of biological research techniques[167].

Actuatable hydrogels are able to profoundly influence biology, particularly in cell types that are known to exist in mechanically active environments, such as cardiac, musculoskeletal, and orthopedic tissues. Magnetically responsive hydrogels have been used to mechanically stimulate stem cells, directing their maturation toward the osteoblastic lineage[168]. Electrostimulation of a carbon nanotube-impregnated composite hydrogel has also been shown to direct skeletal muscle growth and differentiation.[169]

Light-responsive hydrogels are particularly advantageous for cell studies, as they allow one to control mechanical inputs at higher spatiotemporal resolution than that afforded by bulk bioreactors, which are the current standard in the field. One example of this is the optomechanical actuator (OMA), a light-responsive hydrogel particle developed by Salaita et al. The OMAs, pNIPMAm-AuNR composites nanoparticles that collapse when exposed to 785 nm NIR light, apply mechanical stimulation to cells through modification of their surface with cell adhesion ligands. In these studies, mechanical stimulation with these hydrogel particles enhanced differentiation and alignment of muscle progenitor cells[33], fibroblast actin polymerization, and T cell calcium signaling[32]. In the study of muscle cells in particular, the spatial resolution afforded by light responsivity as opposed to other hydrogel response mechanisms allowed for study of differentiation mechanisms on a sub-cellular level. Using light also avoids confounding biological effects, as some chemical as well as electrostimulation have been known to influence muscle cell growth.

A final application of responsive hydrogel in cell biology is studying cancer mechanobiology. Solid tumor cells are known to be influenced by local mechanical conditions in the body. Researchers have quite recently begun to incorporate actuating materials with the ability to specifically program responses to study cancer biology in this way[170]. Lim et al. used a bilayer, thermoresponsive hydrogel material to apply periodic compressive forces to tumor cell clusters, enhancing growth factor and angiogenic factor expression and providing novel insight into the role of force in tumorigenesis.

Using responsive hydrogel to study the role of mechanical forces in cell biology is still an emerging approach with these materials. However, as the focus in this field continues to turn toward providing the most biomimetic environment for cells *in vitro*, the incorporation of mechanical forces with programmable and multi-responsive hydrogels will offer novel insight into development and disease.

1.4.2.2. Tissue engineering applications of hydrogel materials

As in cell biology, the field of regenerative medicine is beginning to turn to programmable hydrogel actuators as biomaterials to promote tissue growth and healing. Natural tissues such as lung, muscle, and endothelial cells are subject to highly dynamic mechanical environments.

However, current tissue engineering scaffolds are static and hence poorly reproduce this dynamic property of natural tissues. Responsive hydrogels offer a solution by provide a material with tunable mechanical properties. While the use of responsive hydrogels *in vivo* is limited at this time, this field will likely expand as researchers seek mechanisms to apply hydrogel toward solving clinical challenges. These applications leverage the biocompatibility of gels and polymers with their tunable mechanical and chemical properties to promote tissue formation through therapeutic force application. A current example of responsive hydrogels used for tissue regeneration is the biphasic ferrogel, an alginate-based hydrogel material impregnated with iron oxide nanoparticles. Under an oscillating magnetic field, implanted gels applied cyclic mechanical loading to the tibialis anterior, and were able to enhance healing in a mouse muscle injury model[171]. As the tissue engineering field continues to grow, responsive hydrogels offer an opportunity to incorporate the dynamics of the physiological environment for enhanced biomimicry.

In another study, 4D printing was used to create hydrogel structures containing mouse stromal cells that would change shape from a sheet to a tube conformation in cell media. While creating microtube structures challenges the spatial resolution of current printing technologies, the rolled geometry resulting from printing a capillary-like structures with internal diameters as small as tens of microns, opening the door to incorporate vascularization in future tissue engineered constructs[172].

1.4.2.3. Responsive hydrogels as drug delivery vehicles

Another notable application of responsive hydrogels in the biomedical sciences is drug delivery. It is important to distinguish between non-mechanically mediated drug release mechanisms and mechanically mediated drug delivery platforms, even though sometimes, this distinction is subtle. For example, protease-mediated degradation that releases a drug bound to a hydrogel matrix is not necessarily mechanical[173]. However, if a enzymatic activity changes the hydrophilicity or crosslinking density in a polymer, leading to hydrogel swelling that allows for release of an entrapped drug[174], then this includes a mechanical component. Other examples of mechanically driven drug delivery include hydrogels that physically "grip" the drug, and can be triggered to release it at a certain site. Here, we highlight several examples of responsive hydrogels in drug delivery that satisfy this distinction from classical delivery mechanisms.

The high degree of programmability and specificity of response conditions makes hydrogels optimal for carrying drug molecules to specific sites in the body and releasing these drugs under either native or remotely triggered conditions. Remote triggering of drug localization and release is highly desirable in medical applications, providing high specificity of delivery without invasive procedures. Many remotely actuatable hydrogels are compatible with biomedical applications, such as magnetic. Cezar et al. applied the biphasic ferrogel, a hydrogel material containing a gradient of iron oxide for programmed magnetic responsiveness, for controlled release of the chemotherapeutic drug mitoxantrone, as well as release of cells for therapeutic purposes[175, 176]. Other groups have employed NIR-driven molecule release as a remotely actuated delivery mechanism, using light to physically deform the hydrogel delivery system and release chemotherapeutic agents at a targeted site [124, 177].

While remote actuation through light or magnetic field manipulation is viable in some scenarios, another desirable mechanism for drug release is through sensing and self-actuation of the material without external intervention. This allows the drug to be released when and where a programmed stimulus is present, even deep inside the body where external stimulation methods would be ineffective. Indeed, prevalent areas of research for these materials are in the gastrointestinal system, where dramatic changes in pH at various stages provide a stimulus to swell hydrogels and trigger drug release[178]. Similarly, such materials can protect protein therapeutics, such as insulin or antibody treatments, from the denaturing environment of the stomach, providing a potential to increase efficacy and remove the need for injections of such drugs[179, 180]. Chemical responsiveness can also be used to monitor and treat conditions. Li et al. developed a multi-responsive hydrogel containing the enzymes glucose oxidase and catalase, and an insulin drug payload as a potential diabetes therapeutic. In the presence of glucose, the enzymes create a local pH change that unfolds the protein hydrogel, releasing insulin[181].

By providing the ability to specify the location and conditions of drug release, the unique properties of hydrogels can remove off-target side effects and increase drug efficacy by ensuring delivery to the appropriate tissue. One example that combines the controlled release of programmable hydrogel materials with their ability for active transport is a recent design of a bio-hybrid robot for chemotherapeutic delivery. A bio-actuated cardiomyocyte-laden hydrogel structure was designed move through a fluid medium, powered by the spontaneous contraction of the embedded cells. At specific laser illumination sites, the construct released its drug payload through photothermal actuation, allowing it to target specific cells in a monolayer[124]. These examples indicate a strong future for responsive hydrogels in drug delivery, where their programmable specificity is a desirable characteristic to remove off-target side effects of drugs while ensuring efficient delivery to targeted cells.

1.4.3 Responsive hydrogels as smart skin materials

Although responsive hydrogel materials can respond to a wide variety of inputs, but are unique in their applications and design. In general, smart skin hydrogel materials are thin, mechanically robust, compliant, and sometimes biocompatible. For example, this dissertation will describe a strain-accommodating smart skin that is made from hydrogel materials in **Chapter 2** [128]. Similar to the skin structure of the chameleon, the force generated by responsive domains in the changed the lattice space of photonic crystals. Compare to conventional chromatic responsive smart skins, which often results large volume change, our design applies a secondary strain-accommodating matrix to accommodate the photonic crystal (PC) domains. According to both computational and experimental results, the strain-accommodating matrix absorbs the strains produced by the PC domains, allowing the bulk material to remain a constant size. This multi-responsive, strain-accommodating smart skin material is very promising for applications such as camouflage, sensing, and anti-counterfeiting.

Another example of a hydrogel-based smart skin is the triboelectric, energy-harvesting skin reported by Liu et al.[129], in which the smart skin is considered as a convenient mechanoresponsive electric generator. When applied to the skin, the responsive hydrogel senses bending or stretching, and converts this mechanical energy to electricity through the deformation of dielectric polymers. This concept of harvesting the energy of everyday motion into electricity is a novel application for which hydrogel-based smart skins are uniquely suited. It is likely even more work will be conducted in this area, integrating the fundamental synthesis of smart skins with top-down design parameters to further explore the practical applications of these responsive hydrogel materials.

1.5 Aim and scope of this dissertation

The aim and scope of this dissertation will focus on addressing three specific challenges on responsive hydrogel design. The first aim is to design a strain-accommodating hydrogel material.

Because most responsive hydrogel materials have swelling/deswelling behavior as an output response, the volumetric change (material strain) of hydrogel material seems unavoidable. The volumetric change could be a disadvantage in certain applicational scenarios such as smart skins. Therefore, the first project focus on resolving the strain issue of hydrogel materials upon responding. Inspired from the case of chameleon skin, we realized that large strain of responsive hydrogel could be accommodated with segmented/discontinuous structure.

The second aim is to design an on-demand assembly mechanism for a responsive hydrogel nanocomposite. The concept of on-demand assembly refers to the reassemble of nanomaterial within hydrogel networks. In most cases, fabricating nanocomposites that are embedded with assembled colloidal nanoparticles require pre-alignment (by gravity; magnetic field; electric field; etc) of the nanoparticles in hydrogel precursors. The alignment/organized structure will be permanently fixed inside the polymer networks when the hydrogel is formed. It is very challenging to reorganize the alignment of nanomaterial in hydrogel networks. We seek to design a responsive hydrogel system that could temporarily unlock its physical barrier so that the particle reassembly could happen.

The third aim is to design a bio-compatible hydrogel matrix that can detect cellular force in piconewton level. It is well known that the mechanical force determines the fate and function of cells such as cardiac muscle cells, T-cells, and platelet. The well-developed molecular tension fluorescence microscopy (MTFM) provides a high-resolution approach for cellular tension measuring. However, most of the MTFM was tested on a glass surface, which is far from a physiological environment. For example, the Young’s modulus of a typical glass surface is ~47Gpa, which is significantly stiffer compare to a human skin tissue (100kPa-10Mpa). Testing the cellular tension on a non-physiology surface may fail to reflect true mechanical force that a cell exerted in a tissue environment. Therefore, there is a need to develop a hydrogel based MTFM surface for cellular tension measurement. We seek to design a stiffness tunable and bio-compatible hydrogel surface for this aim.

CHAPTER 2. CHAMELEON INSPIRED STRAIN-ACCOMMODATING SMART SKIN

2.1 Introduction

Many living creatures have evolved the ability to change color, such as chameleons[182], neon tetra fishes,[183, 184] and Morpho Sulkowskyi butterflies[185, 186]. The ability to rapidly change color is beneficial for camouflage, mating, and intimidating predators. Coloration in these organisms is described as "structural" because it is generated by periodic arrays of nano- and micro-structures, known as photonic crystals (PCs), which generate color through optical interference effects. Unlike common coloration strategies using dyes and pigments, which rely on wavelength-specific absorption of light, structural coloration is immune to photobleaching and can be easily manipulated by controlling particle spacing as opposed to synthetic strategies. In accordance with Bragg's law of diffraction,[187, 188] the periodic distance between elements in these natural PCs dictates the color of the material. Accordingly, the mechanism of dynamic color change for many of these species employs responsive matrices that tune the spacing of the PCs.

Inspired by natural examples, there has been significant effort focused on generating synthetic responsive PC materials that can change color on demand.[189-194] Such color-changing materials, which are sometimes described as "smart skins", are envisioned to become important in various applications ranging from camouflage and communications to anti-counterfeiting and biosensing. The fundamental mechanism for adjusting the color of synthetic PCs mirrors that of natural systems and requires modulating the periodicity of the PC lattice using an "accordion" mechanism.[195-198] This strategy is usually realized by embedding the PC in a hydrogel[199-202] or flexible polymer matrix[203, 204] that responds to an input by expansion or contraction, resulting in a shift in the PC periodicity. The major problem with this accordion strategy of creating artificial smart skins pertains to the large volume change, which leads to structural instability and buckling of the material.[205, 206] For example, a 20% or greater linear expansion or contraction (strain) of a responsive PC is required to produce a significant color shift ($\Delta\lambda$=100 nm). This magnitude of strain and deformation impedes their application and adoption. However, this led us to consider how color-changing animals, such as chameleons address this problem (**Figure 2.1a**). Based on recent time-lapse imaging of chameleon skin,1 we noticed that only a small fraction of the skin cells contain the guanine PC arrays, while the remainder of the skin cells are colorless. In other words, chameleon skin tissue included non-responsive cells that may contribute to reduce the global volume change during chromatic response.

This general concept is shown in **Figure 2.1b**, which highlights the contrast between artificial responsive PCs that have been extensively studied, and natural responsive PCs, which employ a tunable PC element embedded within a matrix that lacks PCs and accommodates the strain. This structural difference, which was shown in natural responsive PCs, leads to a significant reduction in the total change in volume of the material, while maintaining the observable dynamic coloration.

Herein, we demonstrate a strain-accommodating smart skin (SASS) inspired by the structure of natural responsive PCs. The total volume of our SASS structure is maintained because the PC contraction is accommodated by local elastic deformation of a supporting polymer layer. SASS materials display excellent mechanical properties including high stretchability and good mechanical strength that is dependent, primarily, on the supporting layer. SASS demonstrates a

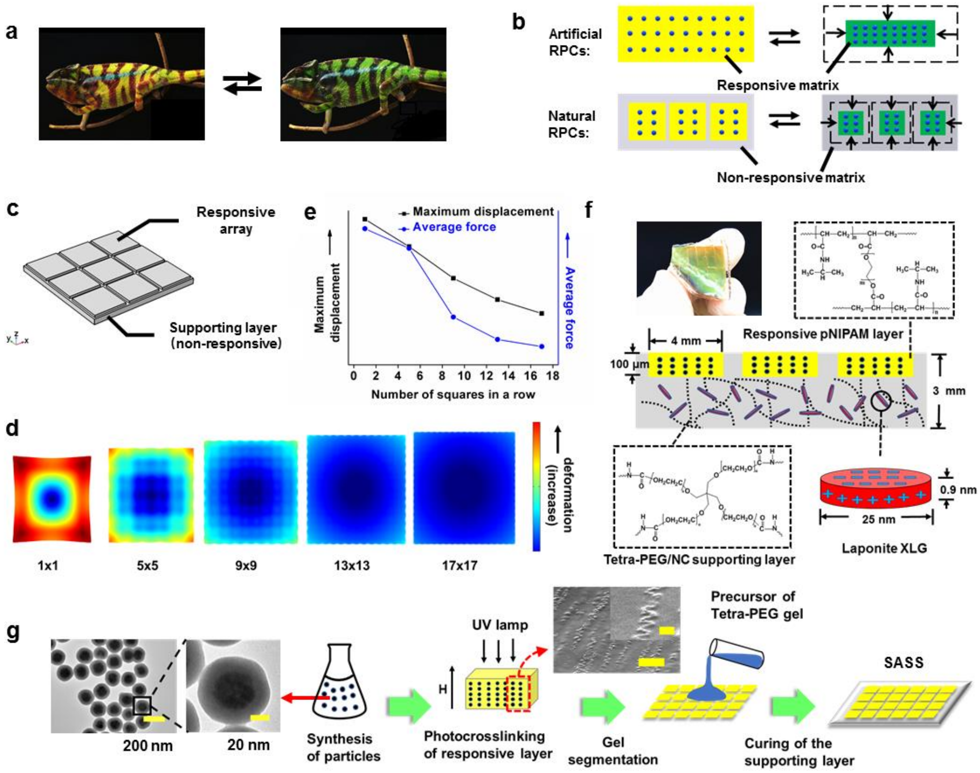

Figure 2.1. Design and fabrication of strain-accommodating smart skin (SASS) material. (a) Photographs of a chameleon displaying color change (Adapted with permission from Teyssier, J., Saenko, S. V., van der Marel, D. & Milinkovitch, M. C. Nat. Commun. 2015, 6, 6368. Copyright 2015 Springer Nature).1 (b) Schematic comparing the typical design of artificial responsive PCs to responsive PCs utilized by nature. The dots represent the PC, yellow and green represent the swollen and de-swollen states of the responsive hydrogel, respectively, and gray indicates the supporting, non-responsive polymer matrix. (c) Model used for finite element analysis (FEA) of SASS (also see Supplementary S2). (d) Rendering of FEA model mapping the deformation of a bilayer material with a supporting non-responsive layer and a responsive upper layer divided into sections. (e) Plot of the FEA determined average force and maximal displacement within a plane of the supporting polymer layer as a function of the number of squares in the responsive PC array layer. (f) Photograph and schematic of SASS that includes dimensions and chemical structure of polymers. (g) Flow diagram illustrating the steps used in SASS fabrication, where TEM and SEM images show representative structures of the magnetic nanoparticles and their organization with responsive PC (Scale bar of SEM image: 5 μm and 1μm (inset)).

generalizable concept of how to create responsive PCs that maintain constant size during chromatic shifting. Furthermore, we show that SASS color-change can be optically triggered and SASS films rapidly changed color upon exposure to ambient sunlight (t = 10 min). These features suggest the potential utility of SASS in applications such as camouflage and anti-counterfeiting.

2.2 Results and discussions

To recapitulate the strain-accommodating behavior of natural responsive PCs and predict the optimal material design, we first performed finite element analysis modeling of mechanical strain. Specifically, we modeled a patterned array of responsive PC hydrogels that were embedded within a non-responsive supporting polymer layer (**Figure 2.1c** and **2.1d**). The geometry of the model was such that the responsive PC elements were localized to the top face of the material. When we fixed the Young's modulus of the two materials and assumed a 50% change in length of the responsive layer, we found that a single planar layer of responsive hydrogel placed atop a supporting layer led to significant strain and deformation at the edges (**Figure 2.1d**, 1x1 case). Note that in our model, a free-standing responsive hydrogel film displayed the expected deformation. Importantly, when we segmented the responsive layer into arrays of squares, our modeling predicted a significant dampening of the deformation/strain that is associated with increasing number of segments (**Figure 2.1d**, 1x1, 5x5, 9x9, 13x13, and 17x17 cases). This reduction in deformation diminishes as *n* was increased from 13x13 to 17x17 as the SASS material showed minimal deformation with *n*=17. Plots of the Von-mises forces applied on a chosen plane of the supporting layer as a function of the number of square arrays predict a monotonic relationship, where the more finely patterned responsive polymer structure displayed the lowest displacement and average force (**Figure 2.1e**). Note that this conclusion holds as we vary the Young's modulus of the responsive and supporting layers and is not specific to the values shown in these representative modeling results. Therefore, our models predict that embedding finely segmented responsive PC layer within an elastic supporting layer will greatly diminish the global strain.

Guided by the computational results, we fabricated SASS as shown in **Figure 2.1f**. The responsive PC layer was comprised of monodisperse $Fe_3O_4@SiO_2$ particles (180 nm diameter, **Figure 2.2**), fabricated as previously described,[207] organized periodically using an external magnetic field, and confined within a photo-crosslinked poly(*N*-isopropylacrylamide) (pNIPAM) polymer. For optimal design of SASS, it is important to select a supporting polymer that is non-responsive while displaying robust mechanical elasticity. As a proof-of-concept, we employed tetra-polyethylene glycol (PEG) doped with a nanoclay (Laponite XLG) to create a robust hydrogel[208] as the supporting layer.

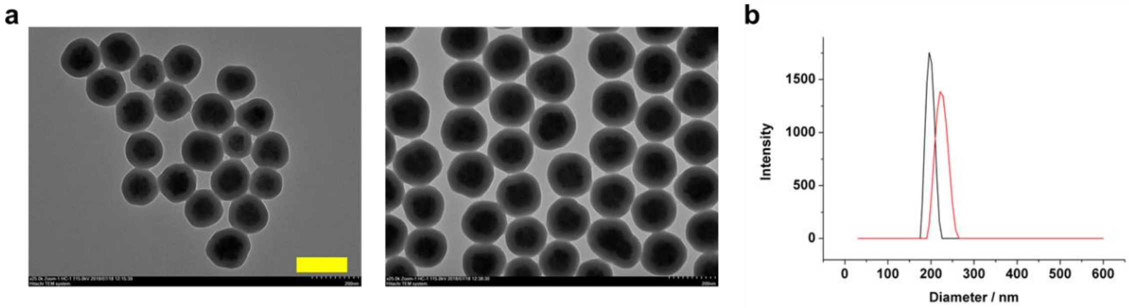

Figure 2.2 Size characterization of $Fe_3O_4@SiO_2$ particles. a) TEM images of 180 nm (left) and 210 nm (right) $Fe_3O_4@SiO_2$ nanoparticles. The diameters were determined by calculating the average diameter of over 100 particles in TEM images (scale bar 200 nm). b) Representative dynamic light scattering (DLS) spectra of two different sizes of particles. The average hydrodynamic diameter of the smaller particles was 196 ± 3.1 nm which is consistent with the TEM determine size of 180 nm. The large particles displayed diameter of 223 ± 4.7 nm and is consistent with the 210 nm diameter determined from TEM. Note that DLS results on average size of particles is greater than the TEM measurement due to the solvent layer surrounding the particles. The reported DLS diameters were averaged from five measurements.

SASS fabrication is detailed in **Figure 1g**. Briefly, $Fe_3O_4@SiO_2$ nanoparticles were mixed with the pNIPAM precursor solution (PEGDA crosslinker, riboflavin photoinitiator, NIPAM monomer), and while applying a magnetic field, UV light was used to crosslink the hydrogel, thus locking nanoparticles into defined periodic arrays. Subsequently, a mold (**Figure 2.3**) was used to create a square array of responsive PC hydrogels (4x4 mm squares, spaced by 0.5 mm). Finally, the tetra-PEG supporting layer precursor was cured onto the responsive PC array at room temperature. A photograph of a SASS film with a 5x5 responsive PC array demonstrating its color and elasticity is shown in **Figure 1f**. Cross-section scanning electron microscopy (SEM) imaging of the responsive PC layer confirms a periodic chain structure formed by magnetic nanoparticles (MNPs) (**Figure 1g**), which generates the colorful Bragg diffraction of the sample. Notably, the chain structures appear to be distorted in the SEM images likely due to drying-induced compression of the hydrogel matrix during imaging.

Figure 2.3 Photographs of Delrin® mold (left) and Delrin® gel cutting grids (right) used in this work.

To optimize the chromatic shift of the responsive pNIPAM PC layer, we tested the role of its mechanical properties (crosslinker concentration) in tuning the swelling/deswelling ratio (**Figure 2.4a**) and generating a maximal chromatic shift (**Figure 2.4b**). Optimization was performed using a reflection-mode spectrometer to record the chromatic shift of pNIPAM PC films in response to thermal heating (45 °C). We found that an intermediate concentration of crosslinker (120 mM polyethylene glycol diacrylate, PEGDA) produced the greatest magnitude of chromatic shift while minimizing area change. Additionally, optimization of magnetic field strength during synthesis is shown in **Figure 2.4c**. We found that if the magnetic field was too strong (385 Gauss), the peak wavelength shift was diminished likely because the periodic distance between particles approaches a minimum, and the collapse of the responsive hydrogel no longer can reduce inter-particle distance further. On the contrary, if the magnetic field is too weak (175 Gauss), no color is observed since the field strength is not sufficient to assemble photonic crystal. (**Figure 2.4c**). Therefore, we fixed our protocol to use 245 Gauss as it produced a maximum chromatic shift.

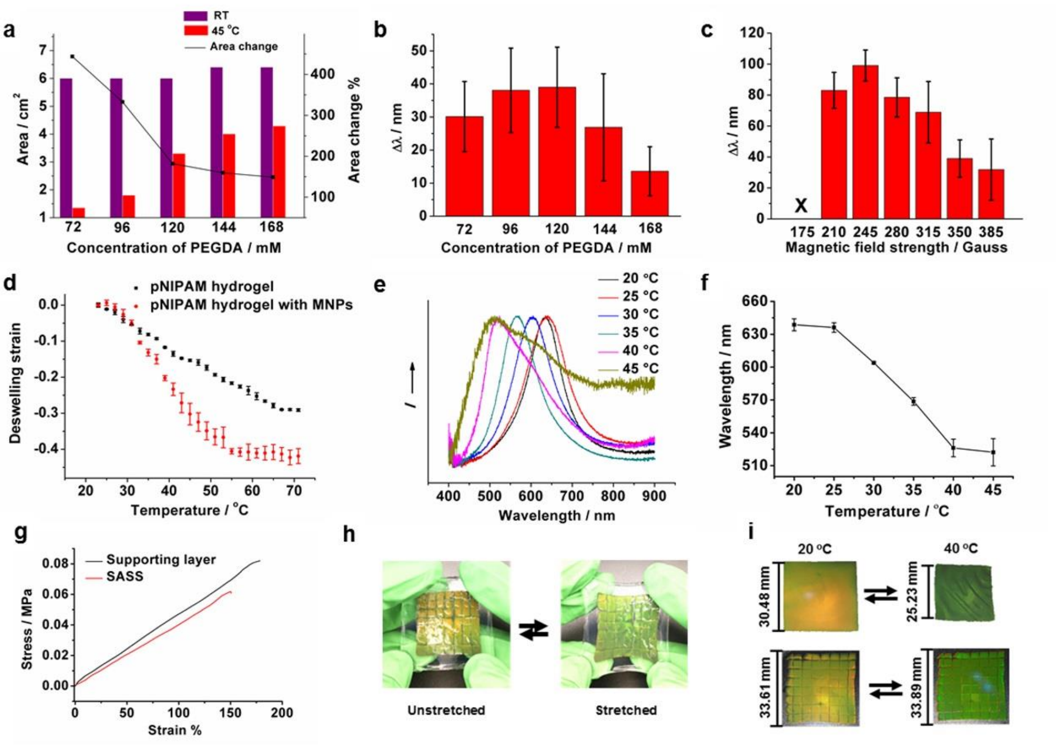

Figure 2.4. Characterization of SASS. (a) Plot relating the crosslinker (PEGDA) concentration in pNIPAM PC gels to their area before and after heating to 45 °C (a 350 Gauss magnetic field was applied during polymerization). The right y-axis represents the area change % upon heating for each composition. (b) Plot showing the change in reflection λ_{max} for the samples prepared in (a). The $\Delta\lambda_{max}$ was determined using reflection spectra of standalone PC films at RT and 45 °C. (c) Plot of reflection $\Delta\lambda_{max}$ (collected at RT and 45 °C) for responsive pNIPAM PCs polymerized under different magnetic field strengths. These gels were synthesized with 120 mM PEGDA. (d) Plot of temperature-dependent strain of pNIPAM hydrogels prepared without (black) and with magnetic nanoparticles (red). (e) Normalized reflection spectra of a SASS sample collected at different temperatures. (f) Plot showing λ_{max} of reflectance for SASS samples as a function of temperature. (g) Representative uniaxial tensile measurement of a SASS sample (red) and a sample of a standalone film comprised of the strain-accommodating polymer (black). (h) Photographs demonstrating the elasticity of SASS and its strain-induced color change. (i) Photographs showing the chromatic response of a traditional responsive pNIPAM PC film (upper) triggered by adjusting the temperature (20 °C to 40 °C) compared to the chromatic response of SASS (lower) under the same conditions. The dimensions of the materials in the initial and final states are provided to the left of each image. All error bars represent the standard deviation of three independent measurements.

These experiments provided the optimal parameters for fabricating the responsive PC hydrogel. Using these optimized conditions, we measured the thermally-induced volume transition of PC-containing and non-PC containing responsive films as shown in **Figure 2.4d** (120 mM PEGDA, 245 Gauss). PC-containing gels displayed a sharper and more significant thermally-induced deswelling strain compared to the pNIPAM films lacking the MNPs. This may be due to the strong UV absorption cross-section of MNPs which impacts UV-initiated radical polymerization. Note that the volumetric transition of these films is broader compared to that of conventional pNIPAM films, which is likely due to the PEG chains in the crosslinker (PEGDA) that modulates dehydration of the hydrogel (**Figure 2.4d**). The data in Figure 2.4a supports this conclusion since gels with higher PEGDA concentrations display lower deswelling ratios.

Representative reflection spectra and plots of the peak reflection wavelength *versus* temperature of the as-prepared SASS samples show a clear thermo-chromatic shift, in agreement with the reported behavior of responsive hydrogels (**Figure 2.4e and f**).[209, 210] The heat-triggered response of the SASS film was similar to that of the responsive PC films suggesting that the SASS architecture did not significantly modulate the transition temperature of pNIPAM. However, compared to the mechanical strength of conventional pNIPAM hydrogels,[211] which display rupture forces of a few kPa, SASS displayed superior mechanical strength. Specifically, uniaxial tensile testing (**Figure 2.4g**) showed that SASS has a rupture force of 60 kPa with a strain of 1.5. This was primarily driven by the mechanical properties of the supporting layer, which similarly had an 83 kPa rupture force with strain of 1.8. We also found that SASS samples could be handled manually and displayed a color change upon stretching (**Figure 2.4h**). Note that the chromatic shift generated by the $Fe_3O_4@SiO_2$ particle chains are sensitive to the orientation of the mechanical strain. Given that the thermal or optically triggered deswelling response generates in-plane forces, we focused on strains parallel to the SASS film. Of course, one can apply an external strain that is perpendicular to the SASS film, and such forces can lead to an opposite red-shift in the reflection peak of the material.

Critically, SASS displayed significant strain-accommodating behavior as was especially clear when comparing its volume transition to conventional responsive PC films (**Figure 2.4i**). To illustrate the difference, SASS and conventional responsive PC films were sandwiched between two plastic petri dishes such that only in-plane deformations were allowed. To the best of our ability to measure the dimensions of the SASS sample, its size was identical following heating-induced chromatic shifting, while the length of the conventional responsive PC film was reduced by ~23% after responding to the same heating source. **Figure 2.5** shows the deformation of free-standing SASS films with 1x1 and 8x8 segmentation. The 1x1 SASS film undergoes curling to form a tube-like structure due to the strain, in contrast to the 8x8 film that displays significant reduced strain.

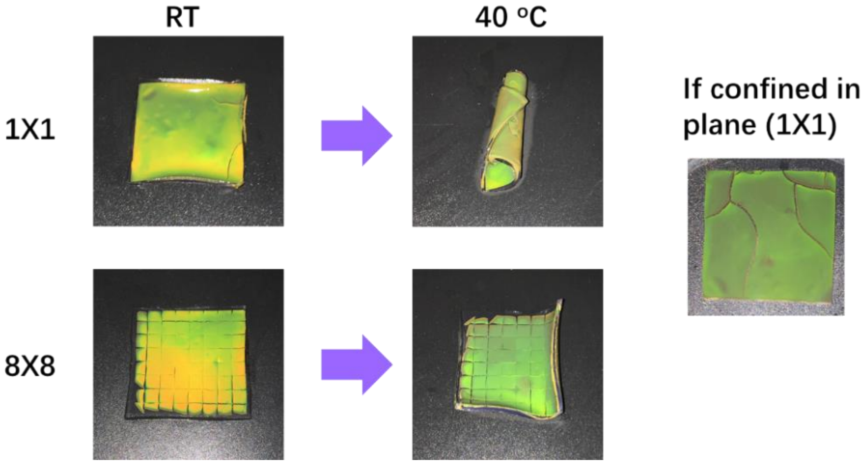

Figure 2.5 Photographs comparing deformation of SASS 1 x 1 and 8 x 8 films. The films were about 3.4 x 3.4 cm at room temperature. The samples were heated by using a water bath and were removed from the water in order to acquire the photographs.

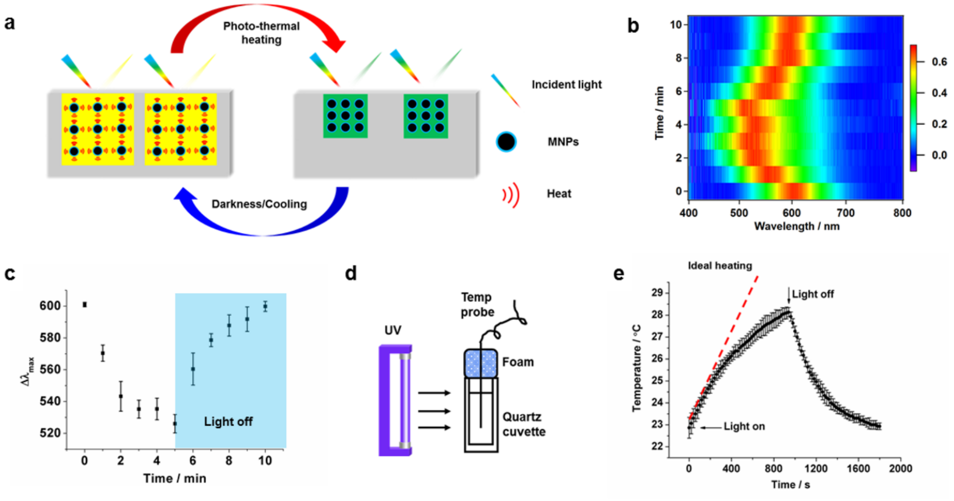

Figure 2.6. Light responsive behavior of SASS. (a) Schematic of the light responsive mechanism of SASS. Exposure to white light induces photothermal heating and a concomitant spectral shift in the peak absorbance as the spacing within the PC decreases. Cessation of light returns SASS to its original state. (b) 2-Dimensional color map depicting the spectral shift of SASS as a function of time when exposed to a white light LED source (light was on 0-5 min and off 5-10 min). (c) The reflection λ_{max} of illuminated SASS samples as described in b. The error bars represent the standard deviation of three measurements obtained from three different SASS samples. (d) Schematic of equipment set-up used for measuring the photo-thermal conversion efficiency. A UV light source was used to illuminate a dispersion of MNPs while the solution temperature was measured. (e) Plot of solution temperature during exposure of MNP dispersion to UV light as a function of time. The error bar represents the standard deviation from three independent samples. The red dashed line indicates the ideal heating of the dispersion and provides the heating rate of the sample.

In addition to its thermoresponsive properties, another intriguing feature of SASS is its light responsive behavior. Due to the strong light absorption of magnetite nanoparticles,[212] we hypothesized that illumination of SASS would also trigger a chromatic response (**Figure 2.6a**). Upon exposure of SASS to a handheld white light LED source, we observed a rapid and reversible reflectance peak shift that mirrored the response to thermal heating (**Figure 2.6b and c**). In the samples tested, we found that the reflection λ_{max} of SASS shifted from 600 nm to 525 nm within a few minutes of illumination. To further quantify the photo-thermal conversion efficiency of MNPs, a calibrated 370 nm light source with ~20 mW/cm^2 intensity was used to heat an aqueous dispersion of MNPs in a quartz cuvette (schematic shown in **Figure 2.6d**). As plotted in **Figure 2.6e**, the photo-thermal ideal heating rate can be inferred by extrapolating a tangential line to the initial phase of the heating curve. According to our calculation, we inferred a conversion efficiency of 81.8%.

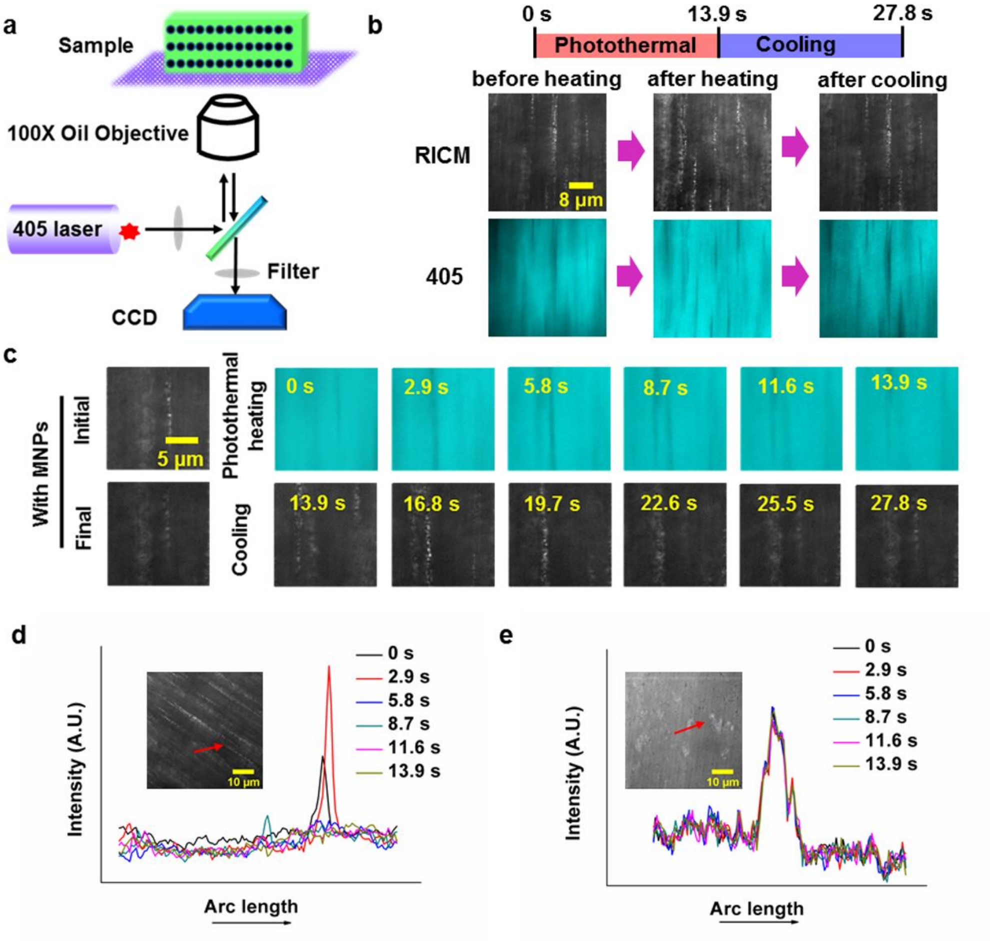

Figure 2.7. Microscopic *in-situ* observation of the light-induced SASS response. (a) Schematic of the microscope and sample set-up for *in-situ* observation of SASS. Irradiation with a 405 nm laser initiates photothermal heating, and remodels MNP organization. (b) Images of aligned MNPs in the responsive layer captured upon initiation of photothermal heating (0 s), at the end of heating (13.9 s), and at the end of cooling (27.8 s). (c) Time-lapse images of aligned MNPs in the responsive layer collected during photothermal heating with a 405 nm laser and cooling with the laser off. (d) and (e) show plots of line-scans for $Fe_3O_4@SiO_2$ nanoparticles (~3 nM), and SiO_2 nanoparticles (~3 nM) embedded within pNIPAM hydrogels during relaxation following 405 nm excitation for 13.9 s.

We next aimed to validate the dynamic remodeling of the PC arrays within the responsive hydrogel film upon illumination. To achieve this, we employed high-resolution *in-situ* optical microscopy to excite and simultaneously image the PC layer within the SASS film (**Figure 2.7a**). We found that exciting the sample using a 405 nm laser coupled with a quad cube filter set (405/488/561/647 nm) revealed the weak autofluorescence of the hydrogel. By happenstance, we found that continuous illumination in the 405 nm channel also triggered photo-thermal heating, localized deswelling of the SASS film, and reorganization of the PC microstructure (**Figure 2.7b**). Conveniently, the nanochain structure has significant scattering when imaged using a 535 nm reflection interference contrast microscopy (RICM) filter set. This allowed for concurrent imaging of the PC nanostructures along with the surrounding responsive hydrogel during photothermal heating and cooling (**Figure 2.7c**). As expected, the PC arrays (RICM channel) were anti-localized with the polymer hydrogel (405 nm channel). End points and Time lapse images recording a single photothermal heating/cooling cycle are shown in **Figure 2.7b and c**. In the time lapse images, the heating phase (0-13.9 s) was recorded using the 405 nm channel, while the cooling phase (13.9-27.8 s) was captured in the RICM channel. The PC chains are displaced and indeed go out of focus due to the isotropic (3D) nature of deswelling. Importantly, the images comparing the positions of the nanochain structure before and after the heating/cooling cycle demonstrate that the SASS microstructure recovers to its initial configuration.

To confirm that the photo-thermal effect was exclusively attributed to absorption by $Fe_3O_4@SiO_2$ particles rather than other components of SASS, we fabricated SASS films doped with pure silica particles lacking the Fe_3O_4 core (**Figure 2.7d**), and compared the time-dependent PC array displacement in SASS samples to that of films with silica nanoparticles (**Figure 2.7e**).

The lack of response in the silica nanoparticle-containing samples confirms the key role of magnetite in driving the light-triggered chromatic response of SASS.

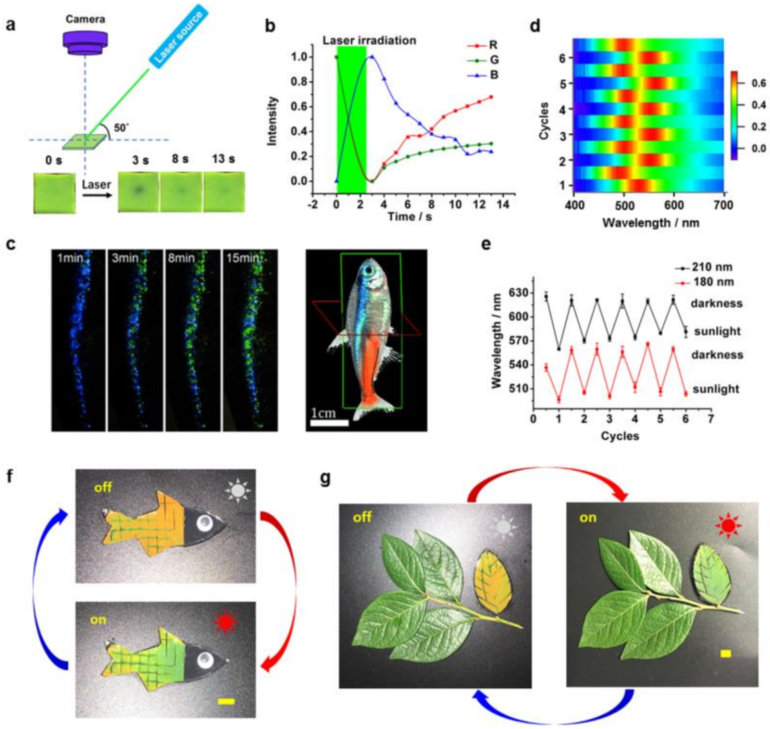

Figure 2.8. Potential light-triggered applications of SASS materials. (a) Experimental diagram of SASS optical stimulation along with smart phone camera readout. Lower inset: Photograph of a single 4 mm x 4 mm SASS tile before and after exposure to 532 nm laser. The SASS sample was fabricated using 180 nm diameter particles. (b) Red, green, and blue (RGB) colorimetric analysis of SASS response following a laser pulse. The green area indicates the period of laser irradiation. (c) Time lapse images of the lateral strip of a neon tetra fish after exposure to sunlight (Adapted with permission from Gur, D. *et al*., *Angew. Chem. Int. Ed.* 2015, *54*, 12426-12430. Copyright 2015 Wiley-VCH). (d) 2-Dimensional color map depicting the spectral shift during six sunlight triggered chromatic shift cycles. (e) Plot showing the chromatic shift of two SASS samples following multiple cycles of exposure to sunlight. The SASS samples were fabricated with two different sizes of MNPs. The maximum peak wavelength for each sample is plotted while oscillating between exposure to sunlight and darkness. (f) A fish-shaped SASS sample before (top) and after (bottom) exposure to sunlight for 10 min. (g) A camouflaged "leaf" fabricated with SASS and positioned alongside real leaves before (left) and after (right) sunlight exposure for 10 min (Scalebars: 1 cm).

SASS chromatic response could also be spatially controlled using localized illumination. To demonstrate this capability, a 532 nm laser was focused onto a 2 mm diameter spot on the SASS sample at an angle of 50˚ and a smart phone camera was used to record the chromatic change perpendicular to the sample (**Figure 2.8a**). The sample drastically changed color within a few seconds of laser illumination (**Figure 2.8a**), and the color change was localized to the spot of irradiation. The response was quantified by RGB analysis of the images (**Figure 2.8b**). An increase in blue intensity was observed with a concomitant decrease in both red and green intensity. This response is consistent with the expected blue shift in the reflection spectra after deswelling. This result suggests potential applications for SASS involving dynamic chromatic patterning.

Neon tetra fish are well known for their light-responsive behavior where the lateral stripes display different structural colors after brief exposure to sunlight (**Figure 2.8c**). To mimic this response, we first tested whether SASS is sensitive to natural sunlight. Surprisingly, we found that a 10 min exposure to sunlight triggered an observable chromatic shift (**Figure 2.8d**). Specifically, the SASS reflection λ_{max} shifted from 622±2.2 nm to 573±7.7 nm for samples fabricated with 210 nm diameter MNPs. The response triggered by sunlight was reversible, as the amplitude of the chromatic shift (48±9.6 nm) did not change significantly over the course of six illumination/cooling cycles. The range of the λ_{max} shift response could also be tuned by employing MNPs of a different diameter. For example, particles with a 180 nm diameter showed a reflection λ_{max} of 556±10.1 nm that reversibly shifts to 504±5.3 nm upon sunlight exposure (**Figure 2.8e**). Further mimicking the neon tetra fish response, we fabricated SASS films shaped like a fish (**Figure 2.8f**). After a 10 min exposure to natural sunlight, the SASS film shifted from orange to green, while the overall size remained constant as determined to the best of our abilities.

Given that SASS can be fabricated in different shapes and is sunlight responsive, we aimed to demonstrate camouflage behavior. Hence, we fabricated a leaf-shaped SASS sample and arranged it together alongside real leaves (**Figure 2.8g**). After exposure to sunlight, the color of the SASS “leaf” shifted from orange to green and was camouflaged among the real leaves. Again, a key feature enabling camouflage is that the size of the “leaf” remained constant during chromatic shifting.

2.3 Conclusions

In summary, we present an alternative approach to fabricate smart skin materials inspired by the chameleon skin structure. The SASS design solves the long-standing problem of mechanical buckling and instability of conventional responsive PC hydrogels. The key element to SASS is a two-component polymer material, where a segmented responsive PC hydrogel is embedded within a supporting polymer that accommodates the strain arising from the volume transition. By optimizing crosslinker concentration and magnetic field strength, we demonstrate a strong and reversible heat/light triggered optical response in SASS. High resolution optical microscopy confirms light-triggered local deswelling and chromatic response of the SASS film. Moreover, SASS chromatic response can be controlled in space and time using a focused laser beam. Note that the resolution of patterning is limited by the dimensions of the illumination spot, the rate of gel response, and the thermal diffusion coefficient within the sample. Future work will define these parameters. Finally, we show that SASS is sensitive to natural sunlight and can be molded into various geometries to aid in biomimicry. This suggests potential applications in camouflage, signaling, and anti-counterfeiting.

2.4Materials and methods

2.4.1 Synthesis of Fe_3O_4@SiO_2 core-shell nanoparticles (MNPs).

$Fe_3O_4@SiO_2$ core-shell nanoparticles were synthesized according to previously developed methods.[207] Briefly, for particles with an average diameter of 180 nm, 0.65 g $FeCl_3$, 40 mL ethylene glycol, 3.0 g sodium acetate, 1.05 g Poly(4-styrenesulfonic acid-co-maleic acid) sodium salt, 14 mg D-isoascorbic acid, and 120 µL deionized H_2O were added consecutively into a parafilm sealed beaker. After vigorous magnetic stirring for about 40 min, a homogeneous mixture formed and then 0.6 g NaOH was added. The mixture was stirred for 1-2 h until all the NaOH was completely dissolved. The mixture was then transferred into a capped 50 mL Erlenmeyer flask and then allowed to react in a preheated oven (190 ˚C) for 9 h. The particles were washed with 30 mL of 50% ethanol three times, and then washed three additional times with DI water.

To synthesize the silica shell, a 12 mL aliquot of Fe_3O_4 dispersion was mixed with 80 mL ethanol and 4 mL ammonium hydroxide (25-28 wt%) under vigorous mechanical stirring for 1 min. This solution was warmed by using a water bath at 50 ˚C. Subsequently, two aliquots of 0.4 mL TEOS were added every 20 min. Finally, the reaction products were washed with ethanol three times by using magnetic separation for each wash.

2.4.2 Synthesis of pure silica nanoparticles.

Silica nanoparticles (~300 nm) were synthesized by the well-established stöber method.[213] 50 mL ammonium solution was made by mixing 9 mL ammonium hydroxide (25-28 wt%), 16 mL ethanol, and 25 mL deionized H_2O. This solution was swiftly added to 50 mL of 0.4 M TEOS ethanol solution under vigorous stirring. After reacting for 2h, the particles were centrifuged and washed three times with ethanol to collect monodisperse silica nanoparticles. TEM indicated that the average particle size was approximately 300 nm.

2.4.3 Fabrication of Delrin® mold and gel cutting tools.

Square shaped sheets of Delrin® with a thickness of 0.125 inches (0.3175 cm) were cut into the desired shapes using a laser cutter (Universal Laser Systems VLS 4.60, featuring a 60-watt CO_2 laser). The patterns were designed using the AutoCAD software package.

2.4.4 Synthesis of responsive photonic film.

The as-obtained Fe_3O_4@SiO_2 particles from the protocol (described above) were redispersed in 12 mL of ethanol, and then 3 mL of this solution of Fe_3O_4@SiO_2 was redispersed in EG solution containing 8 mg riboflavin, followed by adding 0.09 g Irgacure, 225 μL poly(ethylene glycol) diacrylate, and 0.45 g N-isopropylacrylamide. The mixture was vortexed for 10 s to obtain a homogeneous solution that was then sonicated for 5 min in the dark. We describe this mixture as the "precursor solution" in subsequent steps. A 3 cm × 3 cm Delrin mold covered with a piece of transparent petri dish was used to fabricate the responsive photonic crystal layer. For each synthesis, 350 μL precursor solution was injected into the mold and exposed to a magnetic field of approximately 245 Gauss (determined using a WT10A teslameter). Finally, the precursor solution was cured with a 100 W high intensity UV lamp (365 nm, Analytik Jena US company) for 10 min. The as-obtained thin film was washed with DMF and H_2O three times, respectively, then was stored in water for further use. Notably, for special shapes (fish and leaf), the Delrin® molds were deliberately fabricated into the required shapes by using a laser cutter as described above using AutoCAD to draw the design.

2.4.5 Patterning of SASS.

The as-synthesized responsive photonic film was first cut by firmly pressing a patterned Delrin® grid. This was performed on a clean petri dish surface. Prior to the fabrication of the PEG supporting layer, two precursor solutions were prepared. The first (precursor A) was generated using 750 μL deionized water and 0.03 g Laponite XLG that were mixed together in a 2 mL vial using a magnetic stir bar until the solution became clear. To this Laponite XLG solution, 750 μL of 0.1 M $Na_4P_2O_7/H_3PO_4$ buffer (pH=7.2) and 0.12 g tetra-PEG-NH_2 were added and completely dissolved through vigorous stirring and sonication. The second precursor solution (B) was prepared using 0.12 g tetra-PEG-NHS that was dissolved in 600 μL $Na_4P_2O_7/H_3PO_4$ buffer (pH=7.2) under vigorous stirring and sonication. Both precursors A and B were stored in an ice box for 20 min before mixing in order to slow the gelation rate. After cooling precursors A and B, the solutions were mixed together for 10 s using a magnetic stir bar, then quickly poured into a specific Delrin® mold (**Figure 2.3**) and sandwiched with the grid-cut photonic film that was placed on a petri dish. The gelation process was complete within 15 min at room temperature.

2.4.6 Characterization.

TEM images were acquired with a Hitachi HT-7700 with 80 kV accelerating voltage. SEM images were obtained using a Topcon DS-130F Field Emission SEM. Digital photographs and videos were recorded with an iPhone 6s. Dynamic surface temperature was monitored by an Etekcity Lasergrip 1080 Non-Contact Digital Laser Infrared Thermometer Temperature Gun (dynamic range for instrument is -50 ˚C to 550 ˚C). Dynamic light scattering (DLS) was performed with a NanoPlus Zeta / Nano Particle Analyzer at 25 °C. UV light intensity was determined by AMTAST UVA365 UV light meter. Gel deswelling ratio was measured by a digital caliper. White LED illumination was performed using a Cygolite Metro 800 with light intensity of 800 lumen (distance to the sample: 3 cm). Solar responses were tested with natural sunlight during the daytime between the hours of 1 pm to 3 pm during the months of June and July (location: 33°47'29.6"N 84°19'36.3"W). Laser response test was conducted with a 50-80 mW 532 nm Green Laser Module with TTL and Fan (12V) purchased from OdicForce Lasers (Surbiton, UK). Reflectivity spectra were measured with a FLAME-S-VIS-NIR Spectrometer equipped with a premium 400 µm reflection probe (Ocean optics Inc., Dunedin, FL). All the spectra data were recorded through the OceanView 1.6.3 software package. Uniaxial tensile tests were conducted using a TestResources 100Q Universal Testing Machine (Shakopee, MN). All optical imaging was performed using a Nikon Eclipse *Ti* microscope, operated with Nikon Elements software, a 1.49 NA CFI Apo 100x objective, perfect focus system, LED light source along with a laser launch excitation source. ImageJ was used to analyze the intensity change of the time lapse video.

CHAPTER 3. SUPRAMOLECULAR DNA PHOTONIC HYDROGEL FOR ON-DEMAND CONTROL OF COLORATION

3.1 Introduction

Photonic crystals (PCs) are periodic arrays of nano- and micro-scale materials that can display striking colors due to Bragg diffraction[214-217]. In contrast to dyes and pigments which absorb specific wavelengths of light, PCs are resistant to photobleaching and their color is dependent on the spatial periodicity of the material rather than its chemical composition. Indeed, as predicted by Bragg's law of diffraction, the specific coloration of PCs can be tuned by adjusting the spacing in the periodic array[218-220].

The ability to create responsive PC materials that can generate coloration in space and time is highly desirable as such materials have important applications in sensing[215, 218, 220], camouflage[128, 221], and anti-counterfeiting inscriptions[222, 223]. Most responsive PC materials are generated by embedding or etching PC structures in a hydrogel matrix that displays a volume change (ie. swelling or collapse) in response to specific types of input[224-226]. These changes in the matrix will in turn modulate the lattice constant of the PC and hence tune the color of the material. One of the greatest challenges in this area is on-demand patterning of the nanoparticle re-organization, as the PC nanoparticles are physically confined within the matrix of the hydrogel. In other words, the challenge pertains to creating periodic assemblies of nanoparticles within a hydrogel from a disordered array with spatial and temporal control. Herein, we address this challenge and create a PC hydrogel that displays on-demand coloration by using DNA supramolecular hydrogels that can rapidly and locally switch between crosslinked and de-crosslinked states using an opto-thermal trigger.

To achieve on demand assembly with high spatial and temporal resolution two conditions must be met: 1) A hydrogel must undergo local, reversible, and transient de-crosslinking upon specific inputs, and 2) Nanoparticles should rapidly translocate and organize within the hydrogel during transient de-crosslinking. To the best of our knowledge, there are no reported examples of nanocomposite hydrogels that meet these conditions. The most commonly adopted approach to form PC hydrogels requires first organizing the PC material using an external magnetic, gravitational, or electric field. Once organized, the hydrogel is crosslinked in a way that the nanoscale periodicity is locked and preserved after the removal of external field.[128, 216, 225, 227] This is due to the large energy barrier to diffusion created by the hydrogel network which prevents nanoparticle mobility inside the hydrogel.

Our approach is illustrated in **Figure 3.1** where we used a DNA supramolecular hydrogel[228] constructed from palindromic single stranded DNA (ssDNA) with three self-complementary domains (red, green, and blue domains in **Figure 3.1a**). To create the PC, we used superparamagnetic magnetite nanoparticles (MNPs) coated with poly(ethylene glycol) (PEG) that assemble into periodic structures under an external magnetic field (**Figure 3.1b)**. PEGylated MNPs are stable enough to assemble in aqueous buffers with higher ionic strength which is necessary for DNA hydrogel formation. Given that crosslinks are exclusively created using hybridized DNA strands, denaturing the DNA allows complete de-crosslinking of the hydrogel and thus lifting the energy barrier for particle mobility (**Figure 3.1c)**. In contrast to other supramolecular hydrogels, pure DNA-based hydrogels in this work display faster gelation kinetics with time resolution of seconds and a relative rigid network that can hold the in-situ assembled structure. These two features are advantageous for on demand structural coloration and de-coloration.

The key design criteria for creating an on-demand PC material are illustrated using a simplified energy diagram in **Figure 3.1c**, where the y-axis represents the free energy of the system and the x-axis represents an order parameter (e.g. the particle organization). State 1 illustrates an initial condition where particles are randomly distributed inside the hydrogel network, while state 2 represents ordered particles that form the PC. Under the influence of an external magnetic field (B), state 1 is higher in energy compared to state 2 due to the potential energy of the magnetic dipole moments of the MNPs. In order for the particles to organize, they must overcome the energy barrier required for movement across the DNA hydrogel network. This barrier is large when the DNA is fully hybridized (black curve **Figure 3.1c**) and hence particles are locked in place. When the DNA is denatured, the barrier reaching state 2 is lowered and thus allowing for translocation to occur (red curve, **Figure 3.1c**). **Figure 3.1d** illustrates the overall cycle of triggered on-demand assembly (patterning) and disassembly (erasing) of the PC within the DNA hydrogel. In our case, we trigger DNA disassembly using the broad absorption spectrum and high photothermal conversion efficiency of MNPs. This can locally and transiently melt the DNA network and dramatically lower the particle translocation energy barrier. The simulation of photo-thermal effect of the laser on the hydrogel is illustrated in **Figure 3.2**, which proves the heat generated by MNPs are large enough to dehybridize the surrounding DNA duplex networks. Upon illumination, the MNPs should generate heat and locally melt the gel as they translocate and align with an external magnetic field, therefore forming a periodic PC structure. Upon removal of illumination, rapid heat dissipation should result in re-hybridization of DNA strands. This locks the patterned PC in the DNA gel. Notably, these PC patterns can be rapidly "erased" by illumination in the absence of an external magnetic field.

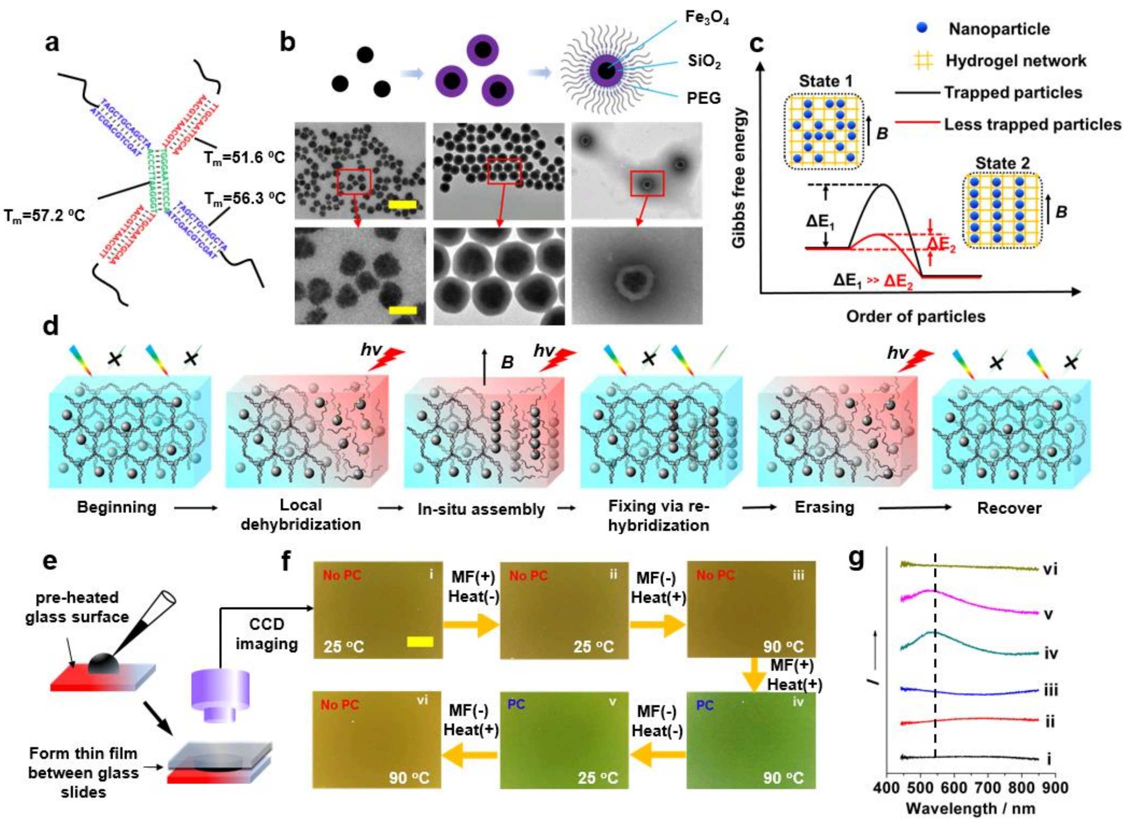

Figure 3.1. Design and testing of the DNA hydrogel system for on demand patterning and erasing. a) Design of a purely DNA supramolecular hydrogel system in which the DNA hydrogel is formed from three different palindromic sequence domains located on a single strand. b) Schematic of MNP synthesis and corresponding TEM images of real samples. Magnetite nanoparticles (~120 nm) are coated with a silica shell (~30 nm) first and then a layer of PEG. (scale bar: 500 nm for upper set and 125 nm for lower set) c) Theoretical energy diagram of in-situ assembly of the hydrogel. d) Mechanism of in-situ assembly which the local and transient dehybridization of DNA hydrogel would lower the energy barrier for particle assembly under a magnetic field and then re-gelate to fix the pattern. This can be erased at a later time by de-hybridization in the absence of a magnetic field. e) Schematic of sample preparation and imaging. f) Digital photographs (state i-vi) of the same hydrogel sample at different conditions showing color changes, scale bar 600 μm. g) Reflectance spectra that correspond to the photographs in f), displaying the emerging reflectance peak ~530 nm after the in-situ assembly, which corresponds to the Bragg diffraction of in-situ assembled PC.

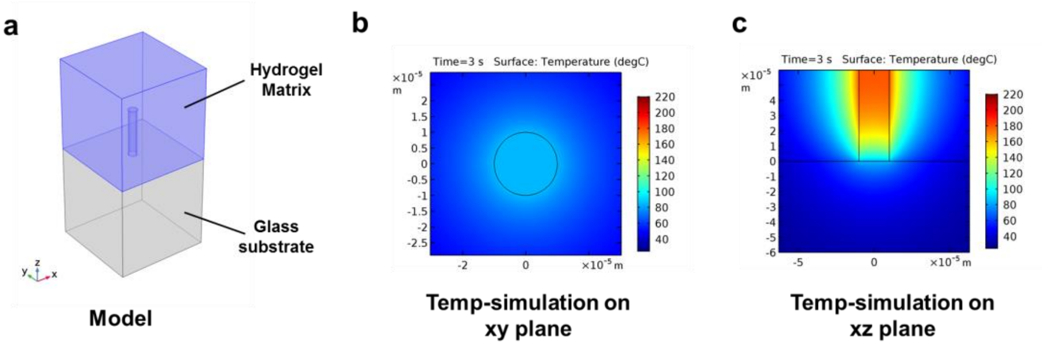

Figure 3.2 Finite element simulation of photothermal heating using a 36.2 mW laser focused on a hydrogel. This simulation uses the model “heat transfer in solid” in COMSOL Multiphysics. a) Basic model of the simulation, in which the cylinder in the middle represents the path of the laser beam (radius=10 μm) and the blue box represents a limited area of hydrogel matrix while the grey box represents a limited area of glass substrate. The cylinder geometry (laser beam pathway) is treated as the heating source which has a power of 36.2 mW. b) A xy-plane cross-section that maps the temperature distribution after 3 s of thermal energy generation. The units of the calibration bar is ^oC. c) A xz-plane cross-section that maps the temperature distribution. The modeling indicates that the temperature increase produced by the photo-thermal effect exceeds the melting temperature of the DNA duplex (~60 ^oC).

3.2 Results and discussions

As a proof-of-concept, we tested our design using bulk heating to drive the DNA denaturation. After mixing the MNP solution with the palindromic ssDNA, we heated the sample to 90 ^oC in potassium phosphate buffer (37 mM, pH = 7) to form a homogeneous solution. The solution was cast on a preheated glass surface and then sandwiched using a second glass slide (**Figure 3.1e**). A thin film of the mixture was then allowed to cool to room temperature, thus forming a hydrogel (**Figure 3.1f**). The formed gel displayed a brown color, and its reflection spectra lacked any clear features (state i in **Figure 3.1f** and **3.1g**).

Neither the physical appearance of the material nor its reflection spectra changed when a magnetic field (~200 Gauss) was applied to the gel (state ii in **Figure 3.1f** and **g**). Likewise no change was observed when the gel was only heated (90 ^oC) (state iii in **Figure 3.1f** and **g**). However, when the gel was heated (90 ^oC) while simultaneously applying a magnetic field (~200 Gauss), green coloration appeared that was consistent with the appearance of a reflection band λ = 530 nm, thus confirming formation of the PC (state iv in **Figure 3.1f** and **3.1g**). The PC was maintained even after cooling the sample to room temperature (state v in **Figure 3.1f** and **3.1g**). Notably, heating the sample without applying an external magnetic field disrupted the structural color and allowed the material to return to its original non-PC (brown color) state (state vi in **Figure 3.1f** and **g**). These results support the model described in **Figure 3.1d** and suggest the feasibility of reversible patterning of the PC with a photothermal input.

To better understand the gelation behavior of the DNA photonic hydrogel, we next performed rheology measurements as a function of DNA sequence, gelation time, and temperature. Firstly, three different sequences were designed and used to create DNA/nanoparticle composite hydrogels. Each sequence contained three palindromic domains of increasing length, 12, 16, and 20 oligomers (**Fig. 3.3a-c**). **Figure 3.3a-c** shows that gelation was reversible within just a single cooling (purple) and heating (red) cycle. At elevated temperatures, all samples were in a low-viscosity liquid state as G' was similar to G'' and their values were fairly low. As the temperature dropped, DNA hybridization proceeds, and this leads to gelation of the material as indicated with a drastic increase in G' and G'' and G'>G''. The apparent peak in G' and G'' is likely due to the volume change in the hydrogel due to hybridization[229]. We have also synthesized two additional sizes of MNPs to test the influence of particle size on the rheology of the hydrogel. However, we did not find a significant difference in rheology for DNA hydrogels embedded with 140, 180, and 200 nm diameter MNPs.

To investigate the effect of DNA sequence on gelation kinetics, we performed time-dependent rheology measurements. In principle, longer sequences should display slower hybridization kinetics and hence longer gelation times. Surprisingly, rheology measurements showed nearly identical gelation kinetics for the three sequences (**Figure 3.3d-f**). This is likely because the gelation time of the DNA is rapid and proceeds at time scales exceeding the time resolution of the rheometer (~0.083 °C/s). Thus, this indicate the palindromic DNA gelation kinetics are fast, which is advantageous to achieve our goal of on-demand formation of PC structure *vide infra*.

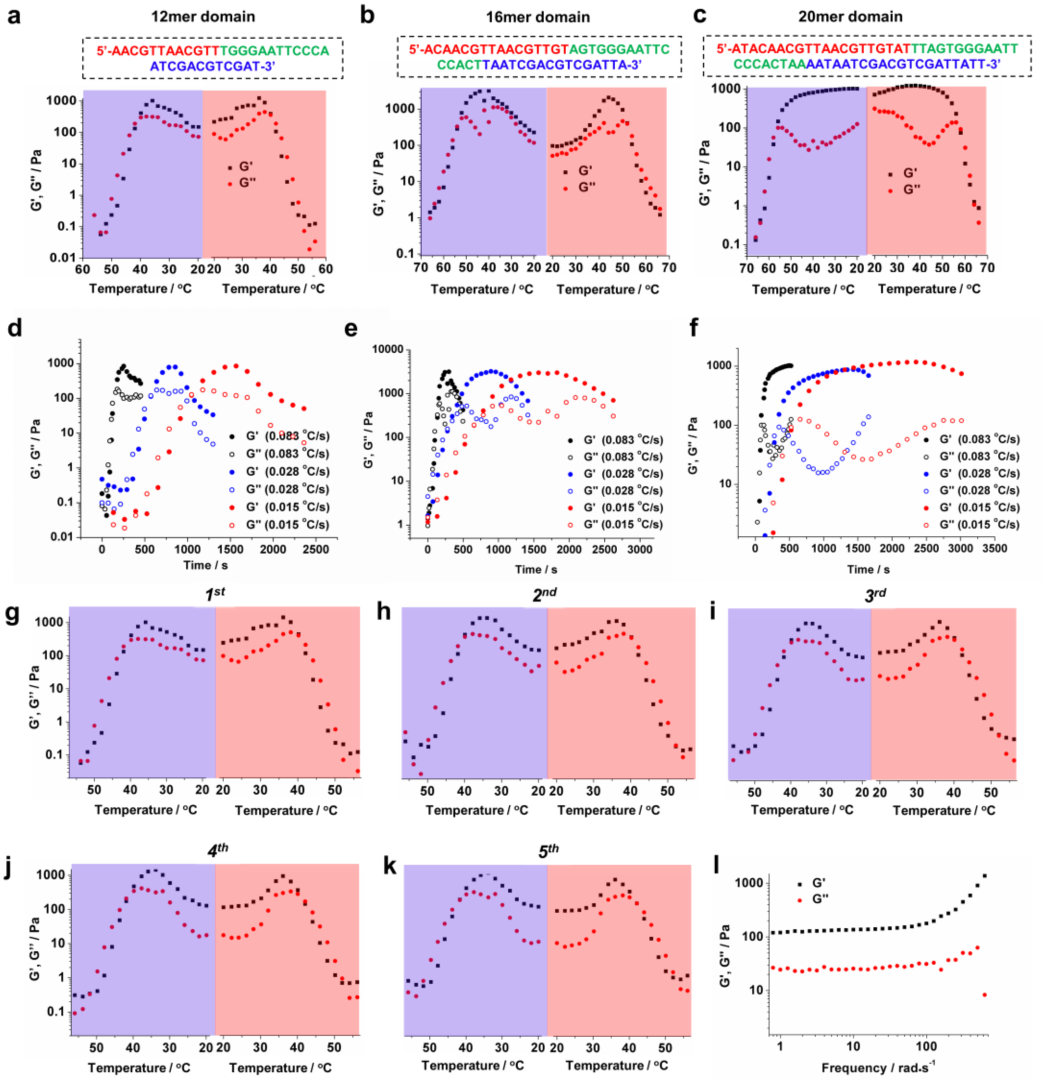

Figure 3.3. Rheology characterization of DNA supramolecular hydrogel/MNP composites. a-c) Rheology plots during cooling-heating cycles of PC hydrogels. The DNA supramolecular hydrogel is designed with three different sequences with palindromic domain lengths of 12,16, and 20 bases corresponding to a), b), and c), respectively. d-f) Rheology results using different scan rates (0.083, 0.028, and 0.015 °C/s) for different PC hydrogels shown in a-c). g-k) The cooling-heating cycles of PC hydrogels formation from 12mer palindromic domain DNA sequence. l) A frequency scan at room temperature of PC hydrogel formation with 12mer domain DNA strands to test the integrity of the hydrogel (G'>G'').

In order to test the reversible gelation behavior, we additionally performed rheology measurements while running multiple thermal cycles on the DNA composite hydrogel formed by the 12-mer domain (**Figure 3.3g-k**). We found that the gelation behavior does not significantly change even after 5 heating-cooling cycles and the sample showed classic hydrogel behavior (G’>G’’) at room temperature following thermal cycling. These results confirm the possibility of generating erasable PC patterns by repeated thermal cycling of the DNA hydrogels.

Figure 3.3l shows a plot of the G’ and G’’ as a function of frequency at room temperature. The data confirms that G’> G’’ across the tested frequencies showing classic hydrogel behavior. We were unable to plot G’ and G’’ above the transition temperature, as the gel was completely liquid and displayed the minimum G’ and G’’ reportable values of ~0.02 Pa which is the limit of the rheometer resolution. These palindromic DNA hydrogels are rheologically distinct from hybrid gels comprised of acrylamide polymers crosslinked using DNA. The rheology measurements for the acrylamide-DNA gels showed a relatively high G’ above the transition temperature, which is likely due to the entanglement of its long polymer backbone (**Figure 3.4**). Therefore, acrylamide-DNA gels would still significantly hinder the reorganization of MNPs above the transition temperature so that on-demand assembly of PC would fail (**Figure 3.5**). Hence, this particular 3-domain palindromic DNA offers properties that are advantageous for the goal of on-demand assembly of PC structures.

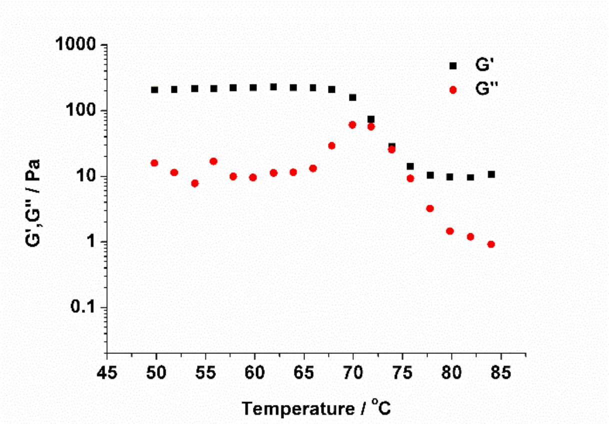

Figure 3.4. Temperature-dependent rheology experiments with dsDNA crosslinked polyacrylamide hydrogels. The hydrogel (4 wt%) was mixed with MNPs at ~90 ºC with a volume ratio of 1:1. The protocol for preparation of the sample was similar to that used for pure DNA based PC hydrogels introduced in the main text.

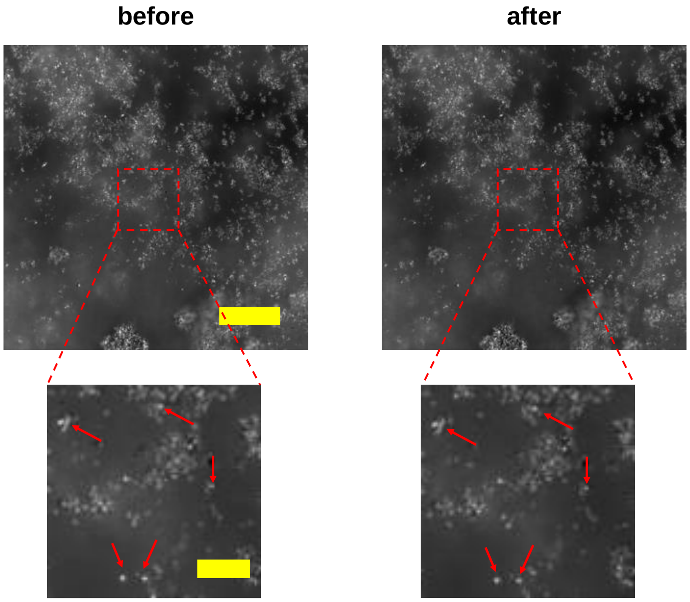

Figure 3.5. In situ microscopic imaging of polyacrylamide hydrogels that were crosslinked using DNA duplexes. These types of gels are commonly used in the literature, hence motivating this experiment. We found that these types of gels created barriers to the mobility of the MNPs even when the gel was heated using NIR illumination. We believe that this is because of polyacrylamide chain entanglement that hinder particle mobility. Thus, the all-DNA hydrogels discussed in our work are essential for on demand coloration. The conditions used for this experiment are identical to those used for the pure DNA supramolecular hydrogel shown in **Figure 3.6**. The microscopic results show nearly identical images before/after the sample was irradiated with 785 nm laser while applying a magnetic field. Note that the laser illumination was held for 3 sec while also applying a magnetic field of 100 Gauss at the same time. (Scale bar: 20 µm (upper set); 5 µm (lower set))

To provide further evidence of light and magnetic field driven assembly of the MNPs into a PC structure within the DNA hydrogel, we employed high-resolution optical microscopy to observe the microscopic assembly of the particles. In our microscope setup, we observed the MNPs by using reflection interference contrast microscopy (RICM) at λ_{ex} = 535 nm while simultaneously exciting the region of interest using a galvo-controlled ~5 μm diameter 785 nm laser irradiation system (**Figure 3.6a**). We used a rare earth magnet to generate a magnetic field (~100 Gauss) that drives the assembly of MNPs in a direction that is parallel to the magnetic field and the observation plane. **Figure 3.6b** shows RICM images displaying the organization of the MNPs prior to and after near-IR illumination (785 nm) for 10 sec (red circle; duty cycle 50%; power = 36.2 mW; on-time = 500 msec). We note the formation of linear assemblies of particles that align with the external magnetic field. To demonstrate the reversibility of PC assembly, we next illuminated the same region for another 10 sec (red circle; duty cycle 50%; power =36.2 mW; on-time = 500 msec) in the absence of the magnetic field. The bottom two images in **Figure 3.6b** show the loss of particle organization in the absence of the external magnetic field. Importantly, particle assembly was confined to the near-IR illumination area while the remaining regions showed static particles that remained randomly distributed. Similar results were also found in DNA hydrogels with the 140 and 200 nm diameter MNPs. We also performed z-stack scanning in the RICM channel and generated 3D reconstruction images (in ImageJ) to further identify the linear assemblies of MNPs inside the gel after alignment where the MNPs assemblies are erased (**Figure 3.6c**). Quantitative analyses of alignment were conducted using the ridge detection plugin[230] of ImageJ, which allowed us to measure an in-plane Feret angle for the linear assemblies using the microscope image frame of reference where $\theta=0°$, which is parallel to the *x*-axis and serves as the frame of reference. **Figure 3.6d** and **e** show radial histograms and box plots, respectively, that were collected from three regions of interest after alignment and erasing of the linear assemblies as described above. In **figure 3.6d**, the fan area indicates the angle distribution. The largest area from Feret angle of the aligned MNPs was the area that represents 0-30^o, coinciding with the approximate direction of the magnetic field (as illustrated in **Figure 3.6b**). After erasing, the angle preference was lost since other fan areas grow nearly as large as the one that represents 0-30^o. In box plots (**Figure 3.6e**), the data points of the original sample showed a uniform distribution span from 0 to 180^o. However, most of the data points converge to ~30^o after alignment, which indicates an angle of interest that is similar to **Figure 3.6d**. This alignment is lost again in the box plot that represent the erased sample. To summarize, the laser and magnetic field induced on-demand patterning is effective and swift as expected.

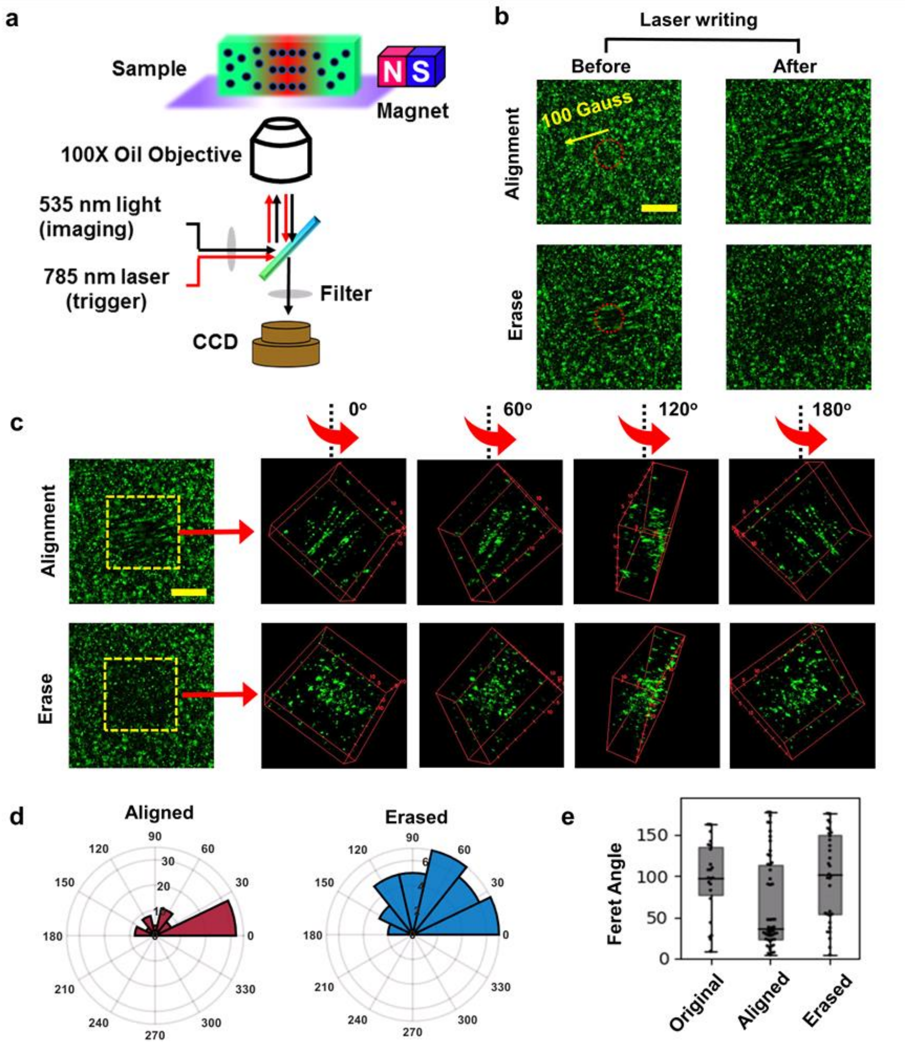

Figure 3.6. Microscopic imaging results of on-demand assembly. a) Schematic of microscope settings for in-situ imaging. The sample was on a glass slide and observed by 100X oil objective with an optical path to a CCD camera and 785 nm laser controlled by a galvo-mirror system for spatially selective excitation. b) Comparison of nano-pattern changes inside the hydrogel before and after applying laser irradiation. Upper set: laser writing of PC nano-patterns. Lower set: laser erasing of PC nano-patterns. (Scale bar: 20 µm) c) 3D reconstructed images based on z-scans of the sample at different angles of rotation demonstrating organized or disorganized structures inside the hydrogel. (Scale bar: 20 µm) d) Feret angles plotted in histogram based on statistical analysis of aligned or erased structures that correspond to automated object detection ridge analysis of sample images. e) Box plot shows the statistical analysis of Feret angles measured from original, aligned or erased samples

On-demand and in-situ assembly of PC structure in hydrogels has many potential applications. One of these applications is for on-demand writing/erasing which was described recently[231-233]. To demonstrate this potential application using our approach, we conducted a series of writing/erasing tests in the DNA hydrogel samples. As described above, photo-thermal heating can trigger local melting of the DNA, thus minimizing the energy barrier of MNP translocation and allowing for on-demand assembly. Our first goal was to quantify how the irradiation time and power tune the local assembly and coloration of the PC gel. Hence we designed an array of irradiation spots with different laser powers (40%–100%) and irradiation times (1–5 sec), and captured images of the gel before and after illumination (**Figure 3.7a**). The experiment was conducted under an external magnetic field that was perpendicular to the observation plane. We found that the color of the PC gel did not change when the total input energy was low; either when the illumination time was brief or if the illumination intensity was weak (e.g. 40% laser power, 1s irradiation time). At greater illumination intensities and dwell times, we observed the diameter of the spots increased as a function of the energy input (**Figure 3.7b**). This is likely due to the accumulation of heat allowing for melting of greater regions of DNA and migration of greater numbers of MNPs from the surrounding hydrogel. We also observed formation of spots that seemed to have a colored ring and dark center. According to our investigation, the dark center is likely due to the depletion of DNA because the hydrogel unevenly re-distributed after heating/cooling (**Figure 3.8**). This is supported by control experiments using fluorophore labeled ssDNA (**Figure 3.9**). We found that a laser power of 80% with 3 s irradiation time produced optimal results since the spot size produced sufficient contrast from the background and the spot size was smaller suggesting improvement in spatial resolution. We also find that the spot size is related to particle concentration. The melting area changed drastically when we photothermally heated the hydrogel sample. This is due to the higher particle concentration for the samples with greater weight percentage which produces greater amounts of heat upon illumination **(Figure 3.10).** By applying this protocol using patterns with pre-assigned (x,y) coordinates, we first created a 3-leaf clover-like figure with an area of 1-2 mm^2 which was spatially patterned and erased after bulk heating and cooling (**Figure 3.7c**). We also demonstrated the patterning of a QR code (2 mm x 2 mm) encrypting with text information of "Emory 1836" in **Figure 3.7d**. Information can be stored and later read using a smart phone as we showed in this figure. In our system, this pattern comprised of ~250 spots required approximately 10 min to complete with a single laser illumination system, thus demonstrating the ability to create patterns on-demand. Compared to rewritable technology based on photochromic materials[233, 234], our method is free of photobleaching, does not require a photomask, and generates patterns more rapidly.

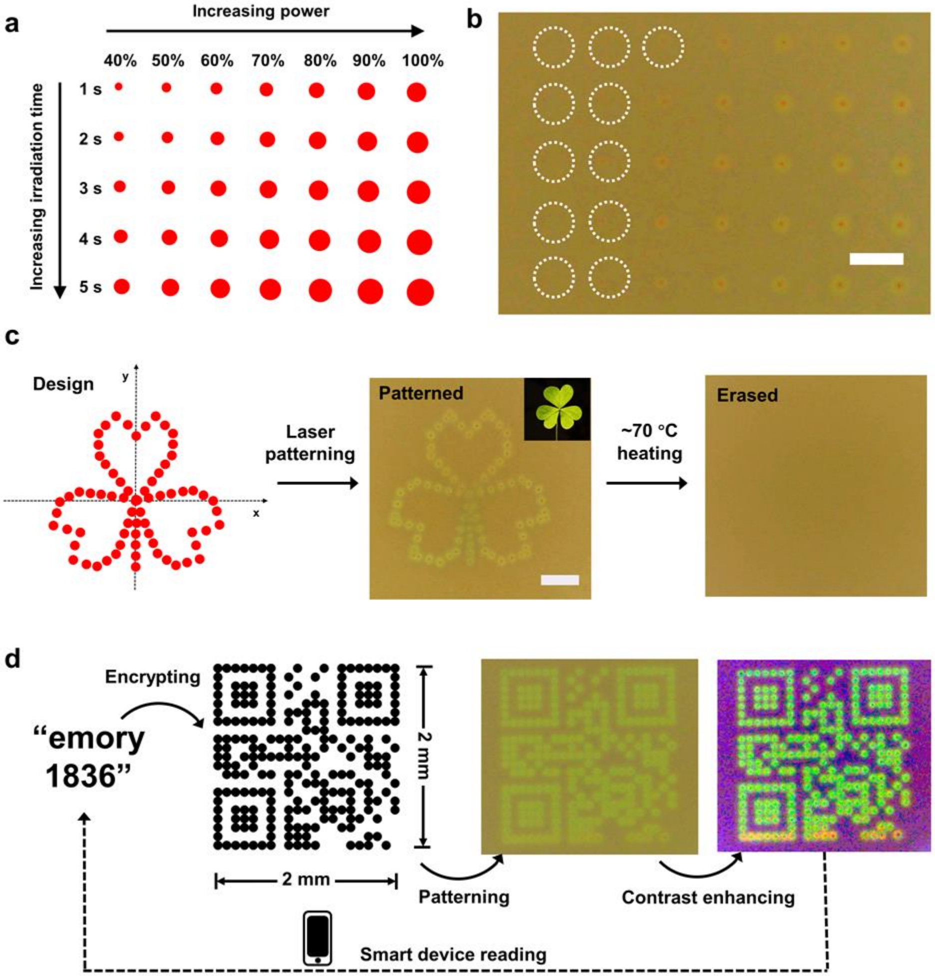

Figure 3.7. **Laser patterning demonstrations of in-situ assembly of DNA supramolecular hydrogels**. a) Laser patterning map based on different laser power and laser irradiation times. Note that 100% laser power is around 49.7 mW. b) Digital photograph of the laser patterned spots based on the design of a) (scale bar 300 µm). c) A laser patterning design of a 3-leaf clover after the patterning and the real image (top inset). The patterned image can be erased by bulk heating. Scale Bar 400 µm. d) A flow diagram demonstrates encrypting application of on-demand assembly. A QR code encrypting the text "emory 1836" was generated first by software. Then, we photo-patterned the QR code (2 mm x 2 mm) with on-demand assembly technology in this work. After adjusting the contrasts of the microscope image, the QR code was read by a smart device to reveal the encrypted information. Note: All hydrogels were imaged at room temperature in the absence of a magnetic field.

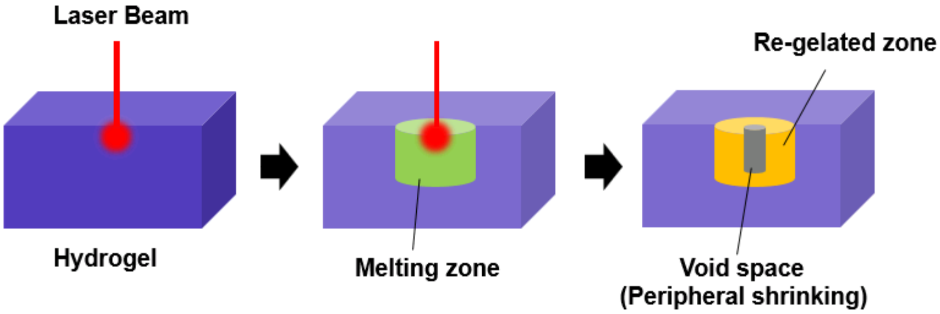

Figure 3.8. Schematic of a possible explanation of the observed dark region formed at the illumination spot within the DNA-PC structures. We hypothesize that these regions arise from peripheral shrinking of the DNA hydrogel.

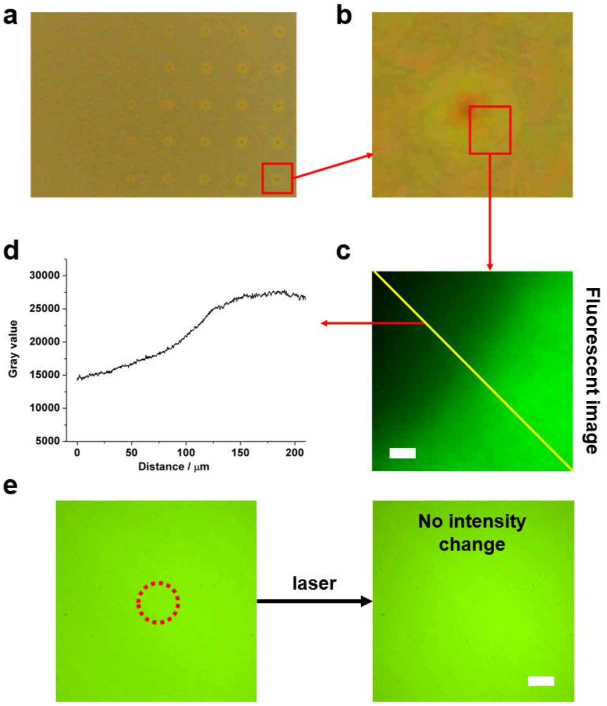

Figure 3.9. Experimental evidence that supports the model illustrated in Figure 3.8. In this experiment, we used 6-carboxyfluorescein (FAM) labeled ssDNA to form the hydrogel in the same manner as described previously. a) and b) Typical spots that have a dark center in the middle. c) A fluorescence image that shows the intensity difference near the laser writing spot demonstrating reduced fluorescence. The dark area indicates a lower density of ssDNA. d) The intensity line scan plot in c). e) A control group without any MNPs. Since heating is produced by MNPs, removing the particles abolishes heating and local dehybridization of the DNA. This control group shows that photobleaching is minimal when illuminating with the 785 nm laser source. This is consistent with the spectral properties of FAM with its λ_{max} = 495 nm. Scale bars: 20 μm.

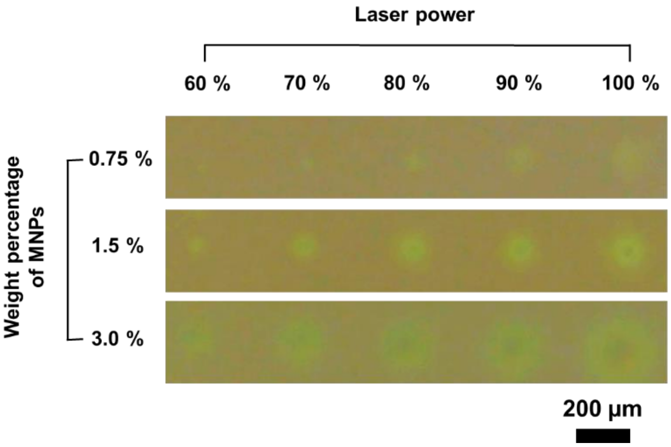

Figure 3.10. Measurement of patterning area in DNA hydrogels as a function of the concentrations of MNP particles (200 nm diameter MNPs). The horizontal direction represents increasing laser powers. Vertical values represent the wt/wt% for MNPs doped DNA hydrogels.

3.3 Conclusions

In summary, we demonstrate an on-demand structural color patterning technology using a DNA supramolecular hydrogel system with high spatial and temporal resolution. The gel is crosslinked using all non-covalent Watson-Crick-Franklin interactions which are advantageous because these can be easily programmed. The self-assembly of MNP created PC structural color which could be controlled and erased on demand based on specific thermal, optical and magnetic inputs. Rheology measurements of the hydrogel composite show highly reversible and rapid crosslinking/de-crosslinking kinetics which were observed for the three palindromic DNA sequences tested (12, 16, and 20 mer domains). Generating PC coloration required transient de-crosslinking of the gel while simultaneously applying an external magnetic field to assemble the MNP. This coloration was rapidly erased when the gels were transiently de-crosslinked in the absence of a magnetic field. Because of the strong visible and near-IR absorbance of the MNPs, structural color could be patterned in a facile manner using a near-IR laser source with micrometer spatial resolution and sub-sec temporal resolution. It is important to note that there are many reported examples of rewritable materials and these are based on organic dye[233, 235], PC[236, 237] and metal-organic framework (MOF)[29] materials. In contrast to organic dye materials, PCs offer more stable coloration that resists photobleaching and degradation that is well documented for organic dyes and pigments. Other PC-rewritable approaches display slow response times (for writing and erasing) as these systems require a volumetric swelling/deswelling change in the polymer matrix. For example, water triggered reversible PC coloration required ~5-10 min response times[26]. By leveraging the rapid and highly localized gelation/de-gelation kinetics of palindromic DNA our strategy offers high spatial resolution (up to ~10 μm), direct-write color patterning without the need for a photomask, and with rapid patterning (<1s) and erasing time (<10s). Supplementary information Table 1 compares some of the reported technologies to generate re-writable materials. Finally, we note that the fundamental strategy disclosed here might inspire other applications such as chemical sensing, molecular diagnostics, and information storage due to the programmability and sensitivity of DNA-based hydrogels.

3.4 Materials and methods

All chemicals were purchased from Millipore Sigma unless noted otherwise. All DNA strands are custom synthesized by Integrated DNA Technologies (Coralville, IA). The DNA sequences are listed in **Figure 3.3** in the main text.

3.4.1 Synthesis of Fe_3O_4 nanoparticles

The protocols for the synthesis of MNPs was adapted from our previously published work[207]. Briefly, 0.65 g $FeCl_3$, 40 mL ethylene glycol, 3.0 g sodium ascorbate, 1.05 g Poly(4-

styrenesulfonic acid-co-maleic acid) sodium salt (M_w~20,000; 1:1 4-styrenesulfonic acid:maleic acid mole ratio), 14 mg D-isoascorbic acid, and 120 μL DI H_2O were added consecutively into a beaker sealed by parafilm. After vigorous magnetic stirring for about 40 min, a homogeneous mixture was formed and then 0.6 g NaOH was added. The mixture was stirred for 1-2 h until all the NaOH pellets were dissolved completely. The mixture was then transferred into a capped 50 mL Erlenmeyer flask and then allowed to react in a preheated oven (190 ˚C) for 9 h. The Fe_3O_4 products were separated from the solution using an external rare-earth (NdFeB) magnet and washed. Initially, the particles were washed with 30 mL of 50% ethanol solution three times, and then washed three additional times with DI water. To generate smaller (~100 nm) and larger (~130 nm) sizes of nanoparticles, we tuned the amount of added water to 180 μL and 110 μL, respectively.

3.4.2 Synthesis of Fe_3O_4@SiO_2 nanoparticles

The as-synthesized magnetite particles were re-dispersed in 30 mL of DI water. A 12 mL aliquot of this dispersion was then mixed with 80 mL ethanol and 4 mL ammonium hydroxide (25-28 wt%) under vigorous mechanical stirring for 1 min. This solution was warmed by using a water bath that was set to 50 ˚C. Subsequently, two aliquots of tetra-ethyl orthosilicate (TEOS) were added every 20 min. The volume of the first aliquot was 0.4 mL and the second aliquot was 0.2 mL. Eventually, the reaction products were collected by a NdFeB magnet and washed with ethanol three times. Each ethanol wash used a brief 2 min sonication (in order to completely re-disperse particles) and the followed by a magnetic separation step.

3.4.3 Synthesis of Fe_3O_4@SiO_2@PEG nanoparticles

Fe_3O_4@SiO_2 nanoparticles were first modified with 3-(trimethoxysilyl)propyl methacrylate before coating with PEG. Briefly, a 3 mL aliquot of the particle ethanol dispersion was added to 80 μL of 3-(trimethoxysilyl) propyl methacrylate and 5 μL de-ionized water. The mixture was sonicated briefly for 1 min and then placed onto a temperature-controlled shaker to shake for 48 hr at 37 ^{o}C. The silane modified nanoparticles were firstly washed with ethanol once and then washed with DI water twice. The particles were finally dispersed in 3 mL DI water.

The 3 mL particle dispersion was boiled together with 100 mL de-ionized water for 5 min. The entire mixture was cooled down to 90 ^{o}C afterwards. 1 mL poly(ethylene glycol) methyl ether methacrylate (Mn~500), 0.3 mL poly(ethylene glycol) diacrylate (Mn~700), and 0.2 mL potassium persulfate solution (100 mM) were added consecutively. The reaction was conducted at 90 ^{o}C for 3 hrs under N_2 flow. The reaction products were washed with DI water once and 75 mM potassium phosphate buffer (pH=6.4) twice. Finally, the particles were concentrated and redispersed in 1.5 mL of 75 mM potassium phosphate buffer (pH=6.4).

3.4.4 Hydrogel nanocomposite with MNPs for on-demand assembly

To synthesize MNP-DNA supramolecular hydrogel nanocomposites, 15 μL MNP dispersion of Fe_3O_4@SiO_2@PEG (in 75 mM potassium phosphate buffer) was directly mixed with 15 μL DNA solution (~3.3 mM in water) in an Eppendorf tube. The mixture was pre-heated to ~90 ^{o}C in a water bath first, then a vortex mixer (~15 s mixing time) was used to create an homogeneous mixture. Note that mixture will rapidly gelate if cooled below 90 ^{o}C transiently, and the sample must be heated again to ~90 ^{o}C before handling and transferring to form the thin film. Two glass slides were pre-warmed to 90 ^{o}C and a 30 μL drop of the warmed hydrogel was sandwiched and allowed to spread. The thickness of the hydrogel was controlled by using parafilm as a spacer. We used 4 layers of parafilm spacer for most of the experiments described in this paper as we found that thinner films formed weakly colored hydrogels.

For the MNP-polyacrylamide hydrogel nanocomposite, the polyacrylamide hydrogel was pre-made by using radical polymerization. 5 mg acrylamide, 33μL pre-annealed DNA duplex 1 mM solution (the DNA duplex was acrylamide terminated on 5’ end as crosslinker), 1 μL saturated solution of potassium persulfate, and 0.5 μL of N,N,N′,N′-tetramethylethylenediamine were mixed together and allowed to gelate at room temperature for 24h. The mixing step with the MNP solution was identical to the DNA supramolecular hydrogel solution. However, the mixing step required greater effort as the DNA crosslinked polyacrylamide hydrogel was not completely melted at 90 ^{o}C.

DNA sequences for polyacrylamide crosslinking are listed as below:

Strand #1 /5’Acryd/TT TTT TTT TTG GTA GCG AGT TAG GGA GCC GA 3’

Strand #2 /5’Acryd/TT TTT TTT TTT CGG CTC CCT AAC TCG CTA CC 3’

3.4.5 Characterization

TEM images were acquired with a Hitachi HT-7700 with 80 kV accelerating voltage. Reflectivity spectra were measured with a FLAME-S-VIS-NIR Spectrometer equipped with a premium 400 μm reflection probe (Ocean optics Inc., Dunedin, FL). The spectrometer was calibrated with a diffuse reflectance standard (PTFE) prior to all the measurements. All the spectra data were recorded through the Ocean View 1.6.3 software package.

Rheological tests were carried out on an AR2000ex rheometer equipped with a temperature controller. The rheological experiments were performed on 25 mm parallel plates using 100 μL of particle-contained hydrogels (particle dispersion: DNA gel solution=1:1 by volume). The gap size was set with 0.12 mm. Frequency sweep tests were carried out on mixtures between 0.01 Hz to 1000 Hz at 25 ^{o}C at a fixed strain of 1%. Temperature sweep tests were carried out at 6.28 rad/s with specific temperature range based on specific sequence (for details see **Figure 3.3**).

The laser patterning imaging was performed using a Nikon Eclipse Ti microscope, operated with Nikon Elements software, a 1.49 NA CFI Apo 100x objective equipped with a perfect focus system and LED light source along with a laser excitation source. An RICM filter cube with a 535 nm excitation filter was employed to visualize particle alignment. Laser patterning was using a UGA-42 Firefly galvo mirror illumination system (Rapp OptoElectronic, Germany) with the ROE Syscon-NIS software (version 1.1.9.9, Rapp Optoelectric) to spatiotemporally control a 785 nm NIR laser at 50 mW power. The demonstration images (in **Figure 3.7**) were taken by Magic Zoom™ 1080p microscope camera.

CHAPTER 4. HYDROGEL BASED CELLULAR TENSION-SENSING MATRIX

4.1 Introduction

Mechanical force determines the fate and function of a variety of cells[238-240]. There are intensive studies focusing on cellular mechanobiology for a broad range of motivations that span from fundamental biology development to diagnostic applications. For example, stem cells have been shown to sense and respond to the stiffness of the underlying substrate, steering differentiation based on the mechanical properties of the cellular microenvironment[241]. Our lab has developed molecular tension fluorescence microscopy (MTFM)[242, 243] as a tool to visualize molecular forces, in addition to other existing methods such as magnetic tweezer[244, 245], traction force microscopy[246], etc. However, most of our MTFM-based force sensing probes are modified on a glass surface, which limits the ability to study how cells behave in the varying stiffnesses of human body tissues. To better simulate the authentic biological environment and investigate different cellular responses affected by substrate stiffness, we have developed a hydrogel-based cellular tension sensing matrix.

The first step is to choose a biocompatible hydrogel that can be facilely modified with DNA tension probes. Poly (ethylene glycol) (PEG) or PEGylated molecules have been demonstrated with great biocompatibility in many existing research literature[247, 248]. In this work, we take advantage of the protocol in **Chapter 2** to synthesize a robust PEG hydrogel material. We adjust the stoichiometry of 4-arm-PEG-NH_2 to be slightly higher than 4-arm-PEG-NHS so that the DNA tension probes could be modified onto the surface through amine related chemistry (**Figure 4.1**). Additionally, all the DNA tension probes modified on the PEG hydrogel surface are Phosphorothioate-(PS-) modified. The PS modification is to prevent the cell-produced nuclease from degrading the tension probes. Comparing with the glass surface that used in previous MTFM works[243], hydrogel surface is more challenging for cells to adhere, and therefore require longer incubation times and better stability of DNA tension probes.

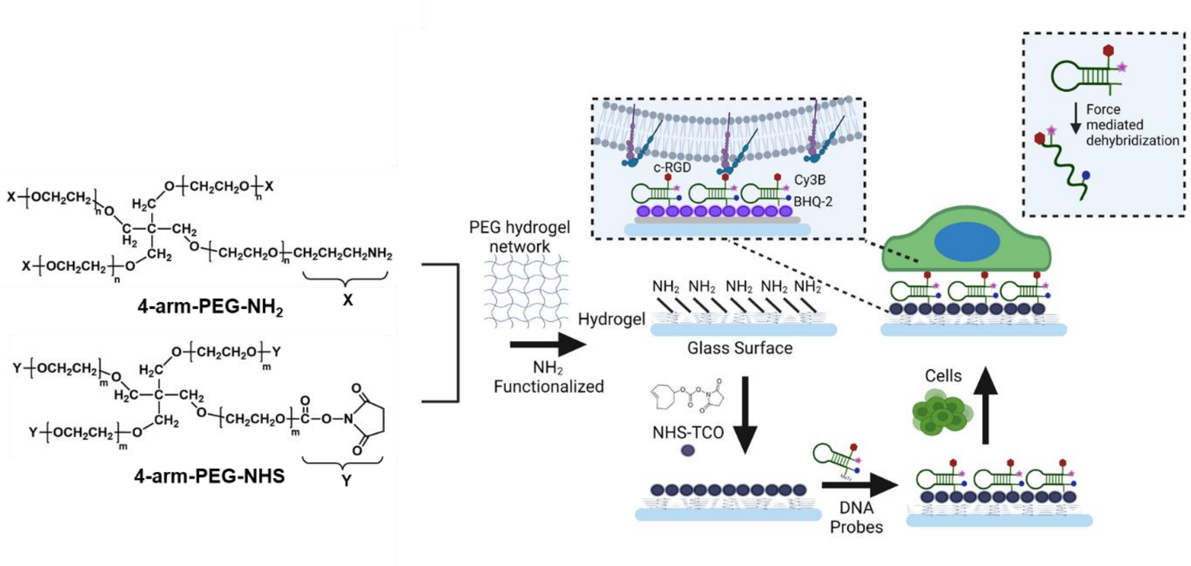

Figure 4.1. Schematic of synthesizing hydrogel tension sensing matrix. The PEG hydrogel tension sensing matrix is fabricated by four major steps. The first step is the gelation process by mixing two PEG molecules with different terminal groups. The second step is to modify the amine residues on the hydrogel surface to introduce TCO groups. Once the surface is functionalized by TCO groups, we added PS modified DNA hairpin tension probe with tetrazine modification. In the end, we spread cell suspensions on the gel surface so that the cell could bind to the cRGD on the PS-modified DNA probes.

4.2 Results and discussions

Most of the biological tissues have relatively robust but diverse mechanical properties. Taking human tissues as examples, the ultimate tensile strength could span from 100 kPa to 100 MPa, while the elastic modulus could span from 1 kPa to 1 GPa[249]. In order to develop a generalized tool for cellular force measuring, we have synthesized PEG hydrogel with controlled modulus that mimic the mechanical properties of biological tissues. The elastic modulus of PEG hydrogel is controlled by tuning the crosslinking density of the hydrogel. We use PEG precursor molecules with different molecular weight to synthesize hydrogels. Theoretically, with same polymer weight content (~10 wt%), the hydrogel that is synthesized from lower molecular weight precursors will have higher modulus compared to the one that is synthesized from higher molecular weight. We next performed the time dependent rheology experiments to examine the modulus-tuning hypothesis (**Figure 4.2**). To begin with, three different pieces of hydrogels were synthesized with precursor molecules with 5k a), 10k b), 20k c), respectively. After mixing the precursor molecules of 4-arm-PEG-NH_2 and 4-arm-PEG-NHS, the mixture was swiftly added to the rheometer and started the tests. The elastic modulus G'_{max} of hydrogels after 50 min were 14 kPa a), 6 kPa b), and 2 kPa c), which agreed with our hypothesis. To note, the molecular weight of the precursor also affects the gelation kinetics. The gelation kinetic of lower molecular weight precursor will be much faster than the one that has larger molecular weight. This phenomenon is due to the molar difference of reaction group pairs (NHS/NH_2) in the precursor mixture.

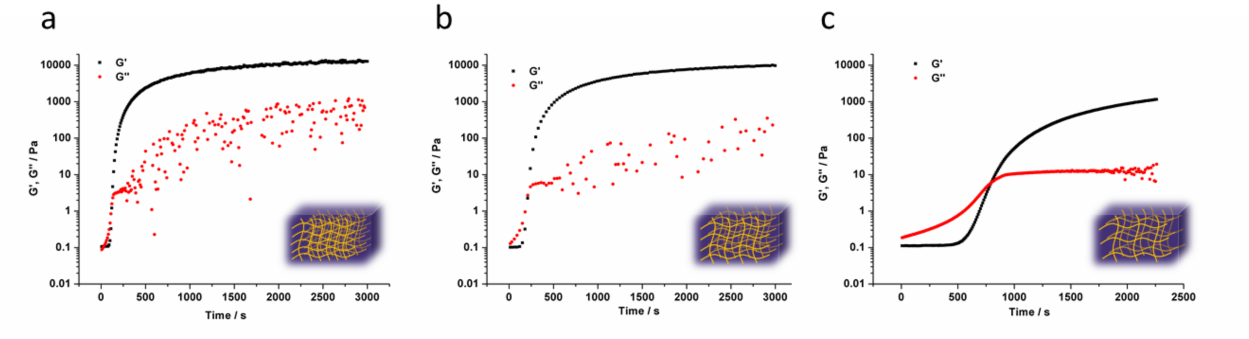

Figure 4.2 Rheology results of PEG hydrogels that is synthesized with different precursor molecules. a) hydrogel that is synthesized from Mw~5,000 PEG precursor molecules; b) hydrogel that is synthesized from Mw~10,000 PEG precursor molecules. c) hydrogel that is synthesized from Mw~20,000 PEG precursor molecules. The elastic modulus G'_{max} for each hydrogel is a) ~14 kPa, b) ~6 kPa, and c) ~2 kPa. Insets: schematic of hydrogels with different crosslinking density. The crosslinking density determines the elastic modulus of PEG hydrogel.

In order to examine the optimal DNA concentration for hydrogel surface chemistry, we use the same TCO/Tetrazine chemistry to bind 24 mer ssDNA with different concentration onto the hydrogel surface (**Figure 4.3**). In theory, the surface that was modified with higher density DNA strands will correspond with higher fluorescence intensity since each DNA strand is labelled with Cy3B dye. The final results are shown by the microscope images (middle) and the plot of DNA concentration calibration (right). From this experiment, we confirm the optimal DNA concentration for surface functionalization is 300 nM.

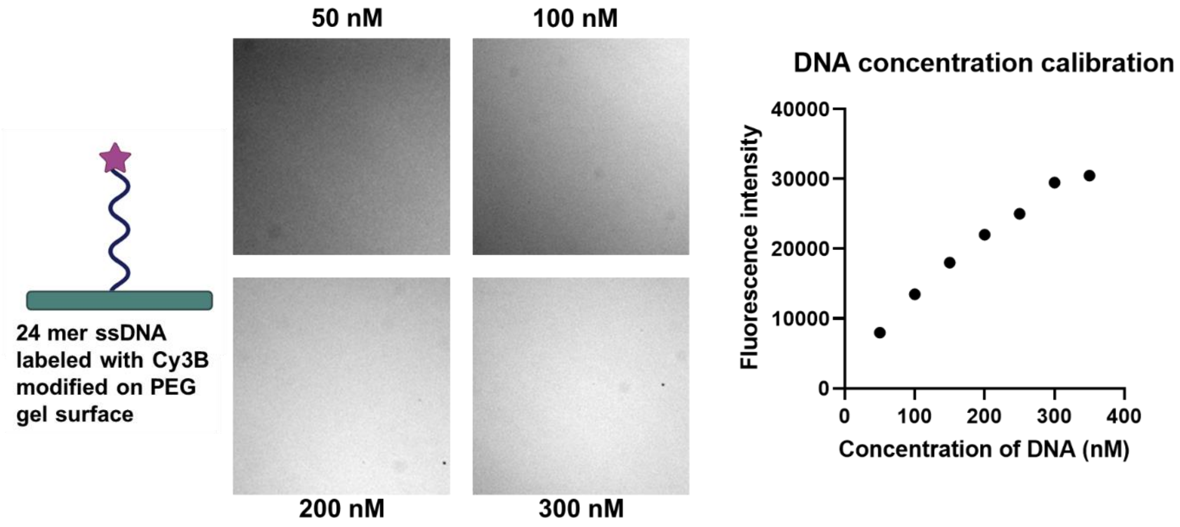

Figure 4.3 DNA concentration calibration for hydrogel surface chemistry. Left: schematic of hydrogel surface that is modified with 24 mer ssDNA; Middle: fluorescence microscopy images for the surface that was treated with 50 nM/100 nM/200 nM/300 nM DNA solution for 2 hours; Right: Fluorescence intensity under microscope as a function of the DNA concentration.

We next use HeLa cells to test the MTFM tension signal on PEG hydrogel. The cells are split and incubated on the hydrogel surface for more than 5 hours before imaging. BF images in Figure 4.4 shows that the cells are well-spread on the surface of the hydrogel. Fluorescence imaging results (TRITC) reveals fluorescence signals located on the peripheral region of the cells, which is likely to be the cellular tension signal. Other types of cells (like 3T3, C2C12) showing similar results of cellular tension signal.

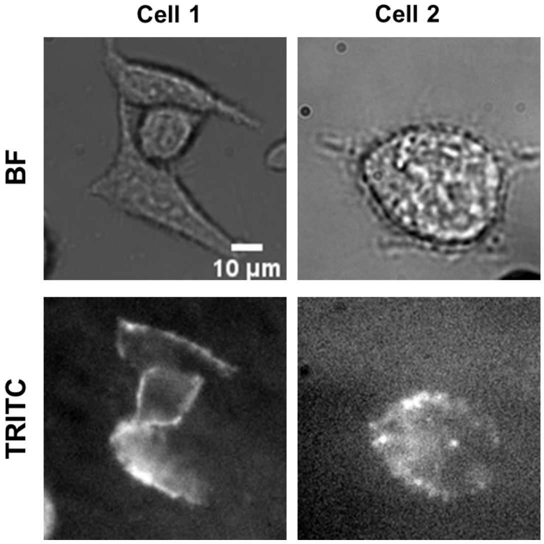

Figure 4.4 Bright field (BF) and fluorescence images (TRITC) of HeLa cells on PEG hydrogel surface. Hydrogel elastic modulus: ~14 kPa.

To confirm the fluorescence signals in Figure 4.4 are actual tension signal, we performed two different control groups. The first control group is to test if the fluorescence signal is due to the specific binding between cRGD and integrin. We modified the surface with/without cRGD on DNA tension probe. We found that the surface without cRGD modified on DNA probes shows very weak signal compare to the surface with cRGD on DNA probes (**Figure 4.5 a** and **b**). The second control group use Latrunculin B (LatB), an inhibitor of actin polymerization, to prove that the fluorescence signal is mostly due to the cellular force rather than the internalization of fluorophores. We found that the integrated fluorescence intensity is over 50% lower after LatB treatment. Both experiments indicate that the fluorescence signal is mainly contributed by the cellular force.

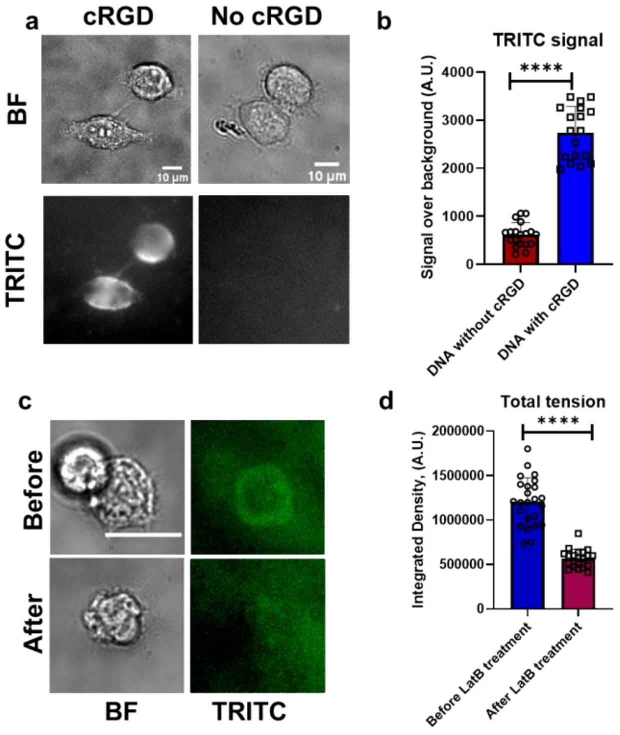

Figure 4.5 Microscopy and statistic results of HeLa cells attached on PEG hydrogel surface. a) Representative microscope images of HeLa cells on hydrogel surfaces that is modified with DNA-cRGD or DNA tension probes. b) statistically results of the fluorescence images showing in a). c) Representative microscope images of HeLa cells before and after treated with LatB. d) statistics results of the fluorescence images shown in c). **** indicates $p < 0.0001$. Scale bar in c is 20 µm.

It is of great interest to study the cellular tension on hydrogel matrix with different stiffness.[250] We employed the modulus tuning method of PEG hydrogel described previously. By performing the same experiments, we obtained some preliminary results of cellular tension signals (**Figure 4.6**). Bright field microscopic images show different attaching behaviors of HeLa cells with hydrogels that have elastic modulus of 14/6/2 kPa (**Figure 4.6a**). The cells are most elongated and spread with larger area on 14 kPa hydrogel surface. Upon decreasing the hydrogel elastic modulus from 14 kPa to 2 kPa, we found that the spreading area of the cell decreased about 50% (Figure

4.6b). Furthermore, similar trend has also been found in fluorescence signal of cells, which cells attached on stiffer substrate shown stronger tension signal (**Figure 4.6 c**). One possible explanation is the viscoelastic nature of polymer-based hydrogel materials, which the material exhibits both elasticity and viscosity behavior under external stress[251, 252]. The viscosity property of the hydrogel surface would provide unstable anchors for an attaching cell, which compromises the cell adhesion and further spreading. The mechano-transduction of living cells is also weakened since the cells relies on effective bindings to exert force. Another possible explanation is that the softer PEG gels have porous structure with larger pore size due to less crosslinking density. The larger pores could inhibit the formation of the extracellular matrix if the cell secreted protein molecules diffuse through the hydrogel networks.

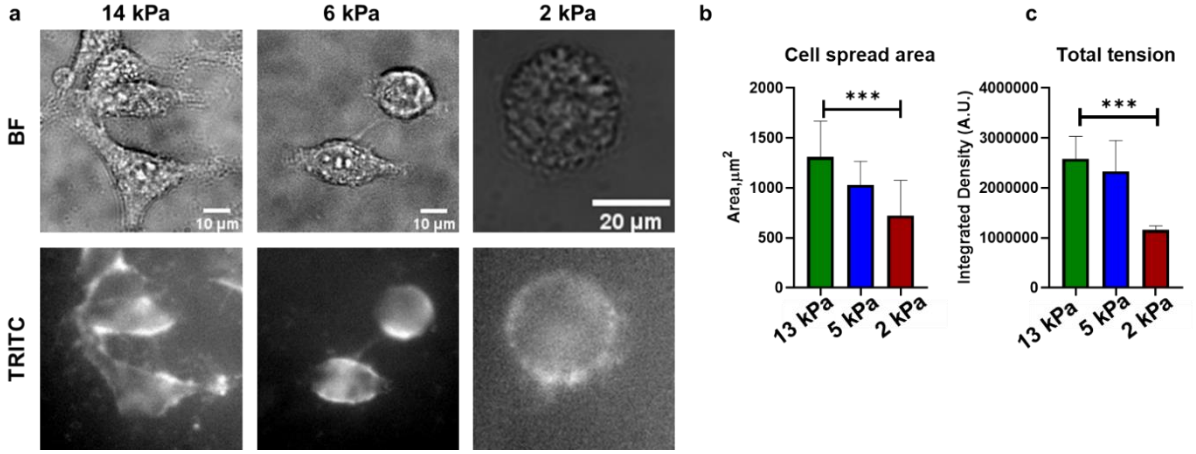

Figure 4.6 Cellular tension of HeLa cells with PEG hydrogels that have different elastic modulus. a) Microscope images of cells on 14/5/2 kPa hydrogel surface. b) and c) statistic results about cell spreading area and tension signal intensity. *** indicates $p < 0.001$.

Hydrogels for 3D cell/tissue culturing has become of great interest in recent years[253, 254]. Important applications such as apoptosis studies[255], tumor modeling[256], and therapy development[257] have been developed through this technology. Imaging cellular tension in 3D or pseudo-3D environments could provide valuable information of cells upon differentiating, migrating, and mechano-transducing. In this work, we programmed our tension-sensing hydrogel surface with lab-on-a-chip technology (**Figure 4.7a**). A 6’’ silicon master is customized and purchased from TERA-print with patterned pyramid structure of 20x20x10 µm. In order to replicate the pattern onto the PEG hydrogel surface, a PDMS stamp is created by curing the liquid PDMS precursor (Sylgard 184®) on the top of the silicon master. Then, the PEG hydrogel is cured on this PDMS stamp. After the hydrogel is peeled off from the PDMS stamp, the pattern on silicon master will be replicated on the hydrogel surface. The dented pattern is expected to hold living cells inside so that the cellular tension can be imaged beyond 2D.

A bright field (BF) microscope image and a fluorescence (TRITC) microscope image were shown in **Figure 4.7b**. The BF image demonstrates the pyramid pattern is successfully transferred onto the hydrogel surface, with the cells conforming to the designed structure. These results align with the fluorescence images showing similar tension signals as displayed in **Figure 4.6**. It is worth noting that the cells have not completely infiltrated the “pyramid” structure due to the larger size of the spread cells. Therefore, readers should expect an optimization of the pyramid dimensions in future work. We also took z-stack images near the patterned region to reconstruct the 3D tension signal. However, due to light diffusion between different z-planes, the 3D reconstruction could not reveal the tension signal with distinct resolution. The preliminary results of 2.5D tension signal indicates the need for optimization in both the silicon master design and the imaging approach of cellular tension.

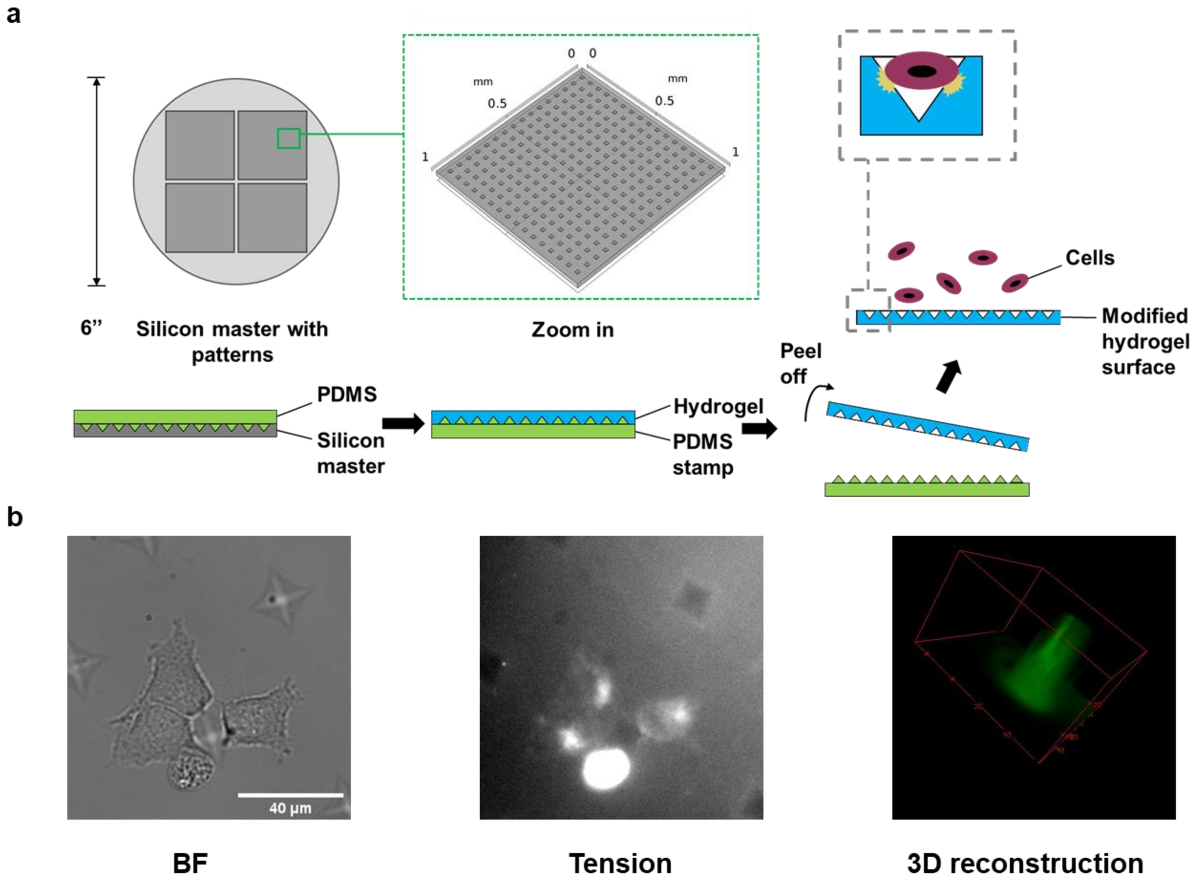

Figure 4.7 Preliminary results of 2.5D cellular tension sensing. a) Schematic of creating a 2.5D hydrogel surface for cellular tension sensing. b) Preliminary microscope results for cellular tension sensing on 2.5D hydrogel surface.

4.3 Conclusions

In summary, we have expanded the toolbox MTFM technology by synthesizing a PEG hydrogel matrix that can respond to cellular tension. The PEG hydrogel provides a biocompatible, modulus tunable, and robust matrix that mimics the physiological conditions in living tissues. Experiments with LatB treatment indicate the fluorescence signals on a hydrogel surface mostly represent cellular tension force rather than autofluorescence. Additionally, we have found that HeLa cells produce strong mechanical force as well as a larger spreading area on a stiffer substrate. In the end, we use lab-on-a-chip technology to create a 2.5D hydrogel surface as the first step towards 3D tension sensing. These results provide guidance for future developments of hydrogel-based tension sensing matrix.

4.4 Materials and methods

4.4.1 Synthesis of Phosphorothioate- (PS-) modified tension probes

PS modified tension probes were synthesized by the sequential copper mediated azide-alkyne cyclization reaction (CuAAC), NHS-Amine coupling reaction, and strain promoted azide-alkyne cycloaddition reaction (SPAAC). Briefly, alkyne- and amine-modified oligonucleotide with full PS-modification was purchased from Integrated DNA Technology (Coralville, IA). The PS-modified oligonucleotide was first subjected to CuAAC reaction with cRGD/Cy3B-N_3 to introduce cell-adhesive peptide and a fluorophore for tension signal. Next, the amine group of PS-modified oligonucleotide was reacted with DBCO-sulfo-NHS to introduce strained alkyne group. Finally, the strained alkyne group was reacted BHQ2/Tz-N_3 for quencher and surface anchoring moiety, which forms PS-modified tension probe. Detailed synthetic scheme is described in the **Scheme S1**.

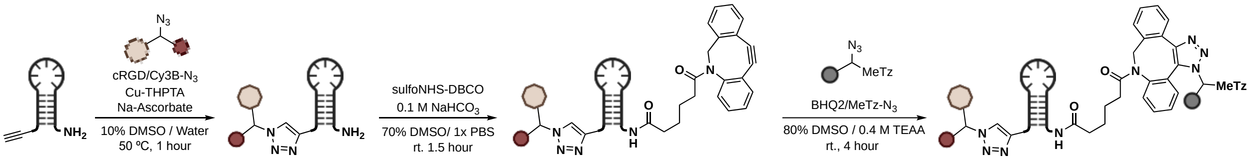

Scheme S1: PS modified (*) DNA sequence (contributed by Dr. Hiroaki Ogasawara): /5Hexynyl/*G*T*A*T*A*A*A*T*G*T*T*T*T*T*T*C* A*T*T*T*A*T*A*C*/3AmMO/

4.4.2 Synthesis of cellular tension sensing hydrogel surface

The PEG gel surface was made by mixing of two precursor solutions. Typically, for hydrogel that was made of 5k molecular weight precursors, the first solution was made by dissolving 55 mg of 4-arm-PEG-NH$_2$ (Mw ~5k; Biopharma PEG, 10225) into 500 µL potassium phosphate buffer (pH~6.4). The second solution was made by dissolving 50 mg 4-arm-PEG-NHS molecule (Mw~5k; NOF America Corp. PTE05GS) into 500 µL potassium phosphate buffer (pH~6.4). Both the solutions were then cooled in an ice bath for 15 min before vigorous mixing using a stir bar (~400 rpm for 5s). Then 20 µL of the mixture was filled in the gap between a parafilm strip and an APTES treated glass surface to form a thin (~80 µm) hydrogel layer and incubated for 1hr at RT. After the gelation, the parafilm strip was peeled off from the PEG gel using tweezers. The gel was then vigorously washed with DMSO for 5 min and incubated with 200 µL of 5mg/mL NHS-TCO in DMSO overnight. The TCO coated peg surface was thoroughly washed with DMSO (3 times), EtOH (3 times), Nano-pure water(3 times) and 1xPBS (3 times) before incubating with 300 nM DNA was incubated for 2hr. The gel was thoroughly washed with PBS (3 times) and cell culture media (3 times) before seeding the Cells.

<Note>: the molecular weight description of 4-arm-PEG molecules refers to the overall molecular weight rather than the molecular weight of one arm. For example, a 4-arm-PEG molecule that has total molecular weight of 5k would have the Mw~5000/4=1250 of each arm.

4.4.3 Cell preparation and incubation

We used HeLa, 3T3, MEF and C_2C_{12} cells as cell model for cell experiments. For 3T3 cells we used 5% CCS (Cosmic Calf serum) with 1% L-glut and 1% antibiotic (Penn strep). The incuFor HeLa and C_2C_{12} we used 5% FBS (Fetal Bovine Serum) with 1% L-glut and 1% antibiotic (Penn strep) as culture condition. We added Cells were incubated on the surface for 3-6 h at 37 ^oC with 5% serum and 1% antibiotic (P/S).

4.4.4 Immunostaining

For staining on rupture probes, HeLa, MEF, 3T3 and C_2C_{12} cells were fixed and stained on different stiffness of hydrogel surfaces following 3-6hrs of cell spreading. Cells were fixed in 2–4% formaldehyde in 1× PBS for 8–10 min. Cells were permeabilized for 3 min with 0.1% Triton X-100 and were blocked with BSA for 30 min. Staining was performed for 1 h at room temperature with 1:1000 Alexa 488-Phalloidin (ab176753, Abcam), 1:50 Vinculin Antibody SF9 647 (sc-73614 AF647, Santa Cruz Biotechnology), 1:50 Phospho-Paxillin (Tyr1888) Polyclonal Antibody (PA5-17828, Thermo Fisher) followed by 1:5500 Alexa Fluor 555 goat anti-rabbit (A21147, Thermo Fisher), or followed by 1:1000 Alexa Fluor 647 or 488 goat anti-mouse IgG2b (γ2b) (A28175 or A28181) or goat anti rabbit secondary antibody(A27034 or A27080) from Thermo Fisher as indicated in the experiment details. Immunostained cells were imaged using total internal reflection fluorescence microscopy (TIRFM).

4.4.5 Drug treatment

CMCs were pretreated for (>1hr @RT) with various inhibitors before seeding. Cells were either treated with 25 μM Y27632 dihyrdochloride (Y0503, MilliporeSigma) for 30 min, or with 10 μM eptifibatide (Cas no- 881997-860) or with 10μM Blebbistatin (18-521, Fisher Sci) for 30 mins or with 25 μM latrunculin B for 30mins. We used DMSO as a solvent vehicle for the control group.

4.4.6 Characterization

Rheology characterizations were carried out on an AR2000ex rheometer equipped with a temperature controlling stage. The rheological experiments were performed between a 25 mm parallel plate and a stainless-steel stage using 100 μL of PEG hydrogel precursor mixtures (the mixture is still in liquid form when just added on rheometer). The gap size was set with 0.1 mm. The rheological tests described in this chapter is based on oscillation mode, where the top plate is rotating back and forth with a certain amplitude and frequency. More specifically, the time-dependent rheological tests were carried out at 25 ^{o}C with a fixed strain of 1% and frequency 1 Hz. Frequency sweep tests were carried out on mixtures between 0.01 Hz to 1000 Hz at 25 ^{o}C at a fixed strain of 1%.

Live and fixed cells were imaged in either 5% serum buffer or PBS at 25 °C using a Nikon Eclipse Ti microscope driven by the Elements software package. The microscope is equipped with Evolve electron multiplying charge coupled device (Photometrics), an Intensilight epifluorescence source (Nikon), a 40× NA objective (Nikon). All of the reported experiments were performed using the following Chroma filter cubes: DAPI, FITC, TRITC, Cy5 and BF.

CHAPTER 5. SUMMARY AND OUTLOOK

5.1 Summary

In this dissertation, we have designed and synthesized three different functionally responsive hydrogels. In the first research, we seek solutions to the issues regarding volumetric changing of responsive hydrogels. We designed a strain-accommodating smart skin (SASS) with a two-layer composite design that is inspired from chameleon skin. Both finite element simulations and experimental demonstrations confirmed the strain-accommodating behavior of responsive hydrogels. Further experiments demonstrate that a SASS material is also light-responsive due to the photothermal effect of magnetite nanoparticles. Potential applications in camouflage, anti-counterfeiting, and chemical sensing are envisioned for SASS material. The second research project focuses on insitu assemblies of magnetic nanoparticles in a responsive DNA supramolecular hydrogel. As an extension project for the first research, the in-situ/on-demand assembly of magnetic nanoparticles also demonstrate the strain accommodating behavior because of the development of a new responding mechanism. Due to the fast gelation/de-gelation kinetics of DNA supramolecular hydrogel, the magnetic nanoparticles could fast switch their assembly states on-demand. Moreover, this on-demand assembly can be easily manipulated with a focused laser and create photonic patterns with high spatial and temporal resolution. Potential applications such as rewritable technology, information encryption, and information storage are envisioned. The third research project focuses on developing a cellular force sensing hydrogel. The functionality of the responsive hydrogel is to measure and map the mechanical force at piconewton levels. Compared with the tension signal that is measured from a glass surface, hydrogel tension sensing matrix provides a physiologically identical condition for living cells. Additionally, by altering the molecular weight of the precursor molecules, the stiffness/modulus can be finetuned.

We found that living cells tend to show stronger tension signal on stiffer hydrogel substrate. In the end, the flexible hydrogel matrix can also be engineered with secondary structures to form a 2.5D surface so that the integrin forces might be measured beyond a two-dimensional region.

5.2 Outlook

What does the future hold for functionally responsive hydrogels? Anticipating how the field will evolve over the next few years is not easy, as there has been a rapid rate of new developments in responsive hydrogels. An important area for this field is honing more comprehensive fabrication technologies used to create responsive hydrogel devices. The vast majority of current hydrogel take the form of thin films, rods, and other simple shapes. While complex architectures have been achieved by assembling these rudimentary shapes together or creating rationally designed self-assembly structures, it is likely that improved 3D printers and lithography techniques over the next few years will allow the manufacture of exciting new hydrogel geometries.

As scientists begin to create responsive hydrogels more efficiently and with more varied architecture, the practical application of these materials is expected to grow as well. One area of expansion will be to create more advanced robotic/actuating systems, increasing the complexity of their functions and operations, along with programming more autonomy into these structures. Such self-actuating soft robots could fill a unique niche in both size and sensitivity that traditional robotics may not be optimized for.

Medical treatment is another area with great potential for future responsive hydrogel development. As drug delivery vehicles, responsive hydrogels have already shown great promise for specific localization and release of therapeutics. This could be particularly advantageous for cancer treatment, carrying toxic chemotherapy drugs directly to tumors and minimizing off-target effects. The sensing abilities of responsive hydrogel may also be further enhanced to develop a self-releasing insulin delivery platform, which may improve quality of life for diabetic patients. Additionally, responsive hydrogel will likely be further developed for regenerative medicine applications. Many bio-material strategies work to mimic the physiological environment of a target tissue in structure and chemical composition, and incorporating native mechanical cues is a logical next step in the field.

At last, the representative models for functionally responsive hydrogels are often biological systems such as skins, muscles, cellular matrices, etc. Many studies are inspired from natural examples, such as smart skin systems that will likely see increased growth in the coming years, as their multi-responsive nature lends them to many applications across multiple industries. Photonic smart skins hold great potential, ranging from microscale force sensing to next-generation camouflage and cloaking technologies. Biocompatible smart skins may also see development for medical sensing and diagnostics as at-home and point-of-care testing continues to gain popularity.

APPENDIX A. ATTRIBUTION OF EFFORTS AND COPYRIGHT STATEMENT

a. Part of the content in **Chapter 1** are readapted with permission from my publication Ref. 226 Copyright 2021 Wiley-VCH, Weinheim.

b. The author thanks Dr. Wei Sun and his lab members for their contribution of the works described in **Chapter 2**. This collaboration led to my publication (Ref. 127) and part of the content in this chapter is readapted with permission from my publication Ref. 127 Copyright 2019 American Chemical Society, Washington DC.

c. The author thanks Dr. Eric R. Weeks and his lab members for their contribution of the rheology work described in **Chapter 3**. This collaboration led to my publication (Ref 21) and part of the content in this chapter is readapted with permission from my publication Ref. 21 Copyright 2021 American Chemical Society, Washington DC.

d. The author and SK Aysha Rashid share equal contributions to the research works described in **Chapter 4**. Also, Dr. Hiroaki Ogasawara contributed to the synthesis of PS modified DNA probe in **Chapter 4**.

APPENDIX B. FUNDING INFORMATION

The research projects described in this dissertation is supported by the following fundings.

NSF DMR 1905947

NIH R01 GM 131099

NIH R01 GM 124472.

DARPA BTO (grant no. HR0011-16-2-0011)

REFERENCES

1. Le, X.; Lu, W.; Zhang, J.; Chen, T., Recent progress in biomimetic anisotropic hydrogel actuators. *Advanced science* **2019,** *6* (5), 1801584.

2. Guan, Q.; Lin, G.; Gong, Y.; Wang, J.; Tan, W.; Bao, D.; Liu, Y.; You, Z.; Sun, X.; Wen, Z., Highly efficient self-healable and dual responsive hydrogel-based deformable triboelectric nanogenerators for wearable electronics. *Journal of Materials Chemistry A* **2019,** *7* (23), 13948-13955.

3. Abe, K.; Kawamata, I.; Shin-ichiro, M. N.; Murata, S., Programmable reactions and diffusion using DNA for pattern formation in hydrogel medium. *Molecular Systems Design & Engineering* **2019,** *4* (3), 639-643.

4. Khoury, L. R.; Popa, I., Chemical unfolding of protein domains induces shape change in programmed protein hydrogels. *Nat. Commun.* **2019,** *10* (1), 1-9.

5. Wang, L.; Zhu, L.; Hickner, M.; Bai, B., Molecular Engineering Mechanically Programmable Hydrogels with Orthogonal Functionalization. *Chem. Mater.* **2017,** *29* (23), 9981-9989.

6. Cheng, Y.; Luo, X.; Payne, G. F.; Rubloff, G. W., Biofabrication: programmable assembly of polysaccharide hydrogels in microfluidics as biocompatible scaffolds. *J. Mater. Chem.* **2012,** *22* (16), 7659-7666.

7. Dong, Y.; Wang, J.; Guo, X.; Yang, S.; Ozen, M. O.; Chen, P.; Liu, X.; Du, W.; Xiao, F.; Demirci, U., Multi-stimuli-responsive programmable biomimetic actuator. *Nat. Commun.* **2019,** *10* (1), 1-10.

8. Zhao, Z.; Wang, C.; Yan, H.; Liu, Y., Soft Robotics Programmed with Double Crosslinking DNA Hydrogels. *Adv. Funct. Mater.* **2019,** *29* (45), 1905911.

9. Takahashi, R.; Wu, Z. L.; Arifuzzaman, M.; Nonoyama, T.; Nakajima, T.; Kurokawa, T.; Gong, J. P., Control superstructure of rigid polyelectrolytes in oppositely charged hydrogels via programmed internal stress. *Nat. Commun.* **2014,** *5*, 4490.

10. Soutif, J.-C.; Brosse, J.-C., Chemical modification of polymers I. Applications and synthetic strategies. *Reactive Polymers* **1990,** *12* (1), 3-29.

11. Duracher, D.; Elaïssari, A.; Pichot, C., Characterization of cross-linked poly(N-isopropylmethacrylamide) microgel latexes. *Colloid and Polymer Science* **1999,** *277* (10), 905-913.

12. Heskins, M.; Guillet, J. E., Solution Properties of Poly(N-isopropylacrylamide). *Journal of Macromolecular Science: Part A - Chemistry* **1968,** *2* (8), 1441-1455.

13. Zhao, J.; Su, H.; Vansuch, G. E.; Liu, Z.; Salaita, K.; Dyer, R. B., Localized Nanoscale Heating Leads to Ultrafast Hydrogel Volume-Phase Transition. *ACS Nano* **2019,** *13* (1), 515-525.

14. Lv, C.; Xia, H.; Shi, Q.; Wang, G.; Wang, Y. S.; Chen, Q. D.; Zhang, Y. L.; Liu, L. Q.; Sun, H. B., Sensitively humidity-driven actuator based on photopolymerizable PEG-DA films. *Advanced Materials Interfaces* **2017,** *4* (9), 1601002.

15. Moe, S. T.; Skjaak-Braek, G.; Elgsaeter, A.; Smidsroed, O., Swelling of covalently crosslinked alginate gels: influence of ionic solutes and nonpolar solvents. *Macromolecules* **1993,** *26* (14), 3589-3597.

16. Gatej, I.; Popa, M.; Rinaudo, M., Role of the pH on Hyaluronan Behavior in Aqueous Solution. *Biomacromolecules* **2005,** *6* (1), 61-67.

17. Qu, X.; Wirsén, A.; Albertsson, A. C., Structural change and swelling mechanism of pH-sensitive hydrogels based on chitosan and D, L-lactic acid. *J. Appl. Polym. Sci.* **1999,** *74* (13), 3186-3192.

18. Lu, B.; Luo, D.; Zhao, A.; Wang, H.; Zhao, Y.; Maitz, M. F.; Yang, P.; Huang, N., pH responsive chitosan and hyaluronic acid layer by layer film for drug delivery applications. *Progress in Organic Coatings* **2019,** *135*, 240-247.

19. Zhou, S.; Wu, B.; Zhou, Q.; Jian, Y.; Le, X.; Lu, H.; Zhang, D.; Zhang, J.; Zhang, Z.; Chen, T., Ionic Strength and Thermal Dual-Responsive Bilayer Hollow Spherical Hydrogel Actuator. *Macromol. Rapid Commun.* **2020,** *41* (8), 1900543.

20. Rothemund, P. W. K., Folding DNA to create nanoscale shapes and patterns. *Nature* **2006,** *440* (7082), 297-302.

21. Dong, Y.; Combs, J. D.; Cao, C.; Weeks, E. R.; Bazrafshan, A.; Rashid, S. K. A.; Salaita, K., Supramolecular DNA Photonic Hydrogels for On-Demand Control of Coloration with High Spatial and Temporal Resolution. *Nano Letters* **2021,** *21* (23), 9958-9965.
22. Tan, Z. J.; Chen, S. J., Nucleic acid helix stability: effects of salt concentration, cation valence and size, and chain length. *Biophysical journal* **2006,** *90* (4), 1175-90.
23. Sardesai, A. N.; Segel, X. M.; Baumholtz, M. N.; Chen, Y.; Sun, R.; Schork, B. W.; Buonocore, R.; Wagner, K. O.; Golecki, H. M., Design and characterization of edible soft robotic candy actuators. *MRS Advances* **2018,** *3* (50), 3003-3009.
24. Liu, X.; Liu, J.; Lin, S.; Zhao, X., Hydrogel machines. *Materials Today* **2020**.
25. Yao, C.; Liu, Z.; Yang, C.; Wang, W.; Ju, X. J.; Xie, R.; Chu, L. Y., Poly (N-isopropylacrylamide)-clay nanocomposite hydrogels with responsive bending property as temperature-controlled manipulators. *Adv. Funct. Mater.* **2015,** *25* (20), 2980-2991.
26. Augé, A.; Zhao, Y., What determines the volume transition temperature of UCST acrylamide–acrylonitrile hydrogels? *RSC Adv.* **2016,** *6* (74), 70616-70623.
27. Ding, Y.; yan, y.; Peng, Q.; Wang, B.; Xing, Y.; Hua, Z.; Wang, Z., Multiple Stimuli-Responsive Cellulose Hydrogels with Tunable LCST and UCST as Smart Windows. *ACS Applied Polymer Materials* **2020**.
28. Hua, L.; Xie, M.; Jian, Y.; Wu, B.; Chen, C.; Zhao, C., Multiple-Responsive and Amphibious Hydrogel Actuator Based on Asymmetric UCST-Type Volume Phase Transition. *ACS Appl. Mater. Interfaces* **2019,** *11* (46), 43641-43648.
29. Gorelikov, I.; Field, L. M.; Kumacheva, E., Hybrid Microgels Photoresponsive in the Near-Infrared Spectral Range. *Journal of the American Chemical Society* **2004,** *126* (49), 15938-15939.
30. Payne, E. K.; Shuford, K. L.; Park, S.; Schatz, G. C.; Mirkin, C. A., Multipole Plasmon Resonances in Gold Nanorods. *The Journal of Physical Chemistry B* **2006,** *110* (5), 2150-2154.
31. Mackey, M. A.; Ali, M. R. K.; Austin, L. A.; Near, R. D.; El-Sayed, M. A., The Most Effective Gold Nanorod Size for Plasmonic Photothermal Therapy: Theory and In Vitro Experiments. *The Journal of Physical Chemistry B* **2014,** *118* (5), 1319-1326.
32. Liu, Z.; Liu, Y.; Chang, Y.; Seyf, H. R.; Henry, A.; Mattheyses, A. L.; Yehl, K.; Zhang, Y.; Huang, Z.; Salaita, K., Nanoscale optomechanical actuators for controlling mechanotransduction in living cells. *Nat. Meth.* **2016,** *13* (2), 143-146.
33. Ramey-Ward, A. N.; Su, H.; Salaita, K., Mechanical Stimulation of Adhesion Receptors Using Light-Responsive Nanoparticle Actuators Enhances Myogenesis. *ACS Applied Materials & Interfaces* **2020**.
34. Acik, M.; Lee, G.; Mattevi, C.; Chhowalla, M.; Cho, K.; Chabal, Y. J., Unusual infrared-absorption mechanism in thermally reduced graphene oxide. *Nature Materials* **2010,** *9* (10), 840-845.
35. Mak, K. F.; Ju, L.; Wang, F.; Heinz, T. F., Optical spectroscopy of graphene: From the far infrared to the ultraviolet. *Solid State Communications* **2012,** *152* (15), 1341-1349.
36. Shi, K.; Liu, Z.; Wei, Y.-Y.; Wang, W.; Ju, X.-J.; Xie, R.; Chu, L.-Y., Near-Infrared Light-Responsive Poly(N-isopropylacrylamide)/Graphene Oxide Nanocomposite Hydrogels with Ultrahigh Tensibility. *ACS Applied Materials & Interfaces* **2015,** *7* (49), 27289-27298.
37. Yang, Y.; Tan, Y.; Wang, X.; An, W.; Xu, S.; Liao, W.; Wang, Y., Photothermal Nanocomposite Hydrogel Actuator with Electric-Field-Induced Gradient and Oriented Structure. *ACS Applied Materials & Interfaces* **2018,** *10* (9), 7688-7692.
38. Cong, H.-P.; Wang, P.; Yu, S.-H., Stretchable and Self-Healing Graphene Oxide–Polymer Composite Hydrogels: A Dual-Network Design. *Chemistry of Materials* **2013,** *25* (16), 3357-3362.
39. Sun, S.; Wu, P., A one-step strategy for thermal- and pH-responsive graphene oxide interpenetrating polymer hydrogel networks. *Journal of Materials Chemistry* **2011,** *21* (12), 4095-4097.
40. Lu, L.; Chen, W., Supramolecular self-assembly of biopolymers with carbon nanotubes for biomimetic and bio-inspired sensing and actuation. *Nanoscale* **2011,** *3* (6), 2412-2420.
41. Shin, S.; Shin, C.; Memic, A.; Shadmehr, S.; Miscuglio, M.; Jung, H. Y.; Jung, S.; Bae, H.; Khademhosseini, A.; Tang, X.; Dokmeci, M., Aligned Carbon Nanotube–Based Flexible Gel Substrates for Engineering Biohybrid Tissue Actuators. *advanced functional materials* **2015,** *25*, 4486–4495.

42. Kamenjicki, M.; Lednev, I. K.; Asher, S. A., Photoresponsive Azobenzene Photonic Crystals. *The Journal of Physical Chemistry B* **2004,** *108* (34), 12637-12639.

43. Takashima, Y.; Hatanaka, S.; Otsubo, M.; Nakahata, M.; Kakuta, T.; Hashidzume, A.; Yamaguchi, H.; Harada, A., Expansion–contraction of photoresponsive artificial muscle regulated by host–guest interactions. *Nature Communications* **2012,** *3* (1), 1270.

44. Ikejiri, S.; Takashima, Y.; Osaki, M.; Yamaguchi, H.; Harada, A., Solvent-Free Photoresponsive Artificial Muscles Rapidly Driven by Molecular Machines. *Journal of the American Chemical Society* **2018,** *140* (49), 17308-17315.

45. Zhao, J.; Su, H.; Vansuch, G. E.; Liu, Z.; Salaita, K.; Dyer, R. B., Localized nanoscale heating leads to ultrafast hydrogel volume-phase transition. *ACS Nano* **2018,** *13* (1), 515-525.

46. Chen, F.; Guo, J.; Xu, D.; Yan, F., Thermo- and pH-responsive poly(ionic liquid) membranes. *Polymer Chemistry* **2016,** *7* (6), 1330-1336.

47. Zarzar, L. D.; Kim, P.; Aizenberg, J., Bio-inspired Design of Submerged Hydrogel-Actuated Polymer Microstructures Operating in Response to pH. *Adv. Mater.* **2011,** *23* (12), 1442-1446.

48. Nakagawa, H.; Hara, Y.; Maeda, S.; Hasimoto, S., A pendulum-like motion of nanofiber gel actuator synchronized with external periodic pH oscillation. *Polymers* **2011,** *3* (1), 405-412.

49. Han, Z.; Wang, P.; Mao, G.; Yin, T.; Zhong, D.; Yiming, B.; Hu, X.; Jia, Z.; Nian, G.; Qu, S.; Yang, W., Dual pH-Responsive Hydrogel Actuator for Lipophilic Drug Delivery. *ACS Appl. Mater. Interfaces* **2020,** *12* (10), 12010-12017.

50. Dai, L.; Ma, M.; Xu, J.; Si, C.; Wang, X.; Liu, Z.; Ni, Y., All-Lignin-Based Hydrogel with Fast pH-Stimuli Responsiveness for Mechanical Switching and Actuation. *Chem. Mater.* **2020,** *32* (10), 4324-4330.

51. Duan, J.; Liang, X.; Zhu, K.; Guo, J.; Zhang, L., Bilayer hydrogel actuators with tight interfacial adhesion fully constructed from natural polysaccharides. *Soft Matter* **2017,** *13* (2), 345-354.

52. Zhang, K.; Liang, Y.; Liu, D.; Liu, H., An on–off biosensor based on multistimuli-responsive polymer films with a binary architecture and bioelectrocatalysis. *Sensors and Actuators B: Chemical* **2012,** *173,* 367-376.

53. Topham, P. D.; Howse, J. R.; Fernyhough, C. M.; Ryan, A. J., The performance of poly (styrene)-block-poly (2-vinyl pyridine)-block-poly (styrene) triblock copolymers as pH-driven actuators. *Soft Matter* **2007,** *3* (12), 1506-1512.

54. Lee, B. P.; Konst, S., Novel hydrogel actuator inspired by reversible mussel adhesive protein chemistry. *Adv. Mater.* **2014,** *26* (21), 3415-3419.

55. Wang, L.; Topham, P. D.; Mykhaylyk, O. O.; Howse, J. R.; Bras, W.; Jones, R. A. L.; Ryan, A. J., Electrospinning pH-Responsive Block Copolymer Nanofibers. *Adv. Mater.* **2007,** *19* (21), 3544-3548.

56. Techawanitchai, P.; Ebara, M.; Idota, N.; Asoh, T.-A.; Kikuchi, A.; Aoyagi, T., Photo-switchable control of pH-responsive actuators via pH jump reaction. *Soft Matter* **2012,** *8* (10), 2844-2851.

57. Le, X.; Lu, W.; Xiao, H.; Wang, L.; Ma, C.; Zhang, J.; Huang, Y.; Chen, T., Fe3+-, pH-, Thermoresponsive Supramolecular Hydrogel with Multishape Memory Effect. *ACS Appl. Mater. Interfaces* **2017,** *9* (10), 9038-9044.

58. Gibson, K. J.; Prominski, A.; Lee, M. S.; Cronin, T. M.; Parker, J.; Weizmann, Y., Discrete pH-Responsive Plasmonic Actuators via Site-Selective Encoding of Nanoparticles with DNA Triple Helix Motif. *Cell Reports Physical Science* **2020,** *1* (6), 100080.

59. Idili, A.; Vallée-Bélisle, A.; Ricci, F., Programmable pH-Triggered DNA Nanoswitches. *J. Am. Chem. Soc.* **2014,** *136* (16), 5836-5839.

60. Cheng, E.; Xing, Y.; Chen, P.; Yang, Y.; Sun, Y.; Zhou, D.; Xu, L.; Fan, Q.; Liu, D., A pH-triggered, fast-responding DNA hydrogel. *Angew. Chem. Int. Ed.* **2009,** *48* (41), 7660-7663.

61. Guo, W.; Lu, C. H.; Orbach, R.; Wang, F.; Qi, X. J.; Cecconello, A.; Seliktar, D.; Willner, I., pH-Stimulated DNA Hydrogels Exhibiting Shape-Memory Properties. *Adv. Mater.* **2015,** *27* (1), 73-78.

62. Greene, A. F.; Danielson, M. K.; Delawder, A. O.; Liles, K. P.; Li, X.; Natraj, A.; Wellen, A.; Barnes, J. C., Redox-responsive artificial molecular muscles: Reversible radical-based self-assembly for actuating hydrogels. *Chem. Mater.* **2017,** *29* (21), 9498-9508.

63. Murase, Y.; Takeshima, R.; Yoshida, R., Self-Driven Gel Conveyer: Effect of Interactions Between Loaded Cargo and Self-Oscillating Gel Surface. *Macromol. Biosci.* **2011,** *11* (12), 1713-1721.

64. Nakahata, M.; Takashima, Y.; Hashidzume, A.; Harada, A., Redox-generated mechanical motion of a supramolecular polymeric actuator based on host–guest interactions. *Angew. Chem. Int. Ed.* **2013,** *52* (22), 5731-5735.

65. Wang, B.; Tahara, H.; Sagara, T., Driving Quick and Large Amplitude Contraction of Viologen-Incorporated Poly-l-Lysine-Based Hydrogel by Reduction. *ACS Appl. Mater. Interfaces* **2018,** *10* (42), 36415-36424.

66. Liu, X.; Zhao, L.; Liu, F.; Astruc, D.; Gu, H., Supramolecular redox-responsive ferrocene hydrogels and microgels. *Coord. Chem. Rev.* **2020,** *419*, 213406.

67. Aramoto, H.; Osaki, M.; Konishi, S.; Ueda, C.; Kobayashi, Y.; Takashima, Y.; Harada, A.; Yamaguchi, H., Redox-responsive supramolecular polymeric networks having double-threaded inclusion complexes. *Chem. Sci.* **2020,** *11* (17), 4322-4331.

68. Xue, B.; Qin, M.; Wang, T.; Wu, J.; Luo, D.; Jiang, Q.; Li, Y.; Cao, Y.; Wang, W., Electrically controllable actuators based on supramolecular peptide hydrogels. *Adv. Funct. Mater.* **2016,** *26* (48), 9053-9062.

69. Yoshida, R.; Ueki, T., Evolution of self-oscillating polymer gels as autonomous polymer systems. *NPG Asia Materials* **2014,** *6* (6), e107-e107.

70. Murase, Y.; Maeda, S.; Hashimoto, S.; Yoshida, R., Design of a mass transport surface utilizing peristaltic motion of a self-oscillating gel. *Langmuir* **2009,** *25* (1), 483-489.

71. Tabata, O.; Kojima, H.; Kasatani, T.; Isono, Y.; Yoshida, R. In *Chemo-mechanical actuator using self-oscillating gel for artificial cilia*, The Sixteenth Annual International Conference on Micro Electro Mechanical Systems, 2003. MEMS-03 Kyoto. IEEE, IEEE: 2003; pp 12-15.

72. Maeda, S.; Hara, Y.; Sakai, T.; Yoshida, R.; Hashimoto, S., Self-walking gel. *Adv. Mater.* **2007,** *19* (21), 3480-3484.

73. Li, Z.; Davidson-Rozenfeld, G.; Vázquez-González, M.; Fadeev, M.; Zhang, J.; Tian, H.; Willner, I., Multi-triggered supramolecular DNA/bipyridinium dithienylethene hydrogels driven by light, redox, and chemical stimuli for shape-memory and self-healing applications. *J. Am. Chem. Soc.* **2018,** *140* (50), 17691-17701.

74. Culver, H. R.; Clegg, J. R.; Peppas, N. A., Analyte-Responsive Hydrogels: Intelligent Materials for Biosensing and Drug Delivery. *Acc. Chem. Res.* **2017,** *50* (2), 170-178.

75. Li, F.; Lyu, D.; Liu, S.; Guo, W., DNA Hydrogels and Microgels for Biosensing and Biomedical Applications. *Adv. Mater.* **2020,** *32* (3), 1806538.

76. Sim, H. J.; Jang, Y.; Kim, H.; Choi, J. G.; Park, J. W.; Lee, D. Y.; Kim, S. J., Self-Helical Fiber for Glucose-Responsive Artificial Muscle. *ACS Appl. Mater. Interfaces* **2020,** *12* (18), 20228-20233.

77. Tong, R.; Yu, H.; Wang, L., Glucose- Responsive Actuators Based on Bigel Strip from Host-Guest Assembly Between a β-Cyclodextrin-Based Host Gel and a Ferrocene-Based Guest Gel. *ChemistrySelect* **2020,** *5* (28), 8858-8863.

78. Zhao, J.; Liu, P.; Liu, Y., Adjustable Tribological Behavior of Glucose-Sensitive Hydrogels. *Langmuir* **2018,** *34* (25), 7479-7487.

79. Lee, J.; Ko, S.; Kwon, C. H.; Lima, M. D.; Baughman, R. H.; Kim, S. J., Carbon nanotube yarn-based glucose sensing artificial muscle. *Small* **2016,** *12* (15), 2085-2091.

80. McDonald, T. O.; Qu, H.; Saunders, B. R.; Ulijn, R. V., Branched peptide actuators for enzyme responsive hydrogel particles. *Soft Matter* **2009,** *5* (8), 1728-1734.

81. Hu, J.; Zhang, G.; Liu, S., Enzyme-responsive polymeric assemblies, nanoparticles and hydrogels. *Chem. Soc. Rev.* **2012,** *41* (18), 5933-5949.

82. Athas, J. C.; Nguyen, C. P.; Zarket, B. C.; Gargava, A.; Nie, Z.; Raghavan, S. R., Enzyme-Triggered Folding of Hydrogels: Toward a Mimic of the Venus Flytrap. *ACS Appl. Mater. Interfaces* **2016,** *8* (29), 19066-19074.

83. Cangialosi, A.; Yoon, C.; Liu, J.; Huang, Q.; Guo, J.; Nguyen, T. D.; Gracias, D. H.; Schulman, R., DNA sequence–directed shape change of photopatterned hydrogels via high-degree swelling. *Science* **2017,** *357* (6356), 1126-1130.

84. Fern, J.; Schulman, R., Modular DNA strand-displacement controllers for directing material expansion. *Nat. Commun.* **2018,** *9* (1), 1-8.

85. Zhang, J.-T.; Cai, Z.; Kwak, D. H.; Liu, X.; Asher, S. A., Two-Dimensional Photonic Crystal Sensors for Visual Detection of Lectin Concanavalin A. *Anal. Chem.* **2014,** *86* (18), 9036-9041.

86. Chen, C.; Dong, Z.-Q.; Shen, J.-H.; Chen, H.-W.; Zhu, Y.-H.; Zhu, Z.-G., 2D Photonic Crystal Hydrogel Sensor for Tear Glucose Monitoring. *ACS Omega* **2018,** *3* (3), 3211-3217.

87. Tang, W.; Chen, C., Hydrogel-Based Colloidal Photonic Crystal Devices for Glucose Sensing. *Polymers* **2020,** *12* (3), 625.

88. Lv, C.; Sun, X.-C.; Xia, H.; Yu, Y.-H.; Wang, G.; Cao, X.-W.; Li, S.-X.; Wang, Y.-S.; Chen, Q.-D.; Yu, Y.-D., Humidity-responsive actuation of programmable hydrogel microstructures based on 3D printing. *Sensors and Actuators B: Chemical* **2018,** *259*, 736-744.

89. Shin, B.; Ha, J.; Lee, M.; Park, K.; Park, G. H.; Choi, T. H.; Cho, K.-J.; Kim, H.-Y., Hygrobot: A self-locomotive ratcheted actuator powered by environmental humidity. *Science Robotics* **2018,** *3* (14).

90. Sun, X.-C.; Xia, H.; Xu, X.-L.; Lv, C.; Zhao, Y., Ingenious humidity-powered micro-worm with asymmetric biped from single hydrogel. *Sensors and Actuators B: Chemical* **2020**, 128620.

91. Yin, Q.; Tu, S.; Chen, M.; Wu, L., Bio-inspired Design of Reinforced Gradient Hydrogels with Rapid Water-Triggered Shape Memory Performance. *ACS Applied Polymer Materials* **2020**.

92. Chang, Q.; Darabi, M. A.; Liu, Y.; He, Y.; Zhong, W.; Mequanin, K.; Li, B.; Lu, F.; Xing, M. M., Hydrogels from natural egg white with extraordinary stretchability, direct-writing 3D printability and self-healing for fabrication of electronic sensors and actuators. *Journal of Materials Chemistry A* **2019,** *7* (42), 24626-24640.

93. Chen, X.; Goodnight, D.; Gao, Z.; Cavusoglu, A. H.; Sabharwal, N.; DeLay, M.; Driks, A.; Sahin, O., Scaling up nanoscale water-driven energy conversion into evaporation-driven engines and generators. *Nat. Commun.* **2015,** *6* (1), 7346.

94. Wang, Y.; Huang, W.; Wang, Y.; Mu, X.; Ling, S.; Yu, H.; Chen, W.; Guo, C.; Watson, M. C.; Yu, Y., Stimuli-responsive composite biopolymer actuators with selective spatial deformation behavior. *Proceedings of the National Academy of Sciences* **2020**.

95. Shang, J.; Theato, P., Smart composite hydrogel with pH-, ionic strength-and temperature-induced actuation. *Soft Matter* **2018,** *14* (41), 8401-8407.

96. Shi, W.; Huang, J.; Fang, R.; Liu, M., Imparting Functionality to the Hydrogel by Magnetic-Field-Induced Nano-assembly and Macro-response. *ACS Appl. Mater. Interfaces* **2020,** *12* (5), 5177-5194.

97. Han, I. K.; Chung, T.; Han, J.; Kim, Y. S., Nanocomposite hydrogel actuators hybridized with various dimensional nanomaterials for stimuli responsiveness enhancement. *Nano Convergence* **2019,** *6* (1), 18.

98. Haider, H.; Yang, C. H.; Zheng, W. J.; Yang, J. H.; Wang, M. X.; Yang, S.; Zrínyi, M.; Osada, Y.; Suo, Z.; Zhang, Q.; Zhou, J.; Chen, Y. M., Exceptionally tough and notch-insensitive magnetic hydrogels. *Soft Matter* **2015,** *11* (42), 8253-8261.

99. Caykara, T.; Yörük, D.; Demirci, S., Preparation and characterization of poly (N-tert-butylacrylamide-co-acrylamide) ferrogel. *J. Appl. Polym. Sci.* **2009,** *112* (2), 800-804.

100. Manjua, A. C.; Alves, V. D.; Crespo, J. o. G.; Portugal, C. A., Magnetic responsive PVA hydrogels for remote modulation of protein sorption. *ACS Appl. Mater. Interfaces* **2019,** *11* (23), 21239-21249.

101. Zhou, Y.; Sharma, N.; Deshmukh, P.; Lakhman, R. K.; Jain, M.; Kasi, R. M., Hierarchically structured free-standing hydrogels with liquid crystalline domains and magnetic nanoparticles as dual physical cross-linkers. *J. Am. Chem. Soc.* **2012,** *134* (3), 1630-1641.

102. Fuhrer, R.; Athanassiou, E. K.; Luechinger, N. A.; Stark, W. J., Crosslinking metal nanoparticles into the polymer backbone of hydrogels enables preparation of soft, magnetic field-driven actuators with muscle-like flexibility. *Small* **2009,** *5* (3), 383-388.

103. Xiong, Z.; Zheng, C.; Jin, F.; Wei, R.; Zhao, Y.; Gao, X.; Xia, Y.; Dong, X.; Zheng, M.; Duan, X., Magnetic-field-driven ultra-small 3D hydrogel microstructures: preparation of gel photoresist and two-photon polymerization microfabrication. *Sensors and Actuators B: Chemical* **2018,** *274*, 541-550.
104. Liu, Y.; Xu, K.; Chang, Q.; Darabi, M. A.; Lin, B.; Zhong, W.; Xing, M., Highly flexible and resilient elastin hybrid cryogels with shape memory, injectability, conductivity, and magnetic responsive properties. *Adv. Mater.* **2016,** *28* (35), 7758-7767.
105. Satarkar, N. S.; Zhang, W.; Eitel, R. E.; Hilt, J. Z., Magnetic hydrogel nanocomposites as remote controlled microfluidic valves. *Lab Chip* **2009,** *9* (12), 1773-1779.
106. Shen, T.; Font, M. G.; Jung, S.; Gabriel, M. L.; Stoykovich, M. P.; Vernerey, F. J., Remotely triggered locomotion of hydrogel mag-bots in confined spaces. *Scientific reports* **2017,** *7* (1), 1-10.
107. Huang, H.-W.; Sakar, M. S.; Petruska, A. J.; Pané, S.; Nelson, B. J., Soft micromachines with programmable motility and morphology. *Nat. Commun.* **2016,** *7* (1), 1-10.
108. Kim, S. J.; Kim, H. I.; Park, S. J.; Kim, I. Y.; Lee, S. H.; Lee, T. S.; Kim, S. I., Behavior in electric fields of smart hydrogels with potential application as bio-inspired actuators. *Smart materials and structures* **2005,** *14* (4), 511.
109. Li, Y.; Sun, Y.; Xiao, Y.; Gao, G.; Liu, S.; Zhang, J.; Fu, J., Electric field actuation of tough electroactive hydrogels cross-linked by functional triblock copolymer micelles. *ACS Appl. Mater. Interfaces* **2016,** *8* (39), 26326-26331.
110. Migliorini, L.; Santaniello, T.; Yan, Y.; Lenardi, C.; Milani, P., Low-voltage electrically driven homeostatic hydrogel-based actuators for underwater soft robotics. *Sensors and Actuators B: Chemical* **2016,** *228*, 758-766.
111. Takada, K.; Iida, T.; Kawanishi, Y.; Yasui, T.; Yuchi, A., An electrochemical actuator based on reversible changes in volume of poly (acrylic acid) gel induced by quinone redox. *Sensors and Actuators B: Chemical* **2011,** *160* (1), 1586-1592.
112. Morales, D.; Palleau, E.; Dickey, M. D.; Velev, O. D., Electro-actuated hydrogel walkers with dual responsive legs. *Soft Matter* **2014,** *10* (9), 1337-1348.
113. Jiang, H.; Fan, L.; Yan, S.; Li, F.; Li, H.; Tang, J., Tough and electro-responsive hydrogel actuators with bidirectional bending behavior. *Nanoscale* **2019,** *11* (5), 2231-2237.
114. Tungkavet, T.; Seetapan, N.; Pattavarakorn, D.; Sirivat, A., Graphene/gelatin hydrogel composites with high storage modulus sensitivity for using as electroactive actuator: Effects of surface area and electric field strength. *Polymer* **2015,** *70*, 242-251.
115. Yang, C.; Liu, Z.; Chen, C.; Shi, K.; Zhang, L.; Ju, X.-J.; Wang, W.; Xie, R.; Chu, L.-Y., Reduced Graphene Oxide-Containing Smart Hydrogels with Excellent Electro-Response and Mechanical Properties for Soft Actuators. *ACS Appl. Mater. Interfaces* **2017,** *9* (18), 15758-15767.
116. Sun, Z.; Yang, L.; Zhao, J.; Song, W., Natural Cellulose-Full-Hydrogels Bioinspired Electroactive Artificial Muscles: Highly Conductive Ionic Transportation Channels and Ultrafast Electromechanical Response. *J. Electrochem. Soc.* **2020,** *167* (4), 047515.
117. Shi, J.; Guo, Z.-X.; Zhan, B.; Luo, H.; Li, Y.; Zhu, D., Actuator based on MWNT/PVA hydrogels. *The Journal of Physical Chemistry B* **2005,** *109* (31), 14789-14791.
118. Ying, Z.; Wang, Q.; Xie, J.; Li, B.; Lin, X.; Hui, S., Novel electrically-conductive electro-responsive hydrogels for smart actuators with a carbon-nanotube-enriched three-dimensional conductive network and a physical-phase-type three-dimensional interpenetrating network. *J. Mater. Chem. C* **2020,** *8* (12), 4192-4205.
119. Anand, S. V.; Yakut Ali, M.; Saif, M. T. A., Cell culture on microfabricated one-dimensional polymeric structures for bio-actuator and bio-bot applications. *Lab on a Chip* **2015,** *15* (8), 1879-1888.
120. Li, Z.; Seo, Y.; Aydin, O.; Elhebeary, M.; Kamm, R. D.; Kong, H.; Saif, M. T. A., Biohybrid valveless pump-bot powered by engineered skeletal muscle. *Proceedings of the National Academy of Sciences* **2019,** *116* (5), 1543-1548.
121. Feinberg, A. W.; Feigel, A.; Shevkoplyas, S. S.; Sheehy, S.; Whitesides, G. M.; Parker, K. K., Muscular thin films for building actuators and powering devices. *Science* **2007,** *317* (5843), 1366-1370.

122. Shang, Y.; Chen, Z.; Fu, F.; Sun, L.; Shao, C.; Jin, W.; Liu, H.; Zhao, Y., Cardiomyocyte-Driven Structural Color Actuation in Anisotropic Inverse Opals. *ACS Nano* **2019,** *13* (1), 796-802.

123. Li, L.; Chen, Z.; Shao, C.; Sun, L.; Sun, L.; Zhao, Y., Graphene Hybrid Anisotropic Structural Color Film for Cardiomyocytes' Monitoring. *Adv. Funct. Mater.* **2020,** *30* (3), 1906353.

124. Xu, B.; Han, X.; Hu, Y.; Luo, Y.; Chen, C. H.; Chen, Z.; Shi, P., A Remotely Controlled Transformable Soft Robot Based on Engineered Cardiac Tissue Construct. *Small* **2019,** *15* (18), 1900006.

125. Morimoto, Y.; Onoe, H.; Takeuchi, S., Biohybrid device with antagonistic skeletal muscle tissue for measurement of contractile force. *Advanced Robotics* **2019,** *33* (5), 208-218.

126. Nagamine, K.; Kawashima, T.; Sekine, S.; Ido, Y.; Kanzaki, M.; Nishizawa, M., Spatiotemporally controlled contraction of micropatterned skeletal muscle cells on a hydrogel sheet. *Lab on a Chip* **2011,** *11* (3), 513-517.

127. Wang, X. Q.; Wang, C. F.; Zhou, Z. F.; Chen, S., Robust Mechanochromic Elastic One-Dimensional Photonic Hydrogels for Touch Sensing and Flexible Displays. *Advanced Optical Materials* **2014,** *2* (7), 652-662.

128. Dong, Y.; Bazrafshan, A.; Pokutta, A.; Sulejmani, F.; Sun, W.; Combs, J. D.; Clarke, K. C.; Salaita, K., Chameleon-inspired strain-accommodating smart skin. *ACS nano* **2019,** *13* (9), 9918-9926.

129. Liu, T.; Liu, M.; Dou, S.; Sun, J.; Cong, Z.; Jiang, C.; Du, C.; Pu, X.; Hu, W.; Wang, Z. L., Triboelectric-nanogenerator-based soft energy-harvesting skin enabled by toughly bonded elastomer/hydrogel hybrids. *ACS Nano* **2018,** *12* (3), 2818-2826.

130. Wang, S.; Li, Q.; Wang, B.; Hou, Y.; Zhang, T., Recognition of Different Rough Surface Based Highly Sensitive Silver Nanowire-Graphene Flexible Hydrogel Skin. *Ind. Eng. Chem. Res.* **2019,** *58* (47), 21553-21561.

131. Merindol, R.; Delechiave, G.; Heinen, L.; Catalani, L. H.; Walther, A., Modular Design of Programmable Mechanofluorescent DNA Hydrogels. *Nat. Commun.* **2019,** *10* (1), 1-10.

132. Ringer, P.; Weißl, A.; Cost, A.-L.; Freikamp, A.; Sabass, B.; Mehlich, A.; Tramier, M.; Rief, M.; Grashoff, C., Multiplexing molecular tension sensors reveals piconewton force gradient across talin-1. *Nat. Meth.* **2017,** *14* (11), 1090.

133. Cost, A. L.; Khalaji, S.; Grashoff, C., Genetically Encoded FRET-Based Tension Sensors. *Current protocols in cell biology* **2019,** *83* (1), e85.

134. Stabley, D. R.; Jurchenko, C.; Marshall, S. S.; Salaita, K. S., Visualizing mechanical tension across membrane receptors with a fluorescent sensor. *Nat. Meth.* **2012,** *9* (1), 64-67.

135. Galior, K.; Liu, Y.; Yehl, K.; Vivek, S.; Salaita, K., Titin-based nanoparticle tension sensors map high-magnitude integrin forces within focal adhesions. *Nano Lett.* **2016,** *16* (1), 341-348.

136. Ma, V. P.-Y.; Liu, Y.; Blanchfield, L.; Su, H.; Evavold, B. D.; Salaita, K., Ratiometric tension probes for mapping receptor forces and clustering at intermembrane junctions. *Nano Lett.* **2016,** *16* (7), 4552-4559.

137. Kong, H. J.; Kim, C. J.; Huebsch, N.; Weitz, D.; Mooney, D. J., Noninvasive probing of the spatial organization of polymer chains in hydrogels using fluorescence resonance energy transfer (FRET). *J. Am. Chem. Soc.* **2007,** *129* (15), 4518-4519.

138. He, F.; You, X.; Gong, H.; Yang, Y.; Bai, T.; Wang, W.; Guo, W.; Liu, X.; Ye, M., Stretchable, Biocompatible, and Multifunctional Silk Fibroin-Based Hydrogels toward Wearable Strain/Pressure Sensors and Triboelectric Nanogenerators. *ACS Appl. Mater. Interfaces* **2020,** *12* (5), 6442-6450.

139. Sun, P.; Zhang, H.; Xu, D.; Wang, Z.; Wang, L.; Gao, G.; Hossain, G.; Wu, J.; Wang, R.; Fu, J., Super tough bilayer actuators based on multi-responsive hydrogels crosslinked by functional triblock copolymer micelle macro-crosslinkers. *Journal of Materials Chemistry B* **2019,** *7* (16), 2619-2625.

140. Ma, C.; Le, X.; Tang, X.; He, J.; Xiao, P.; Zheng, J.; Xiao, H.; Lu, W.; Zhang, J.; Huang, Y., A multiresponsive anisotropic hydrogel with macroscopic 3D complex deformations. *Adv. Funct. Mater.* **2016,** *26* (47), 8670-8676.

141. Cheng, Y.; Ren, K.; Yang, D.; Wei, J., Bilayer-type fluorescence hydrogels with intelligent response serve as temperature/pH driven soft actuators. *Sensors and Actuators B: Chemical* **2018,** *255*, 3117-3126.

142. Rivero, R. E.; Molina, M. A.; Rivarola, C. R.; Barbero, C. A., Pressure and microwave sensors/actuators based on smart hydrogel/conductive polymer nanocomposite. *Sensors and Actuators B: Chemical* **2014,** *190*, 270-278.

143. Chen, L.; Weng, M.; Zhou, P.; Zhang, L.; Huang, Z.; Zhang, W., Multi-responsive actuators based on a graphene oxide composite: intelligent robot and bioinspired applications. *Nanoscale* **2017,** *9* (28), 9825-9833.

144. Li, H.; Go, G.; Ko, S. Y.; Park, J.-O.; Park, S., Magnetic actuated pH-responsive hydrogel-based soft micro-robot for targeted drug delivery. *Smart Materials and Structures* **2016,** *25* (2), 027001.

145. Han, B.; Gao, Y.-Y.; Zhang, Y.-L.; Liu, Y.-Q.; Ma, Z.-C.; Guo, Q.; Zhu, L.; Chen, Q.-D.; Sun, H.-B., Multi-field-coupling energy conversion for flexible manipulation of graphene-based soft robots. *Nano Energy* **2020,** *71*, 104578.

146. Zhang, Y.-L.; Ma, J.-N.; Liu, S.; Han, D.-D.; Liu, Y.-Q.; Chen, Z.-D.; Mao, J.-W.; Sun, H.-B., A "Yin"-"Yang" complementarity strategy for design and fabrication of dual-responsive bimorph actuators. *Nano Energy* **2020,** *68*, 104302.

147. Wang, T.; Li, M.; Zhang, H.; Sun, Y.; Dong, B., A multi-responsive bidirectional bending actuator based on polypyrrole and agar nanocomposites. *J. Mater. Chem. C* **2018,** *6* (24), 6416-6422.

148. Li, J.; Mou, L.; Zhang, R.; Sun, J.; Wang, R.; An, B.; Chen, H.; Inoue, K.; Ovalle-Robles, R.; Liu, Z., Multi-responsive and multi-motion bimorph actuator based on super-aligned carbon nanotube sheets. *Carbon* **2019,** *148*, 487-495.

149. Qin, H.; Zhang, T.; Li, N.; Cong, H.-P.; Yu, S.-H., Anisotropic and self-healing hydrogels with multi-responsive actuating capability. *Nat. Commun.* **2019,** *10* (1), 1-11.

150. https://en.wikipedia.org/wiki/Robot. *https://en.wikipedia.org/wiki/Robot*.

151. Wang, H.; Shi, Q.; Nakajima, M.; Takeuchi, M.; Chen, T.; Di, P.; Huang, Q.; Fukuda, T., Rail-guided multi-robot system for 3D cellular hydrogel assembly with coordinated nanomanipulation. *International Journal of Advanced Robotic Systems* **2014,** *11* (8), 121.

152. Tang, J.; Yao, C.; Gu, Z.; Jung, S.; Luo, D.; Yang, D., Super-Soft and Super-Elastic DNA Robot with Magnetically Driven Navigational Locomotion for Cell Delivery in Confined Space. *Angew. Chem. Int. Ed.* **2020,** *59* (6), 2490-2495.

153. Du, X.; Cui, H.; Xu, T.; Huang, C.; Wang, Y.; Zhao, Q.; Xu, Y.; Wu, X., Reconfiguration, Camouflage, and Color-Shifting for Bioinspired Adaptive Hydrogel-Based Millirobots. *Adv. Funct. Mater.* **2020,** *30* (10), 1909202.

154. Chen, Z.; Zhao, D.; Liu, B.; Nian, G.; Li, X.; Yin, J.; Qu, S.; Yang, W., 3D Printing of Multifunctional Hydrogels. *Adv. Funct. Mater.* **2019,** *29* (20), 1900971.

155. Higashi, K.; Miki, N., A self-swimming microbial robot using microfabricated nanofibrous hydrogel. *Sensors and Actuators B: Chemical* **2014,** *202*, 301-306.

156. Morimoto, Y.; Onoe, H.; Takeuchi, S., Biohybrid robot powered by an antagonistic pair of skeletal muscle tissues. *Science Robotics* **2018,** *3* (18).

157. Zhang, M.; Li, G.; Yang, X.; Xiao, Y.; Yang, T.; Wong, T.-W.; Li, T., Artificial muscle driven soft hydraulic robot: electromechanical actuation and simplified modeling. *Smart Materials and Structures* **2018,** *27* (9), 095016.

158. Liang, S.; Tu, Y.; Chen, Q.; Jia, W.; Wang, W.; Zhang, L., Microscopic hollow hydrogel springs, necklaces and ladders: a tubular robot as a potential vascular scavenger. *Materials Horizons* **2019,** *6* (10), 2135-2142.

159. Gerboni, G.; Diodato, A.; Ciuti, G.; Cianchetti, M.; Menciassi, A., Feedback control of soft robot actuators via commercial flex bend sensors. *IEEE/ASME Transactions on Mechatronics* **2017,** *22* (4), 1881-1888.

160. Bilodeau, R. A.; Kramer, R. K., Self-healing and damage resilience for soft robotics: a review. *Frontiers in Robotics and AI* **2017,** *4*, 48.

161. Wu, Y.; Yim, J. K.; Liang, J.; Shao, Z.; Qi, M.; Zhong, J.; Luo, Z.; Yan, X.; Zhang, M.; Wang, X., Insect-scale fast moving and ultrarobust soft robot. *Science Robotics* **2019,** *4* (32), eaax1594.

162. Galloway, K. C.; Becker, K. P.; Phillips, B.; Kirby, J.; Licht, S.; Tchernov, D.; Wood, R. J.; Gruber, D. F., Soft robotic grippers for biological sampling on deep reefs. *Soft robotics* **2016,** *3* (1), 23-33.

163. Qin, L.; Tang, Y.; Gupta, U.; Zhu, J., A soft robot capable of 2D mobility and self-sensing for obstacle detection and avoidance. *Smart Materials and Structures* **2018,** *27* (4), 045017.

164. Joyee, E. B.; Pan, Y., Multi-material additive manufacturing of functional soft robot. *Procedia Manufacturing* **2019,** *34*, 566-573.

165. Polygerinos, P.; Correll, N.; Morin, S. A.; Mosadegh, B.; Onal, C. D.; Petersen, K.; Cianchetti, M.; Tolley, M. T.; Shepherd, R. F., Soft robotics: Review of fluid-driven intrinsically soft devices; manufacturing, sensing, control, and applications in human-robot interaction. *Advanced Engineering Materials* **2017,** *19* (12), 1700016.

166. Lee, E. L.; Von Recum, H. A., Cell culture platform with mechanical conditioning and nondamaging cellular detachment. *J. Biomed. Mater. Res. Part A* **2010,** *93* (2), 411-418.

167. Koike, Y.; Yokoyama, Y.; Hayakawa, T., Light-Driven Hydrogel Microactuators for On-Chip Cell Manipulations. *Frontiers in Mechanical Engineering* **2020,** *6* (2).

168. Filippi, M.; Dasen, B.; Guerrero, J.; Garello, F.; Isu, G.; Born, G.; Ehrbar, M.; Martin, I.; Scherberich, A., Magnetic nanocomposite hydrogels and static magnetic field stimulate the osteoblastic and vasculogenic profile of adipose-derived cells. *Biomaterials* **2019,** *223*, 119468.

169. McKeon-Fischer, K.; Flagg, D.; Freeman, J., Coaxial electrospun poly (ε-caprolactone), multiwalled carbon nanotubes, and polyacrylic acid/polyvinyl alcohol scaffold for skeletal muscle tissue engineering. *Journal of biomedical materials research Part A* **2011,** *99* (3), 493-499.

170. Lim, J. W.; Kim, H.-j.; Kim, Y.; Shin, S. G.; Cho, S.; Jung, W. G.; Jeong, J. H., An Active and Soft Hydrogel Actuator to Stimulate Live Cell Clusters by Self-folding. *Polymers* **2020,** *12* (3), 583.

171. Cezar, C. A.; Roche, E. T.; Vandenburgh, H. H.; Duda, G. N.; Walsh, C. J.; Mooney, D. J., Biologic-free mechanically induced muscle regeneration. *Proceedings of the National Academy of Sciences* **2016,** *113* (6), 1534-1539.

172. Kirillova, A.; Maxson, R.; Stoychev, G.; Gomillion, C. T.; Ionov, L., 4D biofabrication using shape-morphing hydrogels. *Adv. Mater.* **2017,** *29* (46), 1703443.

173. van Rijt, S. H.; Bölükbas, D. A.; Argyo, C.; Datz, S.; Lindner, M.; Eickelberg, O.; Königshoff, M.; Bein, T.; Meiners, S., Protease-mediated release of chemotherapeutics from mesoporous silica nanoparticles to ex vivo human and mouse lung tumors. *ACS Nano* **2015,** *9* (3), 2377-2389.

174. Klumb, L. A.; Horbett, T. A., Design of insulin delivery devices based on glucose sensitive membranes. *J. Control. Release* **1992,** *18* (1), 59-80.

175. Cezar, C. A.; Kennedy, S. M.; Mehta, M.; Weaver, J. C.; Gu, L.; Vandenburgh, H.; Mooney, D. J., Biphasic ferrogels for triggered drug and cell delivery. *Adv Healthc Mater* **2014,** *3* (11), 1869-1876.

176. Lin, F.; Zheng, J.; Guo, W.; Zhu, Z.; Wang, Z.; Dong, B.; Lin, C.; Huang, B.; Lu, B., Smart cellulose-derived magnetic hydrogel with rapid swelling and deswelling properties for remotely controlled drug release. *Cellulose* **2019,** *26* (11), 6861-6877.

177. Kim, D.-i.; Lee, H.; Kwon, S.-h.; Choi, H.; Park, S., Magnetic nano-particles retrievable biodegradable hydrogel microrobot. *Sensors and Actuators B: Chemical* **2019,** *289*, 65-77.

178. Liang, Y.; Zhao, X.; Ma, P. X.; Guo, B.; Du, Y.; Han, X., pH-responsive injectable hydrogels with mucosal adhesiveness based on chitosan-grafted-dihydrocaffeic acid and oxidized pullulan for localized drug delivery. *Journal of Colloid and Interface Science* **2019,** *536*, 224-234.

179. Carrillo-Conde, B. R.; Brewer, E.; Lowman, A.; Peppas, N. A., Complexation Hydrogels as Oral Delivery Vehicles of Therapeutic Antibodies: An in Vitro and ex Vivo Evaluation of Antibody Stability and Bioactivity. *Industrial & Engineering Chemistry Research* **2015,** *54* (42), 10197-10205.

180. Sung, H.-W.; Sonaje, K.; Liao, Z.-X.; Hsu, L.-W.; Chuang, E.-Y., pH-Responsive Nanoparticles Shelled with Chitosan for Oral Delivery of Insulin: From Mechanism to Therapeutic Applications. *Accounts of Chemical Research* **2012,** *45* (4), 619-629.

181. Li, X.; Fu, M.; Wu, J.; Zhang, C.; Deng, X.; Dhinakar, A.; Huang, W.; Qian, H.; Ge, L., pH-sensitive peptide hydrogel for glucose-responsive insulin delivery. *Acta biomaterialia* **2017,** *51*, 294-303.

182. Teyssier, J.; Saenko, S. V.; Van Der Marel, D.; Milinkovitch, M. C., Photonic crystals cause active colour change in chameleons. *Nature communications* **2015,** *6* (1), 1-7.
183. Gur, D.; Palmer, B. A.; Leshem, B.; Oron, D.; Fratzl, P.; Weiner, S.; Addadi, L., The mechanism of color change in the neon tetra fish: a light-induced tunable photonic crystal array. *Angewandte Chemie International Edition* **2015,** *54* (42), 12426-12430.
184. Yoshioka, S.; Matsuhana, B.; Tanaka, S.; Inouye, Y.; Oshima, N.; Kinoshita, S., Mechanism of variable structural colour in the neon tetra: quantitative evaluation of the Venetian blind model. *Journal of the Royal Society Interface* **2011,** *8* (54), 56-66.
185. Niu, S.; Li, B.; Mu, Z.; Yang, M.; Zhang, J.; Han, Z.; Ren, L., Excellent structure-based multifunction of morpho butterfly wings: A review. *Journal of Bionic Engineering* **2015,** *12* (2), 170-189.
186. Lu, T.; Peng, W.; Zhu, S.; Zhang, D., Bio-inspired fabrication of stimuli-responsive photonic crystals with hierarchical structures and their applications. *Nanotechnology* **2016,** *27* (12), 122001.
187. Aguirre, C. I.; Reguera, E.; Stein, A., Tunable colors in opals and inverse opal photonic crystals. *Advanced Functional Materials* **2010,** *20* (16), 2565-2578.
188. Wu, S.; Xia, H.; Xu, J.; Sun, X.; Liu, X., Manipulating luminescence of light emitters by photonic crystals. *Advanced Materials* **2018,** *30* (47), 1803362.
189. Ge, D.; Lee, E.; Yang, L.; Cho, Y.; Li, M.; Gianola, D. S.; Yang, S., A robust smart window: reversibly switching from high transparency to angle-independent structural color display. *Advanced Materials* **2015,** *27* (15), 2489-2495.
190. Inan, H.; Poyraz, M.; Inci, F.; Lifson, M. A.; Baday, M.; Cunningham, B. T.; Demirci, U., Photonic crystals: emerging biosensors and their promise for point-of-care applications. *Chemical society reviews* **2017,** *46* (2), 366-388.
191. Lee, G. H.; Choi, T. M.; Kim, B.; Han, S. H.; Lee, J. M.; Kim, S.-H., Chameleon-inspired mechanochromic photonic films composed of non-close-packed colloidal arrays. *ACS nano* **2017,** *11* (11), 11350-11357.
192. Zhang, R.; Wang, Q.; Zheng, X., Flexible mechanochromic photonic crystals: routes to visual sensors and their mechanical properties. *Journal of Materials Chemistry C* **2018,** *6* (13), 3182-3199.
193. Cai, Z.; Kwak, D. H.; Punihaole, D.; Hong, Z.; Velankar, S. S.; Liu, X.; Asher, S. A., A photonic crystal protein hydrogel sensor for Candida albicans. *Angewandte Chemie* **2015,** *127* (44), 13228-13232.
194. Cai, Z.; Zhang, J.-T.; Xue, F.; Hong, Z.; Punihaole, D.; Asher, S. A., 2D photonic crystal protein hydrogel coulometer for sensing serum albumin ligand binding. *Analytical chemistry* **2014,** *86* (10), 4840-4847.
195. Gur, D.; Leshem, B.; Farstey, V.; Oron, D.; Addadi, L.; Weiner, S., Light-Induced Color Change in the Sapphirinid Copepods: Tunable Photonic Crystals. *Advanced Functional Materials* **2016,** *26* (9), 1393-1399.
196. Cai, Z.; Luck, L. A.; Punihaole, D.; Madura, J. D.; Asher, S. A., Photonic crystal protein hydrogel sensor materials enabled by conformationally induced volume phase transition. *Chemical science* **2016,** *7* (7), 4557-4562.
197. Luo, Z.; Evans, B. A.; Chang, C.-H., Magnetically actuated dynamic iridescence inspired by the neon tetra. *ACS nano* **2019,** *13* (4), 4657-4666.
198. Isapour, G.; Lattuada, M., Bioinspired stimuli-responsive color-changing systems. *Advanced Materials* **2018,** *30* (19), 1707069.
199. Couturier, J. P.; Sütterlin, M.; Laschewsky, A.; Hettrich, C.; Wischerhoff, E., Responsive inverse opal hydrogels for the sensing of macromolecules. *Angewandte Chemie International Edition* **2015,** *54* (22), 6641-6644.
200. Luo, W.; Cui, Q.; Fang, K.; Chen, K.; Ma, H.; Guan, J., Responsive hydrogel-based photonic nanochains for microenvironment sensing and imaging in real time and high resolution. *Nano Letters* **2018,** *20* (2), 803-811.
201. Ma, H.; Zhu, M.; Luo, W.; Li, W.; Fang, K.; Mou, F.; Guan, J., Free-standing, flexible thermochromic films based on one-dimensional magnetic photonic crystals. *Journal of Materials Chemistry C* **2015,** *3* (12), 2848-2855.

202. Zhang, J.-T.; Smith, N.; Asher, S. A., Two-dimensional photonic crystal surfactant detection. *Analytical chemistry* **2012,** *84* (15), 6416-6420.

203. Schauer, S.; Baumberg, J. J.; Hölscher, H.; Smoukov, S. K., Tuning of Structural Colors Like a Chameleon Enabled by Shape-Memory Polymers. *Macromolecular Rapid Communications* **2018,** *39* (21), 1800518.

204. Vatankhah-Varnosfaderani, M.; Keith, A. N.; Cong, Y.; Liang, H.; Rosenthal, M.; Sztucki, M.; Clair, C.; Magonov, S.; Ivanov, D. A.; Dobrynin, A. V., Chameleon-like elastomers with molecularly encoded strain-adaptive stiffening and coloration. *Science* **2018,** *359* (6383), 1509-1513.

205. Ye, B.-F.; Zhao, Y.-J.; Cheng, Y.; Li, T.-T.; Xie, Z.-Y.; Zhao, X.-W.; Gu, Z.-Z., Colorimetric photonic hydrogel aptasensor for the screening of heavy metal ions. *Nanoscale* **2012,** *4* (19), 5998-6003.

206. Park, J.-G.; Rogers, W. B.; Magkiriadou, S.; Kodger, T.; Kim, S.-H.; Kim, Y.-S.; Manoharan, V. N., Photonic-crystal hydrogels with a rapidly tunable stop band and high reflectivity across the visible. *Optical Materials Express* **2017,** *7* (1), 253-263.

207. Dong, Y.; Wen, B.; Chen, Y.; Cao, P.; Zhang, C., Autoclave-free facile approach to the synthesis of highly tunable nanocrystal clusters for magnetic responsive photonic crystals. *RSC advances* **2016,** *6* (69), 64434-64440.

208. Fukasawa, M.; Sakai, T.; Chung, U.-i.; Haraguchi, K., Synthesis and mechanical properties of a nanocomposite gel consisting of a tetra-PEG/clay network. *Macromolecules* **2010,** *43* (9), 4370-4378.

209. Kang, Y.; Walish, J. J.; Gorishnyy, T.; Thomas, E. L., Broad-wavelength-range chemically tunable block-copolymer photonic gels. *Nature materials* **2007,** *6* (12), 957-960.

210. Matsubara, K.; Watanabe, M.; Takeoka, Y., A thermally adjustable multicolor photochromic hydrogel. *Angewandte Chemie* **2007,** *119* (10), 1718-1722.

211. Haq, M. A.; Su, Y.; Wang, D., Mechanical properties of PNIPAM based hydrogels: A review. *Materials Science and Engineering: C* **2017,** *70,* 842-855.

212. Chen, R.; Zhu, K.; Gan, Q.; Yu, Y.; Zhang, T.; Liu, X.; Ye, M.; Yin, Y., Interfacial solar heating by self-assembled Fe 3 O 4@ C film for steam generation. *Materials Chemistry Frontiers* **2017,** *1* (12), 2620-2626.

213. Stöber, W.; Fink, A.; Bohn, E., Controlled growth of monodisperse silica spheres in the micron size range. *Journal of colloid and interface science* **1968,** *26* (1), 62-69.

214. Yang, Y.; Chen, Y.; Hou, Z.; Li, F.; Xu, M.; Liu, Y.; Tian, D.; Zhang, L.; Xu, J.; Zhu, J., Responsive photonic crystal microcapsules of block copolymers with enhanced monochromaticity. *ACS nano* **2020,** *14* (11), 16057-16064.

215. Chen, Q.; Wang, C.; Wang, S.; Zhou, J.; Wu, Z., A responsive photonic crystal film sensor for the ultrasensitive detection of uranyl ions. *Analyst* **2020,** *145* (16), 5624-5630.

216. Ge, J.; Yin, Y., Responsive photonic crystals. *Angewandte Chemie International Edition* **2011,** *50* (7), 1492-1522.

217. Yue, Y.; Kurokawa, T., Designing responsive photonic crystal patterns by using laser engraving. *ACS applied materials & interfaces* **2019,** *11* (11), 10841-10847.

218. Cai, Z.; Sasmal, A.; Liu, X.; Asher, S. A., Responsive photonic crystal carbohydrate hydrogel sensor materials for selective and sensitive lectin protein detection. *ACS sensors* **2017,** *2* (10), 1474-1481.

219. Chen, H.; Hou, A.; Zheng, C.; Tang, J.; Xie, K.; Gao, A., Light-and humidity-responsive chiral nematic photonic crystal films based on cellulose nanocrystals. *ACS Applied Materials & Interfaces* **2020,** *12* (21), 24505-24511.

220. Zhang, J.-T.; Wang, L.; Luo, J.; Tikhonov, A.; Kornienko, N.; Asher, S. A., 2-D array photonic crystal sensing motif. *Journal of the American Chemical Society* **2011,** *133* (24), 9152-9155.

221. Moirangthem, M.; Schenning, A. P., Full color camouflage in a printable photonic blue-colored polymer. *ACS applied materials & interfaces* **2018,** *10* (4), 4168-4172.

222. Hu, H.; Chen, Q.-W.; Tang, J.; Hu, X.-Y.; Zhou, X.-H., Photonic anti-counterfeiting using structural colors derived from magnetic-responsive photonic crystals with double photonic bandgap heterostructures. *Journal of Materials Chemistry* **2012,** *22* (22), 11048-11053.

223. Chen, K.; Zhang, Y.; Ge, J., Highly invisible photonic crystal patterns encrypted in an inverse opaline macroporous polyurethane film for anti-counterfeiting applications. *ACS Applied Materials & Interfaces* **2019,** *11* (48), 45256-45264.
224. Goodling, A. E.; Nagelberg, S.; Kolle, M.; Zarzar, L. D., Tunable and responsive structural color from polymeric microstructured surfaces enabled by interference of totally internally reflected light. *ACS Materials Letters* **2020,** *2* (7), 754-763.
225. Jia, X.; Xiao, T.; Hou, Z.; Xiao, L.; Qi, Y.; Hou, Z.; Zhu, J., Chemically Responsive Photonic Crystal Hydrogels for Selective and Visual Sensing of Thiol-Containing Biomolecules. *ACS omega* **2019,** *4* (7), 12043-12048.
226. Dong, Y.; Ramey-Ward, A. N.; Salaita, K., Programmable Mechanically Active Hydrogel-Based Materials. *Advanced Materials* **2021,** *33* (46), 2006600.
227. Liu, F.; Zhang, S.; Jin, X.; Wang, W.; Tang, B., Thermal-responsive photonic crystal with function of color switch based on thermochromic system. *ACS applied materials & interfaces* **2019,** *11* (42), 39125-39131.
228. Jiang, H.; Pan, V.; Vivek, S.; Weeks, E. R.; Ke, Y., Programmable DNA hydrogels assembled from multidomain DNA strands. *ChemBioChem* **2016,** *17* (12), 1156-1162.
229. Topuz, F.; Okay, O., Rheological behavior of responsive DNA hydrogels. *Macromolecules* **2008,** *41* (22), 8847-8854.
230. Steger, C., An unbiased detector of curvilinear structures. *IEEE Transactions on pattern analysis and machine intelligence* **1998,** *20* (2), 113-125.
231. Chen, C.; Zhao, X.; Chen, Y.; Wang, X.; Chen, Z.; Li, H.; Wang, K.; Zheng, X.; Liu, H., Reversible Writing/Re-Writing Polymeric Paper in Multiple Environments. *Advanced Functional Materials* **2021,** *31* (37), 2104784.
232. Chen, L.; Weng, M.; Huang, F.; Zhang, W., Long-Lasting and Easy-to-Use Rewritable Paper Fabricated by Printing Technology. *ACS Applied Materials & Interfaces* **2018,** *10* (46), 40149-40155.
233. Müller, V.; Hungerland, T.; Baljozovic, M.; Jung, T.; Spencer, N. D.; Eghlidi, H.; Payamyar, P.; Schlüter, A. D., Ink-Free Reversible Optical Writing in Monolayers by Polymerization of a Trifunctional Monomer: Toward Rewritable "Molecular Paper". *Advanced Materials* **2017,** *29* (27), 1701220.
234. Khazi, M. I.; Jeong, W.; Kim, J.-M., Functional Materials and Systems for Rewritable Paper. *Advanced Materials* **2018,** *30* (15), 1705310.
235. Wei, J.; Jiao, X.; Wang, T.; Chen, D., Electrospun Photochromic Hybrid Membranes for Flexible Rewritable Media. *ACS Applied Materials & Interfaces* **2016,** *8* (43), 29713-29720.
236. Du, X.; Li, T.; Li, L.; Zhang, Z.; Wu, T., Water as a colorful ink: transparent, rewritable photonic coatings based on colloidal crystals embedded in chitosan hydrogel. *Journal of Materials Chemistry C* **2015,** *3* (15), 3542-3546.
237. Wang, M.; He, L.; Hu, Y.; Yin, Y., Magnetically rewritable photonic ink based on superparamagnetic nanochains. *Journal of Materials Chemistry C* **2013,** *1* (38), 6151-6156.
238. Zhang, Y.; Qiu, Y.; Blanchard, A. T.; Chang, Y.; Brockman, J. M.; Ma, V. P.-Y.; Lam, W. A.; Salaita, K., Platelet integrins exhibit anisotropic mechanosensing and harness piconewton forces to mediate platelet aggregation. *Proceedings of the National Academy of Sciences* **2018,** *115* (2), 325-330.
239. Rashid, S. A.; Blanchard, A. T.; Combs, J. D.; Fernandez, N.; Dong, Y.; Cho, H. C.; Salaita, K., DNA Tension Probes Show that Cardiomyocyte Maturation Is Sensitive to the Piconewton Traction Forces Transmitted by Integrins. *ACS Nano* **2022**.
240. Jin, W.; Tamzalit, F.; Chaudhuri, P. K.; Black, C. T.; Huse, M.; Kam, L. C., T cell activation and immune synapse organization respond to the microscale mechanics of structured surfaces. *Proceedings of the National Academy of Sciences* **2019,** *116* (40), 19835-19840.
241. Park, J. S.; Chu, J. S.; Tsou, A. D.; Diop, R.; Tang, Z.; Wang, A.; Li, S., The effect of matrix stiffness on the differentiation of mesenchymal stem cells in response to TGF-β. *Biomaterials* **2011,** *32* (16), 3921-3930.

242. Liu, Y.; Medda, R.; Liu, Z.; Galior, K.; Yehl, K.; Spatz, J. P.; Cavalcanti-Adam, E. A.; Salaita, K., Nanoparticle tension probes patterned at the nanoscale: impact of integrin clustering on force transmission. *Nano letters* **2014,** *14* (10), 5539-5546.

243. Zhang, Y.; Ge, C.; Zhu, C.; Salaita, K., DNA-based digital tension probes reveal integrin forces during early cell adhesion. *Nature Communications* **2014,** *5* (1), 5167.

244. Sarkar, R.; Rybenkov, V. V., A guide to magnetic tweezers and their applications. *Frontiers in Physics* **2016,** *4*, 48.

245. Jiang, Y.; Yuan, H.; Li, Z.-X.; Wang, Z.; Zhang, H.; Cao, Y.; Yan, P., Twisted magnon as a magnetic tweezer. *Physical Review Letters* **2020,** *124* (21), 217204.

246. Toyjanova, J.; Hannen, E.; Bar-Kochba, E.; Darling, E. M.; Henann, D. L.; Franck, C., 3D Viscoelastic traction force microscopy. *Soft matter* **2014,** *10* (40), 8095-8106.

247. Bjugstad, K.; Redmond Jr, D.; Lampe, K.; Kern, D.; Sladek Jr, J.; Mahoney, M., Biocompatibility of PEG-based hydrogels in primate brain. *Cell transplantation* **2008,** *17* (4), 409-415.

248. Caddeo, C.; Pucci, L.; Gabriele, M.; Carbone, C.; Fernàndez-Busquets, X.; Valenti, D.; Pons, R.; Vassallo, A.; Fadda, A. M.; Manconi, M., Stability, biocompatibility and antioxidant activity of PEG-modified liposomes containing resveratrol. *International Journal of Pharmaceutics* **2018,** *538* (1), 40-47.

249. Singh, G.; Chanda, A., Mechanical properties of whole-body soft human tissues: a review. *Biomedical Materials* **2021**.

250. Ye, K.; Wang, X.; Cao, L.; Li, S.; Li, Z.; Yu, L.; Ding, J., Matrix stiffness and nanoscale spatial organization of cell-adhesive ligands direct stem cell fate. *Nano letters* **2015,** *15* (7), 4720-4729.

251. Chaudhuri, O., Viscoelastic hydrogels for 3D cell culture. *Biomaterials science* **2017,** *5* (8), 1480-1490.

252. Chaudhuri, O.; Cooper-White, J.; Janmey, P. A.; Mooney, D. J.; Shenoy, V. B., Effects of extracellular matrix viscoelasticity on cellular behaviour. *Nature* **2020,** *584* (7822), 535-546.

253. Ravi, M.; Paramesh, V.; Kaviya, S.; Anuradha, E.; Solomon, F. P., 3D cell culture systems: advantages and applications. *Journal of cellular physiology* **2015,** *230* (1), 16-26.

254. Huh, D.; Hamilton, G. A.; Ingber, D. E., From 3D cell culture to organs-on-chips. *Trends in cell biology* **2011,** *21* (12), 745-754.

255. Park, C. C.; Zhang, H.; Pallavicini, M.; Gray, J. W.; Baehner, F.; Park, C. J.; Bissell, M. J., β1 integrin inhibitory antibody induces apoptosis of breast cancer cells, inhibits growth, and distinguishes malignant from normal phenotype in three dimensional cultures and in vivo. *Cancer research* **2006,** *66* (3), 1526-1535.

256. Lee, G. Y.; Kenny, P. A.; Lee, E. H.; Bissell, M. J., Three-dimensional culture models of normal and malignant breast epithelial cells. *Nature methods* **2007,** *4* (4), 359-365.

257. Weigelt, B.; Lo, A. T.; Park, C. C.; Gray, J. W.; Bissell, M. J., HER2 signaling pathway activation and response of breast cancer cells to HER2-targeting agents is dependent strongly on the 3D microenvironment. *Breast cancer research and treatment* **2010,** *122* (1), 35-43.